AD-A140 804    STUDIES OF HEAT TRANSFER IN COMPLEX INTERNAL FLOWS(U)    1/2
               MINNESOTA UNIV MINNEAPOLIS DEPT OF MECHANICAL
               ENGINEERING  E M SPARROW APR 84 N00014-79-C-0621
UNCLASSIFIED                                     F/G 13/1        NL

MICROCOPY RESOLUTION TEST CHART
NATIONAL BUREAU OF STANDARDS-1963-A

STUDIES OF HEAT TRANSFER IN COMPLEX INTERNAL FLOWS

E. M. Sparrow

April, 1984

Department of Mechanical Engineering
University of Minnesota
Minneapolis, Minnesota 55455

84 05 03 002

SECURITY CLASSIFICATION OF THIS PAGE (When Data Entered)

| REPORT DOCUMENTATION PAGE | | READ INSTRUCTIONS BEFORE COMPLETING FORM |
|---|---|---|
| 1. REPORT NUMBER<br>N00014-79-C-0621-1984A | 2. GOVT ACCESSION NO.<br>AD-A140 804 | 3. RECIPIENT'S CATALOG NUMBER |
| 4. TITLE (and Subtitle)<br>STUDIES OF HEAT TRANSFER IN COMPLEX INTERNAL FLOWS | | 5. TYPE OF REPORT & PERIOD COVERED<br>Final Report<br>9/15/79 to 3/31/84 |
| | | 6. PERFORMING ORG. REPORT NUMBER |
| 7. AUTHOR(s)<br>E. M. Sparrow | | 8. CONTRACT OR GRANT NUMBER(s)<br>N00014-79-C-0621 |
| 9. PERFORMING ORGANIZATION NAME AND ADDRESS<br>Department of Mechanical Engineering<br>University of Minnesota, Minneapolis, MN | | 10. PROGRAM ELEMENT, PROJECT, TASK AREA & WORK UNIT NUMBERS<br>Work Unit NR097-437 |
| 11. CONTROLLING OFFICE NAME AND ADDRESS<br>Office of Naval Research<br>800 North Quincy Street<br>Arlington, Virginia 22217 | | 12. REPORT DATE<br>April, 1984 |
| | | 13. NUMBER OF PAGES<br>110 |
| 14. MONITORING AGENCY NAME & ADDRESS(if different from Controlling Office) | | 15. SECURITY CLASS. (of this report)<br>Unclassified |
| | | 15a. DECLASSIFICATION/DOWNGRADING SCHEDULE |

16. DISTRIBUTION STATEMENT (of this Report)

Approved for public release; distribution unlimited

17. DISTRIBUTION STATEMENT (of the abstract entered in Block 20, if different from Report)

18. SUPPLEMENTARY NOTES

19. KEY WORDS (Continue on reverse side if necessary and identify by block number)

heat exchangers, flow maldistribution, heat transfer coefficient, pressure drop, tube bank, swirl

20. ABSTRACT (Continue on reverse side if necessary and identify by block number)

This is the final report of a research program whose objective was to determine the heat transfer and pressure drop characteristics of heat exchange devices subject to highly complex fluid flows. The report consists of two parts. The first part summarizes the results of research that has already been described in progress reports, while the second part conveys the results of investigations conducted and

DD FORM 1473 EDITION OF 1 NOV 68 IS OBSOLETE
1 JAN 73
S/N 0102-LF-014-6601

completed since the distribution of the last progress report.

The general theme which runs through the work is a search for the effects of flow maldistribution on heat transfer in various types of heat exchange devices. The maldistribution may be caused by the turning of the flow upstream of the inlet, abrupt changes of cross-sectional area, blockage, competition between parallel flow passages, misalignment of the inlet and outlet of plenum chambers, swirl, and the presence of enhancement devices. The investigated geometries included tube banks in crossflow, circuler tubes, and rectangular flow passages.

The research was experimental in nature. In each of the investigated problems, data were collected over a Reynolds number range appropriate to practice. In certain of the problems, the heat transfer results were obtained by means of thermal measurements. In other cases, mass transfer coefficients were measured via the naphthalene sublimation technique, and the mass transfer coefficients were converted to heat transfer coefficients by the well-established analogy between heat and mass transfer. The fluid flow measurements included the pressure drop and, in some cases, flow visualization.

DTIC
SELECTED
MAY 4 1984
B

| Accession For | |
|---|---|
| NTIS GRA&I | ✓ |
| DTIC TAB | ☐ |
| Unannounced | ☐ |
| Justification | |
| By | |
| Distribution/ | |
| Availability Codes | |
| Dist | Avail and/or Special |
| A-1 | |

# INTRODUCTION TO THE REPORT

The heat transfer devices that are employed in power producing systems are subject to highly complex fluid flows whose effect on performance is generally unknown. In this regard, information available in the literature is not readily applicable since, for the most part, it is based on studies of relatively simple flows and of elementary geometrical configurations. Even when more complex devices are studied, only overall data are collected, so that the causes of observed effects have not been identified.

As an example of the encountered flow complexities, attention may be called to the possible maldistribution of the flow delivered to the heat exchanger inlet, a case in point being Navy shipboard heat recovery which utilizes hot gases exhausted from gas turbines. The maldistribution may result from changes in cross section (e.g., sudden enlargement), partial blockages due to valves and other control devices, changes in direction due to bends and elbows, and branching and merging of flow passages. Frequently, more than one of these features occur in a single system. The maldistribution may be accompanied by flow separation, recirculation, and swirl.

Among the external manifestations of these flow processes are increased pressure losses and possible unsteadiness. Perhaps of even greater significance are the heat transfer ramifications. For example, the heat transfer coefficients in a region of flow separation may either be substantially lower or substantially higher than that for a uniform flow, depending on the Reynolds number. In general, large variations of the local heat transfer coefficient can be expected in complex flows, in contrast to the relatively uniform coefficients that are characteristic of conventional flows. These variations may give rise to local hot spots. In addition, it can be expected that on the average, the general level of the transfer coefficient will be higher in complex flows.

The foregoing discussion conveys the rationale for the research program that was initiated at the University of Minnesota in September, 1979. The program was concluded on March 31, 1984. The accomplishments of the program through December, 1982 are documented in three previously distributed progress reports. Three additional experimental investigations have been completed since that time.

This report is the final report of the research program. It consists of two parts. Part I conveys the highlights of the research that was reported in the three already distributed progress reports. The second part is an in-depth description of the research that was conducted and completed subsequent to the distribution of the last of the progress reports. The three problems investigated during that period are

1.  Heat Exchanger Situated Downstream of a Right-Angle Bend

2.  Swirl-Affected Turbulent Fluid Flow and Heat Transfer in a Circular Tube

3.  Symmetric Vs. Asymmetric Periodic Disturbances at the Walls of a Heated Flow Passage

Each of these research problems is described in a separate section which is a fully self-contained report in itself.

Part I

SUMMARIES OF PRIOR PROJECT REPORTS

1.  EFFECT OF BLOCKAGE-INDUCED FLOW MALDISTRIBUTION ON THE HEAT TRANSFER
    AND PRESSURE DROP IN A TUBE BANK

    Detailed experiments, encompassing per-tube heat transfer measurements and
row-by-row pressure measurements, were performed to investigate the response of
a tube bank to maldistribution of the flow at the inlet cross section.  The mal-
distribution was created by a partial blockage of the inlet section.  Baseline
experiments for uniformly distributed inlet flow were also carried out.  The
experiments spanned an order of magnitude range in the Reynolds number.  On the
whole, the inlet-section flow maldistribution tends to enhance the heat transfer
at a given Reynolds number.  Enhancements in the 30 - 40 percent range are en-
countered in the first several rows in the corridor downstream of the unblocked
portion of the inlet section.  Reductions (up to 50 percent) are confined to a
narrow alley behind the blockage.  Ten percent maldistribution-related effects
persist to the seventh row, while effects at the five percent level occur at least
as far downstream as the twelfth row.  With regard to pressure, there is an incre-
mental pressure drop of about $2\frac{1}{2}$ velocity heads due to the maldistribution.

2.  HEAT TRANSFER IN A TUBE BANK IN THE PRESENCE OF UPSTREAM CROSS-SECTIONAL
    ENLARGEMENT

    Per-tube heat transfer coefficients were determined in a tube bank in the
presence of an abrupt upstream enlargement of the flow cross section.  The enlarge-
ment occurred either at the inlet face of the tube bank or at the upstream end of
a duct which delivered the flow to the inlet.  Three different magnitudes of en-
largement were investigated along with three lengths of the delivery duct.  Axial
pressure distributions were measured both in the tube bank and in the delivery
duct, and flow visualization was performed to observe the fluid motions in the
tube bank.  It was found that the enlargement can give rise to appreciable

increases in the tube-bank heat transfer coefficients compared with those for the no-enlargement case. The enlargement also causes an additional pressure drop which depends on the magnitude of the enlargement and, to a lesser extent, on the distance between the enlargement and the tube bank.

3. MALDISTRIBUTED-INLET-FLOW EFFECTS ON TURBULENT HEAT TRANSFER AND PRESSURE DROP IN A FLAT RECTANGULAR DUCT

The effects of flow maldistribution caused by partial blockage of the inlet of a flat rectangular duct were studied experimentally. Local heat transfer coefficients were measured on the principal walls of the duct for two blockages and for Reynolds numbers spanning the range between 6000 and 30,000. Measurements were also made of the pressure distribution along the duct, and the flow pattern was visualized by the oil-lampblack technique. Large spanwise nonuniformities of the local heat transfer coefficient were induced by the maldistributed flow. These nonuniformities persisted to far downstream locations, especially in the presence of severe inlet-flow maldistributions. Spanwise-average heat transfer coefficients, evaluated from the local data, were found to be enhanced in the downstream portion of the duct due to the flow maldistribution. However, at more upstream locations, where the entering flow reattached to the duct wall following its separation at the sharp-edged inlet, the average coefficients were reduced by the presence of the maldistribution.

4. IN-TUBE HEAT TRANSFER FOR SKEWED INLET FLOW CAUSED BY COMPETITION AMONG TUBES FED BY THE SAME PLENUM

Measurements were made of the axial and circumferential distributions of the heat transfer coefficient in a tube in which the entering airflow is highly skewed. The skewness was caused by competition between the test section tube and a parallel tube which draws air from the same plenum chamber. For each of several fixed

Reynolds numbers in the test section tube, the flow imbalance between the compet-
ing tubes was varied parametrically (up to a factor of eighteen), as was the
center-to-center separation distance between the tubes (separation = 1.5, 3, and
4.5 times the tube diameter). Measurements were also made of the pressure drop,
and a visualization technique was employed to examine the pattern of fluid flow.
Practically significant effects of the flow imbalance on the axial distribution of
the heat transfer coefficient were encountered only at the smallest of the investi-
gated inter-tube spacings. Even for that case, the effects were moderate; for
example, the imbalance-related changes for an imbalance ratio of two did not ex-
ceed seven percent. The experiments involved naphthalene sublimation, and a new
technique was developed for coating the inside surface of a tube with naphthalene.

5.  HEAT TRANSFER AND FLUID FLOW EXPERIMENTS WITH A TUBE FED BY A PLENUM HAVING
    NONALIGNED INLET AND EXIT

   Local turbulent heat transfer coefficients for airflow were measured in a
tube situated downstream of a cylindrical plenum chamber in which the inflow was
radial and the outflow was axial. Pressure drop measurements and flow visualiza-
tion were performed to supplement the heat transfer experiments. The plenum length
and diameter were varied systematically during the experiments, and the Reynolds
number ranged from 10,000 to 60,000. Substantially higher Nusselt numbers in
the tube were encountered for the present nonaligned plenum inlet/exit configura-
tion than for a plenum with axially aligned inlet and exit or for an upstream
hydrodynamic development section. For a given Reynolds number, the Nusselt numbers
corresponding to the present plenum configuration were quite insensitive to the
investigated geometrical parameters. The thermal development length was found to
be substantially elongated due to swirl carried into the tube from the plenum;
the presence of the swirl was confirmed by flow visualization. The net pressure
loss due to the presence of the plenum was about 1.75 velocity heads and was quite

insensitive to the geometrical parameters and to the Reynolds number.

6. EFFECT OF PLENUM LENGTH AND DIAMETER ON TURBULENT HEAT TRANSFER IN A
   DOWNSTREAM TUBE AND ON PLENUM-RELATED PRESSURE LOSSES

A systematic experimental study was carried out to determine how the heat transfer characteristics of a turbulent tube flow are affected by the length and diameter of a cylindrical plenum chamber which delivers fluid to the tube. The net pressure loss due to the presence of the plenum was also measured. The experimental arrangement was such that the fluid experiences a consecutive expansion and contraction in the plenum before entering the electrically heated test section. Air was the working fluid, and the Reynolds number was varied over the range from 5,000 to 60,000. It was found that at axial stations in the upstream portion of the tube, there are substantially higher heat transfer coefficients in the presence of longer plenums. Thus, a longer plenum functions as an enhancement device. On the other hand, the plenum diameter appears to have only a minor influence in the range investigated (i.e., plenum diameters equal to three and six times the tube diameter). The fully developed Nusselt numbers are independent of the plenum length and diameter. With longer plenums in place, the thermal entrance length showed increased sensitivity to Reynolds number in the fully turbulent regime. The pressure loss coefficient, which compares the plenum-related pressure loss with the velocity head in the tube, increases more or less linearly with the plenum length. With regard to experimental technique, it was demonstrated that guard heating/cooling of the electrical bus adjacent to the tube inlet is necessary for accurate heat transfer results at low Reynolds numbers but, although desirable, is less necessary at higher Reynolds numbers.

7.  HEAT TRANSFER IN A TUBE DOWNSTREAM OF A TEE IN WHICH AIRSTREAMS OF
    DIFFERENT TEMPERATURES ARE MIXED

Heat transfer experiments were performed for the mixing of two pipe flows
of different temperatures to obtain the heat transfer coefficients for turbulent
flow in a tube situated downstream of a mixing tee.  In the experiments, pre-
heated air was delivered to the center port of the tee while unheated air was
delivered to one of the side ports.  The merged flow exited the tee from the other
side port and passed into the test section tube.  Measurements were made to de-
termine the circumferential average heat transfer coefficients and circumferential
variations of the local heat transfer coefficients of each axial station.

The imbalance in the entering bulk temperatures of the component flows served
as a parameter of the study.  It was made dimensionless relative to the fully de-
veloped wall-to-bulk temperature difference.  The range of this temperature
parameter extended from 0 to 3.  Reynolds numbers of 20000 and 30000 were used
during the experiments.  At each Reynolds number, variations were made in the
ratio of the flow supplied to the tee via the side port $\dot{m}_1$ to the exiting flow $\dot{m}$.

It was found that the influence of the initial bulk temperature imbalance on
the circumferential average heat transfer coefficient was largest at small $x/D$
and diminished as the fully developed regime was approached.  The effects were
greatest for the $\dot{m}_1/\dot{m} = 0.75$ and almost nonexistent in the case of $\dot{m}_1/\dot{m} = 0.25$.

In the presence of the bulk temperature imbalance, the largest heat transfer
coefficients occurred along the wall of the tube diametrically opposite the center
port, while those for the no-imbalance case occurred along the same side as the
center port.  The extent of the circumferential variations increased as the tem-
perature imbalance increased.  The circumferential variations diminished as the
downstream distance increased, but the shape of the angular distributions re-
versed in some cases.  Finally, the circumferential variations vanished at a suf-
ficient downstream distance.

8. PRESSURE DROP CHARACTERISTICS FOR A SHROUDED LONGITUDINAL-FIN ARRAY
   WITH TIP CLEARANCE

Experiments were performed to determine friction factors for flow in a duct in which internal longitudinal fins are affixed to one of the principal walls. The fins do not extend across the entire cross section of the duct, but there is a clearance gap between the fin tips and the adjacent wall. The clearance gap was varied parametrically throughout the study, as was the interfin spacing. These variations were accomplished by a duct design which enabled easy inter-changeability of interfin spacer bars and fin heights. The Reynolds number was also varied during the investigation.

Auxiliary experiments in which the duct was operated without fins yielded friction factors in good agreement with the literature. The friction factor data with the fins in place could be correlated so that the tip clearance gap was not an active parameter. On the other hand, there was a data spread due to the interfin spacing, the extent of which was, for the most part, about ten percent.

9. EFFECT OF A MISSING CYLINDER ON HEAT TRANSFER AND FLUID FLOW IN AN ARRAY
   OF CYLINDERS IN CROSSFLOW

Experiments encompassing both heat transfer measurements and flow visualization were performed for crossflow arrays of cylinders in which there is a missing cylinder. Both staggered and in-line arrays were investigated. The visualization work, carried out with the oil-lampblack technique, yielded highly revealing photographs of the patterns of fluid flow, both for fully populated arrays and for arrays which have a missing cylinder. With regard to heat transfer, it was found that a staggered array is more responsive to a missing cylinder than is an in-line array.

PART II

REPORT OF RESEARCH PERFORMED DURING

THE PERIOD DECEMBER 15, 1982 TO MARCH 31, 1984

# HEAT EXCHANGER SITUATED DOWNSTREAM OF A RIGHT-ANGLE BEND

## ABSTRACT

Heat transfer, pressure drop, and flow visualization experiments were per-
formed for a tube-bank-type crossflow heat exchanger situated downstream of a
right-angle bend. The heat exchanger was housed in a duct of square cross sec-
tion, and the L-shaped duct which delivered the airflow to the tube bank inlet
was of identical cross section. Two geometrical parameters were varied during
the course of the experiments: (1) the distance between the bend and the tube
bank inlet and (2) the orientation of the plane of the bend with respect to the
axes of the tubes in the bank (either parallel or perpendicular to the axes). The
Reynolds number was varied over nearly an order of magnitude. For each geometry
and Reynolds number, per-tube heat transfer coefficients were determined at each
relevant tube site in the array. It was found that the presence of the right-
angle bend did not have a major effect on the heat transfer characteristics of
the tube bank. Bend-related enhancements in the 10 - 15 percent range were en-
countered at individual tubes in the initial rows, but the row-average enhance-
ments were smaller. Inter-row nonuniformities occurred for the perpendicular
orientation but not for the parallel orientation. The system pressure drop (from
delivery duct inlet to tube bank exit) was even less sensitive to the geometrical
parameters than the per-tube heat transfer.

## NOMENCLATURE

$A_{min}$     minimum free flow area between tubes

$A_w$     surface area of a tube

D     tube diameter

$\mathcal{D}$     diffusion coefficient

$f_{fd}$     fully developed friction factor, $\Delta p_{row}/\tfrac{1}{2}\rho V^2$

K     per-tube mass transfer coefficient, equation (1)

L*     distance between bend and tube bank inlet

$\Delta M$     change in mass during data run

p     pressure

$P_{atm}$     ambient pressure

$\Delta p_{row}$     fully developed per-row pressure drop

$\Delta p_{tot}$     pressure drop for flow circuit

Re     Reynolds number, $(\dot{w}/A_{min})D/\mu$

Sc     Schmidt number, $\nu/\mathcal{D}$

Sh     per-tube Sherwood number, $KD/\mathcal{D}$

$Sh_{fd}$     fully developed per-tube Sherwood number

S     side of duct

$S_L$     longitudinal pitch

$S_T$     transverse pitch

V     velocity at minimum free flow area in bank

$\dot{w}$     mass flowrate

X     coordinate along duct centerline

Greek symbols

$\mu$     viscosity

$\nu$     kinematic viscosity

$\rho$     air density

$\rho_{nw}$      naphthalene vapor density at tube surface

$\rho_{nb}$      naphthalene vapor density in bulk flow

$\tau$      duration of data run

# INTRODUCTION

In heat exchanger installations, it is not uncommon that a right-angle bend is situated upstream of the inlet face of the exchanger. It is known that such a bend introduces nonuniformities in the velocity distribution, with the flow packing to the outside of the bend. In addition, the bend creates a secondary flow in the form of corkscrew-like vortices which are superposed on the mainflow. Thus, the presence of the bend causes the flow that is presented to the inlet of the heat exchanger to be both nonuniformly distributed and nonunidirectional. The extent to which these nonidealities exist at the exchanger inlet depends on the distance between the bend and the inlet.

The research reported here is concerned with a tube-bank-type crossflow heat exchanger to which the crossflow fluid is delivered via a right-angle bend. Two orientations of the bend with respect to the tube bank were investigated. In one, the plane formed by the L-shaped delivery duct which contains the bend was oriented perpendicular to the axes of the tubes in the bank. On the other hand, in the other orientation, the plane of the L-duct was parallel to the tube axes. These two orientations yield markedly different inlet-face flow patterns. In particular, the vortices spawned by the bend are oriented differently with respect to the tube axes, and the flow nonuniformity is differently distributed.

For each of the two orientations, the distance between the bend and the inlet was varied parametrically. Three distances were employed, so that a total of six different configurations were investigated. For each configuration, experiments were performed for two Reynolds numbers which spanned nearly an order of magnitude.

For each case (given orientation, bend-to-inlet distance, and Reynolds number), per-tube Nusselt numbers were determined for each tube of the bank. Axial pressure distributions were also measured for each case, and friction factors, based on the pressure drop per row, were deduced. In addition, a flow visualization

study, performed with the oil-lampblack technique, was undertaken with the aim of observing alterations in the fluid flow pattern in the heat exchanger due to the presence of the bend.

Despite the realization of the potential importance of inlet-section fluid flow maldistributions on heat exchanger performance [1], there appears to be very little relevant experimental work in the literature. As part of a long-range research program, of which the present paper describes the final phase, the authors have investigated maldistributions caused by partial cross-sectional blockages and abrupt enlargements [2, 3]. Computational models based on hypothesized (and unverified) distributions of the heat transfer coefficient have been proposed (e.g., [4 - 7]) to estimate the effects of flow maldistribution. These hypotheses include local application of heat transfer coefficients for nonmaldistributed flows and a power-law relation between the transfer coefficient and the mass velocity.

## THE EXPERIMENTS

It was highly advantageous to carry out the research by means of mass transfer experiments. The per-tube Sherwood numbers (dimensionless mass transfer coefficients) determined from such experiments can be converted to per-tube Nusselt numbers by employing the well-established analogy between heat and mass transfer. The mass transfer experiments were performed utilizing the naphthalene sublimation technique.

In the execution of the mass transfer experiments, an approach was adopted which is frequently used in experimental work on heat transfer in tube banks. In that approach, only one of the tubes in the bank is heated during a given data run, and the heated tube is positioned at different sites in the bank during different data runs. Similarly, in the present experiments, only one mass-transfer-active tube was employed in each data run. However, for each case (given orientation, bend-to-inlet distance, and Reynolds number), sufficient runs were

made to enable the active tube to be positioned at all relevant sites in the array.

Experimental apparatus. A schematic, pictorial view of the experimental apparatus is presented in Fig. 1. As seen there, an L-shaped duct (the delivery duct) conveys air drawn from the laboratory room to the test section, which houses a model of a tube-bundle-type crossflow heat exchanger. The delivery duct and the test section are both of square cross section with side S. After traversing the test section, the air passes through a redevelopment length (also of S x S cross section) and is then ducted to a flowmeter (calibrated rotameter), control valve, and blower. The blower was situated in a service corridor outside the laboratory. The compression-heated, naphthalene-laden discharge of the blower was vented outside the building. Operation of the apparatus in the suction mode assured that the air delivered to the test section was free of naphthalene vapor.

The portion of the L-shaped delivery duct situated upstream of the bend had a length equal to 6S (S = side of square cross section), and this length was fixed throughout the experiments. On the other hand, the length of the delivery duct downstream of the bend was one of the key parameters of the research. This length is designated as L* in Fig. 1. The L*/S values employed during the research were 0.8, 2.5, and 4.5, with 0.8 being the smallest value consistent with the flanges and screw fittings that were used to connect the delivery duct to the test section.

In the execution of the research, the experiments for the L*/S = 4.5 case (largest L*) were carried out first. When these experiments were concluded, a portion of the downstream end of the delivery duct was cut off, leaving L*/S = 2.5. Similarly, when the L*/S = 2.5 case was completed, the duct was further cut to yield the L*/S = 0.8 case.

As was noted earlier, two orientations of the bend with respect to the tube bank were investigated. These orientations are illustrated in Figs. 2 and 3. In Fig. 2, the plane of the L-shaped delivery duct is seen to be perpendicular to the axes of the tubes in the heat exchanger. This arrangement will hereafter be

termed the perpendicular orientation. Figure 3 shows the parallel orientation wherein the plane of the L is parallel to the axes of the tubes.

Figure 2 also serves to illustrate the layout of the array. The tubes are seen to be on equilateral-triangular centers ($S_L/S_T = \sqrt{3}/2$), with $S_T/D = 2$. There are six tubes in each row. In alternate rows, half tubes are positioned adjacent to the side walls in order to help approximate an array of infinite width. The experiments were performed with fifteen rows of tubes. Downstream of the fifteenth row, the S x S cross section continues for a distance of about 10S, at which point the transition from a square to a circular cross section occurs.

The heat exchanger tubes were modeled by solid cylinders fabricated from drill rod stock of diameter D. For those tubes which did not participate in the mass transfer process, the rod stock was used essentially as is, aside from cutting to the proper length ($= S$) and buffing of the surface. The mass-transfer-active tubes were also fabricated from the same rod stock. To accommodate a thin naphthalene coating, the rods were machined to a slightly reduced diameter. The naphthalene was applied by a two-step process which first involved dipping the rod into molten naphthalene and then machining the solidified coating so as to obtain a hydrodynamically smooth surface of diameter D. A freshly coated rod was employed for each data run. Further details of the coating procedure are given in [2].

The actual physical dimensions of the apparatus may be specified via the side length S and the tube diameter D, whose values were 7.62 cm (3 in.) and 0.635 cm (0.250 in.).

Experimental procedure. In the execution of a data run, the primary objective is to determine the change of mass of the coated tube which results from the sublimation of the naphthalene during the run. Correspondingly, the mass of the coated tube is measured immediately before it is subjected to the airflow and immediately after the period of exposure. To accomplish these measurements, it is essential that the coated tube is able to be withdrawn from or installed in the

test section with dispatch (i.e., in a few seconds). To this end, the upper wall of the test section was made removable and fitted with quick-acting clamps. The mass was measured by an ultra-precision electronic balance with a resolution of $10^{-5}$ g.

Each data run was preceded by a preparatory period during which the coated tube attained thermal equilibrium with the airflow. During this period, the tube was in place in the array but was covered with an impermeable Teflon jacket which suppressed mass transfer. The equilibration period was a prerequisite for the definition of the operating conditions of the experiment, especially since the vapor pressure of naphthalene (which drives the mass transfer) is sensitive to temperature.

Axial pressure distributions were measured in a set of experiments separate from the mass transfer experiments. The pressure tap locations are shown in Fig. 1. The pressure signals were measured by a Baratron pressure meter with a resolution of 0.001 Torr.

The flow visualization was performed using the oil-lampblack technique [8]. For this work, the floor of the test section was covered with white, self-adhering, plasticized contact paper in which holes were made to accommodate the lower ends of the tubes. Prior to the initiation of the airflow, the contact paper was brushed with a suitable mixture of lampblack powder and oil. When the airflow was activated and maintained, the mixture moved under the action of the fluid shear forces, yielding a pattern of lines which reflect the flow pattern adjacent to the floor of the test section.

## RESULTS AND DISCUSSION

Data reduction. The evaluation of the per-tube mass transfer coefficient K involves the following quantities: (1) the change of mass $\Delta M$ during the data run, (2) the duration $\tau$ of the run, (3) the surface area $A_w$ of the tube, (4) the naphthalene vapor density $\rho_{nw}$ at the tube surface, and (5) the naphthalene

vapor pressure $\rho_{nb}$ in the airflow (b$\sim$ bulk). With these,

$$K = (\Delta M/\tau A_w)/(\rho_{nw} - \rho_{nb}) \tag{1}$$

Among the foregoing, $\Delta M$, $\tau$, and $A_w$ were directly measured, $\rho_{nb} = 0$, and $\rho_{nw}$ was calculated from the vapor pressure--temperature equation for naphthalene [9] and the perfect gas law.

The per-tube Sherwood number may be defined as $Sh = KD/\mathcal{D}$, where $\mathcal{D}$ is the mass diffusion coefficient. By introducing the Schmidt number $Sc = \nu/\mathcal{D}$, the diffusion coefficient can be elminated, so that

$$Sh = (KD/\nu)Sc \tag{2}$$

The Schmidt number for naphthalene diffusion in air is 2.5 [9].

The Sherwood number results will be parameterized by the Reynolds number. The velocity that appears in the Reynolds number was evaluated at the minimum free flow area $A_{min}$, so that $\rho V = \dot{w}/A_{min}$, where $\dot{w}$ is the flowrate of the air. In addition, the cylinder diameter D was used as the characteristic dimension. Thus,

$$Re = (\dot{w}/A_{min})D/\mu \tag{3}$$

In the present array, $A_{min} = \frac{1}{2}S^2$.

Mass (heat) transfer results. The Sherwood number results will be presented in terms of the ratio $Sh/Sh_{fd}$. In the ratio, the quantity $Sh$ represents the per-tube Sherwood number at any site of interest in the array, while $Sh_{fd}$ is the fully developed per-tube Sherwood number. Both $Sh$ and $Sh_{fd}$ correspond to the same Reynolds number. With regard to $Sh_{fd}$, it is known that an axially periodic flow pattern is established in a tube bank at sufficient distances from the inlet face. The periodic flow pattern gives rise to axially unchanging values of the per-tube Sherwood (or Nusselt) number, as was affirmed by the present experiments. The $Sh_{fd}$ values measured here for $Re = 1000$ and 8600 are 30.45 and 117.3, respectively.

The Sherwood number ratios are presented in Figs. 4 -6. Each of these figures is a plan-view layout of the array. Adjacent to each tube (excluding the half tubes at the sides), there is a trio of numbers. These numbers are the $Sh/Sh_{fd}$

values for the tube. The topmost number of each trio is for the L*/S = 0.8 delivery duct, the middle number is for the L*/S = 2.5 duct, and the lowermost number is for L*/S = 4.5. This identification pattern is illustrated near the top of each figure. The specification of whether a given trio corresponds to the tube at its right or at its left will be made shortly. Figure 4 conveys the results for the parallel orientation, while Figs. 5 - 6 are for the perpendicular orientation. The presentation will begin with the parallel orientation.

From a consideration of the diagram in Fig. 3, it is apparent that for the parallel orientation, the bend does not introduce any flow asymmetries along a given row. Therefore, in any row, symmetry should prevail with respect to a plane that is parallel to the sidewalls and situated midway between them. Advantage has been taken of this symmetry in the presentation of results in Fig. 4. The left half of the figure contains the results for Re = 1000, with each trio referring to the tube at its right. In the right half of the figure are the results for Re = 8600. Here, each trio refers to the tube at its left.

To provide perspective for the resuts of Fig. 4 (as well as for Figs. 5 and 6), Table 1 conveys $Sh/Sh_{fd}$ values for the case where the flow enters the inlet section of the tube bank without imposed maldistributions. The values listed in the table are from [2] and [3].

Both Fig. 4 and Table 1 confirm the well-established fact that the lowest transfer coefficients occur in the first row of the tube bank, with row-to-row increases in response to increased turbulence and mixing. One of the main points of interest in the figure is the effect of the bend-to-inlet distance L*/S on the $Sh/Sh_{fd}$ ratios. In the initial rows of the tube bank (rows 1 - 3), there is a general trend toward larger $Sh/Sh_{fd}$ values for smaller bend-to-inlet distances. This trend is plausible in that larger disturbances should reach the tube bank from a bend that is nearer to the inlet of the bank. The variation of $Sh/Sh_{fd}$ with L*/S is, however, modest--eight percent, at most. Furthermore, beyond the third

row, the $Sh/Sh_{fd}$ ratios are insensitive to $L*/S$.

It is also relevant to note that the $Sh/Sh_{fd}$ values of Fig. 4 are within ten percent of those of Table 1. Therefore, although the presence of the bend serves to enhance the mass (or heat) transfer in the initial rows, the enhancement is surprisingly small. Overall, on the basis of the present measurements, it appears that the presence of a bend installed in the parallel orientation does not require a tube-bank design procedure different from that used for the bend-free case.

Further inspection of Fig. 4 shows that the $Sh/Sh_{fd}$ values for a given row (and at a given Reynolds number) are relatively uniform. There are no significant effects of the sidewalls in evidence.

Attention will now be turned to the $Sh/Sh_{fd}$ results for the perpendicular orientation. Consideration of Fig. 2 suggests that for this orientation, the non-uniform flow spawned by the bend will give rise to Sherwood number variations along a given row, at least in the initial rows of the tube bundle. Therefore, the symmetry-based format used in Fig. 4 for the parallel orientation is not appropriate for the perpendicular orientation. As a consequence, the results for the perpendicular orientation are presented in two figures, Figs. 5 and 6, respectively for Re = 1000 and Re = 8600. In these figures, each trio of numbers refers to the tube at its left. As before, each number in a trio represents a value of $Sh/Sh_{fd}$, which, from upper to lower, corresponds to $L*/S = 0.8$, 2.5, and 4.5. The position of the bend relative to the tube bank is illustrated schematically at the lower left of each figure.

In appraising Figs. 5 and 6, it is relevant to observe not only how $Sh/Sh_{fd}$ at a given tube varies with $L*/S$ but also how $Sh/Sh_{fd}$ varies along a row. In addition, it is appropriate to compare the $Sh/Sh_{fd}$ values of the figures with those of Table 1 for the no-maldistribution case.

Turning first to Fig. 5 and to the results for the lower of the two Reynolds numbers, it is seen that bend-related effects are in evidence in the first five

rows. At any tube in these rows, the variation of $Sh/Sh_{fd}$ with L*/S is, at most, about seven percent--again, a rather modest effect. In general, the largest Sherwood numbers correspond to the smallest L*/S.

At a given L*/S, the variation of $Sh/Sh_{fd}$ within a given row is as large as fifteen percent, but more typical variations are ten percent or less. In general, $Sh/Sh_{fd}$ increases from left to right along a row, that is, in the direction from the inside to the outside of the bend. This trend is consistent with the packing of the flow to the outside of the bend. It is, however, surprising that the largest inter-row variations of $Sh/Sh_{fd}$ do not occur in the first row; rather, they occur in the second row and to a slightly lesser extent in the fourth row. Also somewhat surprising is the slight dropoff which occurs at the right-hand end of the second row. All of the unexpected trends were double checked and even selectively triple checked. The check runs were always consistent to within two percent or better.

Upon comparing Fig. 5 with Table 1, it is seen that there are local bend-related enhancements as large as ten percent. However, on a row-average basis, the enhancement is lower. Overall, it appears that for low Reynolds numbers (Re ∿ 1000), the bend-related effects for the perpendicular orientation are not major.

The results corresponding to the perpendicular orientation and to the higher Reynolds number (Re = 8600) will now be discussed with reference to Fig. 6. Here, the main effects of the bend are confined to the first four rows, with residual effects in the fifth row and an interesting reversed maldistribution in later rows (e.g., ninth row) which will be discussed shortly. Aside from isolated sites in the first row, the variation of $Sh/Sh_{fd}$ with L*/S at a given tube is ten percent or less. For the most part, the largest $Sh/Sh_{fd}$ corresponds to the smallest L*/S but with occasional exceptions.

Inter-row variations of $Sh/Sh_{fd}$ at a given L*/S are also in evidence. These variations are most marked in the first four rows and are greatest in the third

and fourth rows (up to fifteen percent). In general, within a given row, $Sh/Sh_{fd}$ increases in the direction from the inside to the outside of the bend (left to right), as expected. However, unexpectedly, the variation of $Sh/Sh_{fd}$ along the first row for L*/S = 0.8 is opposite in direction. This trend was verified by numerous check runs, and it will be illuminated by the flow visualization results. The trendwise opposite inter-row variations in the first row exaggerate the differences in $Sh/Sh_{fd}$ with L*/S at a given tube.

The slight dropoff at the right-hand end of the second row, already noted in Fig. 5, recurs in Fig. 6.

In row nine, for L*/S = 0.8, $Sh/Sh_{fd}$ tends to decrease (albeit slightly) from left to right. This behavior actually occurs in rows 8 - 11, but dies away thereafter. It is believed due to a secondary maldistribution which occurs because the flow overreaches itself as it attempts to recover from the primary maldistribution.

From a comparison of Fig. 6 with Table 1, it is seen that at certain tubes in the first row, there are bend-related enhancements of up to about 15 percent. However, only for the L*/S = 0.8 case does the row-average enhancement approach this value. In subsequent rows, there are local enhancements as large as eight percent, but the row average is hardly enhanced. Thus, for the orientation and Reynolds number in question, the effects of the bend are quite localized and do not have a major effect on the performance of the tube bank as a whole. Upon reviewing the discussion of Figs. 4 and 5, it appears that the foregoing conclusion applies to all the cases investigated here.

Pressure drop. A representative measured pressure distribution is presented in Fig. 7, where the data are for the case of the parallel orientation, L*/S = 4.5, and Re = 8600. The ordinate displays the dimensionless pressure difference $(p_{atm} - p)/\frac{1}{2}\rho V^2$, where $p_{atm}$ is the pressure in the ambient from which the air was drawn, and p is the local pressure. Note that $p < p_{atm}$ because the apparatus was operated in the suction mode. Consequently, increases in $(p_{atm} - p)$ correspond

to a pressure drop.  The quantity $\frac{1}{2}\rho V^2$ is a representative velocity head which is a constant for each case.  It was evaluated as

$$\frac{1}{2}\rho V^2 = \frac{1}{2}\dot{w}^2/\rho A_{min}^2 \qquad (4)$$

where $\rho$ is the mean density in the tube bank.  The value of $\frac{1}{2}\rho V^2$ from equation (4) is, strictly speaking, only appropriate for the tube bank.  However, it was employed throughout the entire flow circuit so that the distribution of $(p_{atm} - p)/\frac{1}{2}\rho V^2$ would truly reflect the distribution of $(p_{atm} - p)$.

On the abscissa, X = 0 corresponds to the inlet of the tube bank.  The data for the delivery duct are plotted to the left of X = 0.  In this range, the abscissa variable is X/S, where X is the distance from the tube bank inlet measured upstream along the duct centerline.  To the right of X = 0 are the data for the tube bank and beyond.  The abscissa variable in this range is the row number.  Note that the last three data points correspond to pressure taps which are downstream of the tube bank, in the redevelopment duct (S x S square cross section).

At the upstream end of the delivery duct, there is a  dropoff in the data (i.e., a pressure rise).  This dropoff corresponds to a pressure recovery which reflects the expansion of the flow downstream of the separation caused by the sharp-edged inlet.  Beyond the third pressure tap and continuing to the corner of the L, the pressure appears to be constant.  Actually, there is a friction-induced pressure drop, but it is too small to be shown in the figure.

At the corner of the L, there is a pressure drop due to turning losses and separation, followed by a partial pressure recovery as the flow expands to fill the duct cross section.  Thereafter, a regime of virtually uniform pressure is established, once again reflective of the extremely small friction-related pressure drop in the duct.

In the tube bank, the first pressure tap is situated midway between the second and third rows, and successive taps are separated by two rows.  The data points for the tube bank fall on a straight line, suggestive of fully developed flow.

Downstream of the bank, the pressure again appears to be virtually uniform.

The pressure drop $\Delta p_{tot}$ for the flow circuit as a whole is of interest because it reflects the net result of differences in L*/S and delivery duct orientation. The value of $\Delta p_{tot}/\frac{1}{2}\rho V^2$ was determined from the data at the three pressure taps situated downstream of the tube bank. Numerical values of this quantity are listed in Table 2 for all of the operating conditions of the experiments. Inspection of the table indicates that for a given Reynolds number, $\Delta p_{tot}/\frac{1}{2}\rho V^2$ is virtually independent of the delivery duct orientation and of L*/S. Indeed, $\Delta p_{tot}$ is even less sensitive to these parameters than were the Sherwood number results. This outcome is quite plausible since $\Delta p_{tot}$ is an overall quantity while the Sherwood numbers were referred to individual tubes.

The linear p vs X distribution in the tube bank enabled the evaluation of the fully developed friction factor for the bank. If $\Delta p_{row}$ denotes the per-row pressure drop in the linear region, then the friction factor may be evaluated from

$$f_{fd} = \Delta p_{row}/\frac{1}{2}\rho V^2 \tag{5}$$

where $\frac{1}{2}\rho V^2$ is from equation (4). For Re = 1000 and 8600, the respective $f_{fd}$ are 0.46 and 0.36 with a scatter of $\pm$ 2 percent.

Flow visualization. The flow visualization work did not yield as much information as was sought. At low Reynolds numbers, the shear stresses were not large enough to move the most fluid of the oil-lampblack mixtures that were prepared. At the highest attainable Reynolds number ($\sim$ 8600), the shear stresses were of sufficient strength, but another difficulty was encountered. With the airflow activated, globules of the mixture collected at the rear of each tube and were held in place by the aerodynamic forces. When the airflow was terminated, the forces vanished and the accumulated mixture tended to spread over adjacent parts of the floor of the test section, obscuring a portion of the flow pattern traces.

For these reasons, the presentation of the flow visualization results is

necessarily quite limited. Also, as noted earlier, the oil-lampblack technique, as employed here, yielded information only about the flow pattern adjacent to the floor of the test section.

The flow visualization results are presented in Fig. 8 via two photographs. The white circles in these photographs correspond to the positions of the tubes. At the respective edges, the white regions are approximate half circles (difficulties in cutting the contact paper were responsible for the imperfections).

Photograph (a) shows a typical flow pattern in the fully developed regime. As noted in the figure, the wakes from the tubes in the adjacent upstream row are deployed along the lower edge of the photo. Between each pair of adjacent wakes is a black zone which is termed a stagnation island in the figure. It is relevant to note that each such island is centered directly in front of a tube. The stagnation at each island is the result of two opposing streams. One is the mainflow, which is moving in the forward direction. The second stream is a backflow which issues from the lower portion of the tube and moves upstream along the floor. Still another array of stagnation zones is in evidence in the photo, with each zone situated just downstream of a wake. These zones are caused by the collision of two streams entering the lane between two adjacent tubes.

Attention may now be turned to photograph (b). This photograph shows the first row of the tube bank for the case of the perpendicular array, L*/S = 0.8, and Re = 8600. It may be recalled that in the discussion of Fig. 6, the first-row Sh values for this case did not increase from left to right, as was expected.

There are many differences between the flow patterns of photographs (a) and (b), many of which reflect the difference between the first row and the fully development regime. However, the altered positioning of the stagnation islands is not attributable to this. It is relevant to note that the stagnation islands in photograph (b) are not located directly in front of the tubes as in photograph (a) (see arrow identifying a stagnation island in (b)).

From the discussion in the next to the last paragraph, it is clear that the position of the stagnation island tells the direction from which the fluid approaches the tube. This direction can be obtained by connecting the center of the island with the axis of the tube. Thus, relative to the nominal mainflow direction, the flow arrives at the leftmost tube of photograph (b) at $45^\circ$, and the adjacent tubes also display large arrival angles.

This finding indicates that whereas the flow may have packed to the outside of the bend, by the time it reaches the first row of the tube bank it is moving diagonally in order to fill the cross section. Also, considering the sharpness of the streak lines, this diagonal flow is at least as vigorous at the left as at the right. These observations help explain the inter-row distribution of $Sh/Sh_{fd}$ in the first row of Fig. 6 for $L*/S = 0.8$.

## CONCLUDING REMARKS

The work described here appears to be the first systematic study of the response of a heat exchanger to a right-angle bend situated upstream of the exchange inlet cross section. Experiments were performed for a tube-bank-type crossflow heat exchanger with the tubes positioned on equilateral triangular centers with a transverse pitch-to-diameter ratio of two. The tube bank was housed in a square duct (side S), and the L-shaped duct which delivered air to the tube bank was of the same square cross section.

The effects of two geometrical parameters were investigated. One parameter is the distance $L*$ between the bend and the inlet of the tube bank, with the investigated values being $L*/S = 0.8$, 2.5, and 4.5. The other geometrical parameter is the orientation of the bend in the L-shaped delivery duct with respect to the axes of the tubes in the bank. Two orientations were considered. In one, the plane of the L is parallel to the tube axes, while in the other, the plane of the L is perpendicular to the axes. For each configuration (given $L*/S$ and orientation), experiments were carried out for Reynolds numbers of 1000 and 8600.

For each case defined by L*/S, orientation, and Reynolds number, the per-tube Sherwood number was measured at each relevant tube site in the array (the Sherwood number is the mass transfer counterpart of the Nusselt number). Pressure distributions were also measured along the delivery duct and the tube bank. A limited flow visualization study was also performed.

In general, it was found that the presence of the right-angle bend did not have a major effect on the heat transfer characteristics of the tube bank. For the closest proximity of the bend, individual tube transfer coefficients exceeded those for the no-bend case by ten percent (in the extreme, by fifteen percent). The departures were confined to the initial rows (first three or four rows) of the bank. Smaller bend-related effects were sustained for larger distances between the bend and the inlet of the tube bank. Row-average transfer coefficients deviated from the no-bend case by smaller percentages than the aforementioned individual tube deviations.

With the bend in the parallel orientation, there were no inter-row nonuniformities. However, the perpendicular orientation introduced inter-row variations in the transfer coefficient, with the extreme variation being fifteen percent.

The system pressure drop (from delivery duct inlet to tube bank exit) was even less sensitive to the geometrical parameters (L*/S and orientation) than was the per-tube transfer coefficient.

Overall, it appears that the presence of a right-angle bend does not require a tube-bank design procedure different from that for the no-bend case.

## ACKNOWLEDGEMENT

## REFERENCES

1. S. Kakac, R. K. Shah, and A. E. Bergles, Low Reynolds Number Heat Exchangers. Hemisphere, Washington, D.C. (1982).

2. E. M. Sparrow and R. Ruiz, Effect of blockage-induced flow maldistribution on the heat transfer and pressure drop in a tube bank, J. Heat Transfer 104, 691-699 (1982).

3. E. M. Sparrow and A. A. Yanezmoreno, Heat transfer in a tube bank in the presence of upstream cross-sectional enlargement, Int. J. Heat Mass Transfer 26 (in press).

4. J. P. Chiou, Thermal performance deterioration in crossflow heat exchanger due to flow nonuniformity, J. Heat Transfer 100, 580-587 (1978).

5. A. C. Mueller, An inquiry of selected topics on heat exchanger design, Donald Q. Kern Award Lecture, 16th National Heat Transfer Conference, August, 1976.

6. B. A. Dobryakov, The calculation of heat exchanger equipment with crossflow of the heat transfer agents, Int. Chem. Engng 13, 81-84 (1973).

7. J. A. Kutchey and H. L. Julien, The measured influence of flow distribution on regenerator performance, SAE Trans. 83, paper no. 740164 (1974).

8. W. Merzkirch, Flow Visualization. Academic Press, New York, 53-56 (1974).

9. H. H. Sogin, Sublimation from discs to air streams flowing normal to their surfaces, Trans. Am. Soc. Mech. Engrs. 80, 61-71 (1958).

Table 1

Sh/$Sh_{fd}$ without Inlet-Section Flow Maldistribution

| Row | Re | |
|-----|--------|--------|
| | 1000 | 8600 |
| 1 | 0.74 | 0.64 |
| 2 | 0.86 | 0.83 |
| 3 | 0.93 | $\sim$1.0 |
| 4 | $\sim$1.0 | |

Table 2

Values of $\Delta p_{tot}/\frac{1}{2}\rho V^2$

| Re | Orient. | L*/S | | |
|------|---------|-----|-----|-----|
| | | 0.8 | 2.5 | 4.5 |
| 1000 | Par. | 7.7 | 7.5 | 7.5 |
| 1000 | Perp. | 7.7 | 7.7 | 7.5 |
| 8600 | Par. | 6.4 | 6.4 | 6.5 |
| 8600 | Perp. | 6.4 | 6.5 | 6.5 |

# FIGURE CAPTIONS

Fig. 1    Pictorial view of the experimental apparatus

Fig. 2    Illustration of the perpendicular orientation

Fig. 3    Illustration of the parallel orientation

Fig. 4    $Sh/Sh_{fd}$ values corresponding to the parallel orientation

Fig. 5    $Sh/Sh_{fd}$ values corresponding to the perpendicular orientation,

Re = 1000

Fig. 6    $Sh/Sh_{fd}$ values corresponding to the perpendicular orientation,

Re = 8600

Fig. 7    Representative pressure distribution (parallel orientation,

$L*/S$ = 4.5, Re = 8600)

Fig. 8    Flow visualization photographs

TEST SECTION

DELIVERY DUCT

TO FLOWMETER AND BLOWER

L*

6S

S

PRESSURE TAPS

Fig. 1

Fig. 2

Fig. 3

L*/S =
0.8
2.5
4.5

Fig. 4

L*/S =
0.8
2.5
4.5

Fig. 5

$L^*/S = 0.8$
2.5
4.5

14

9
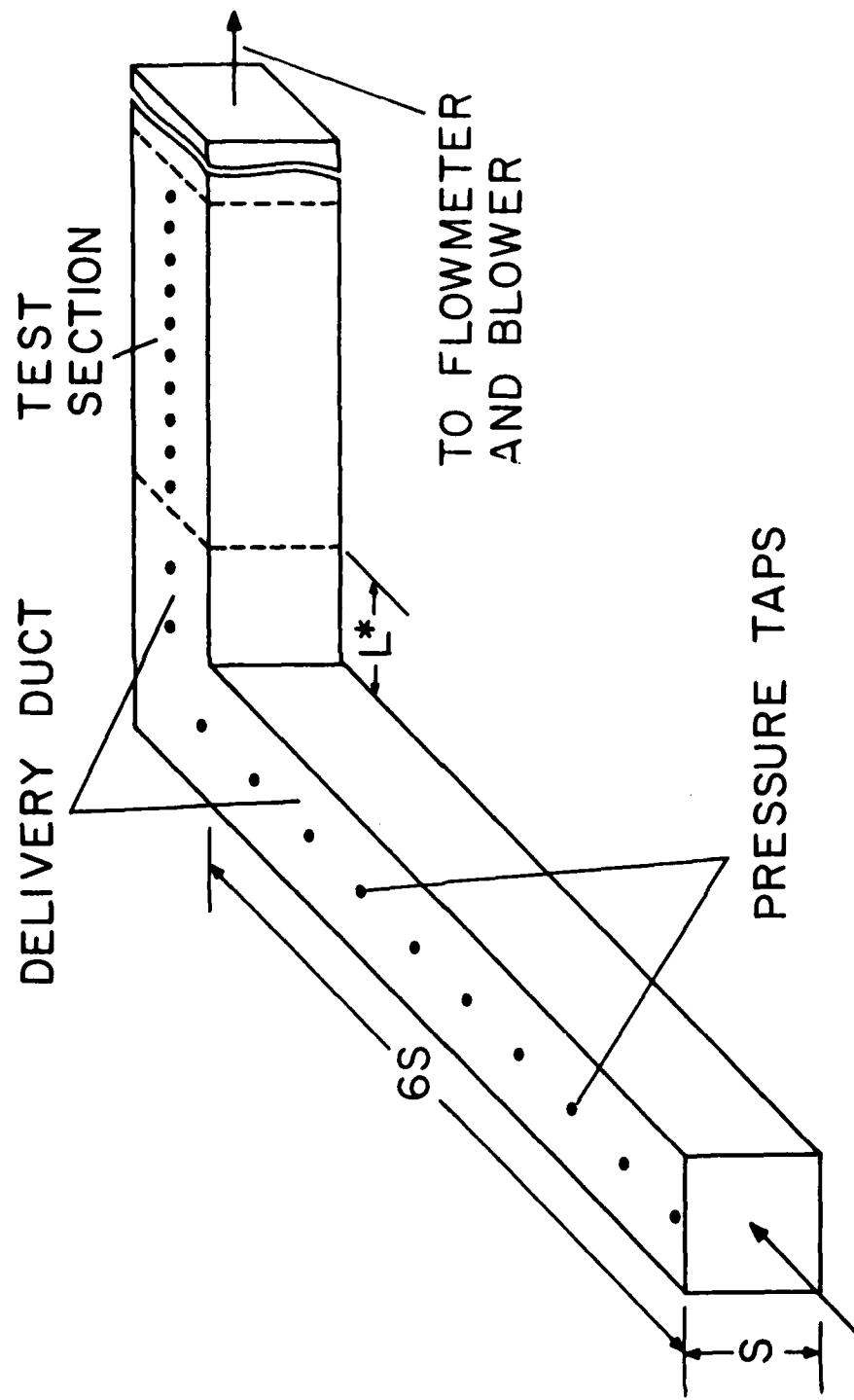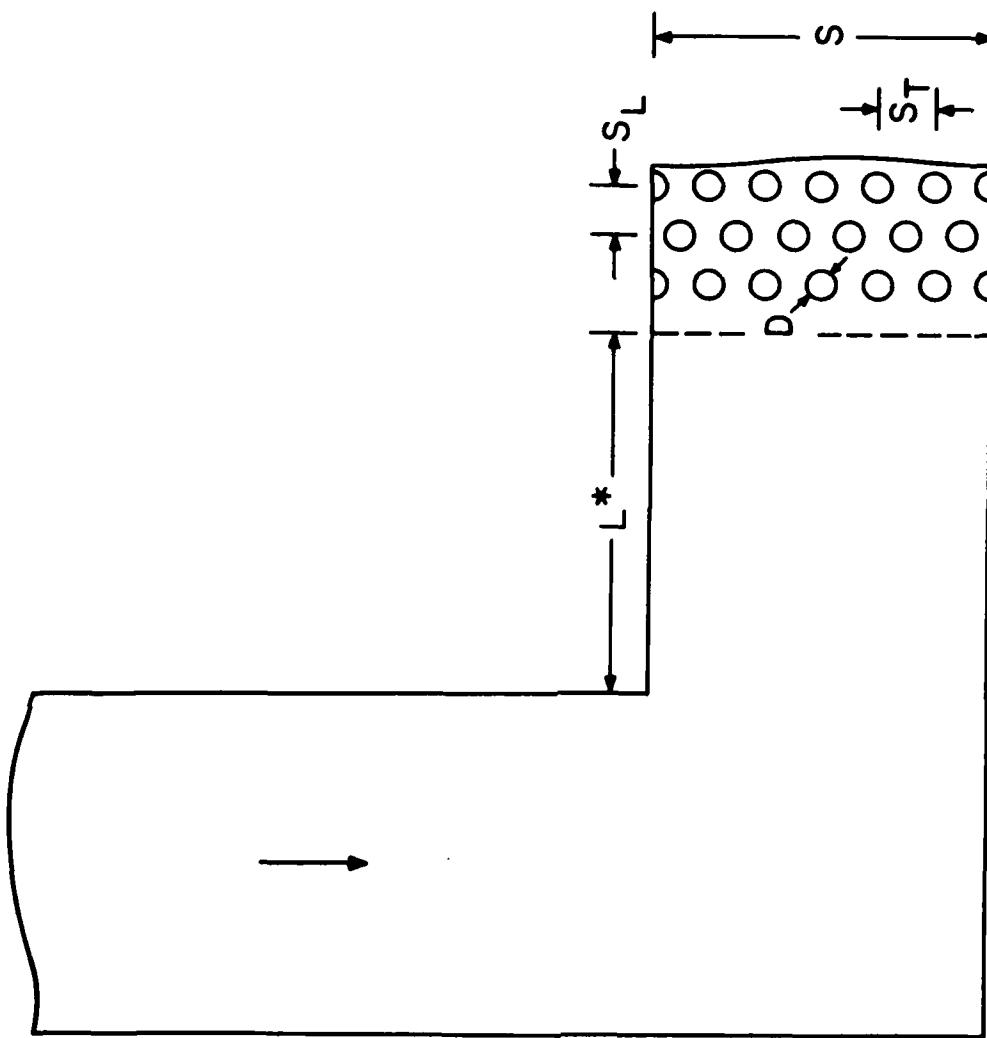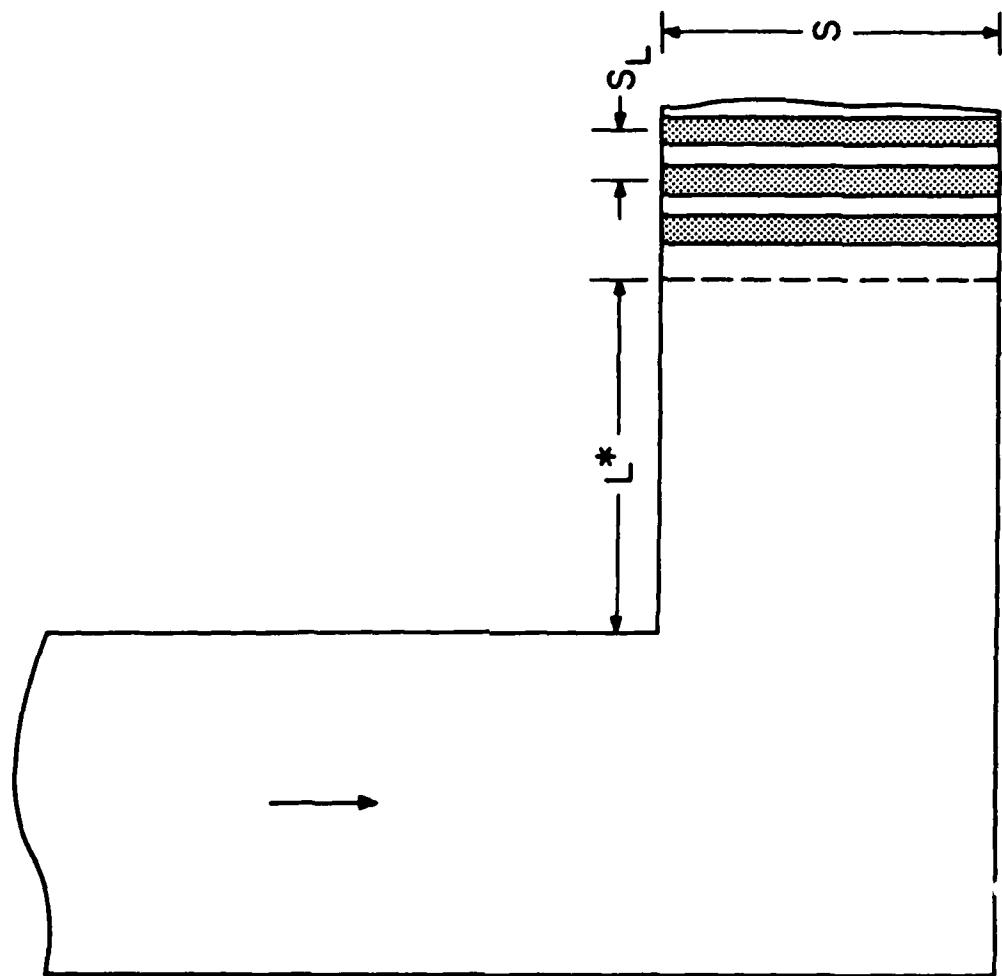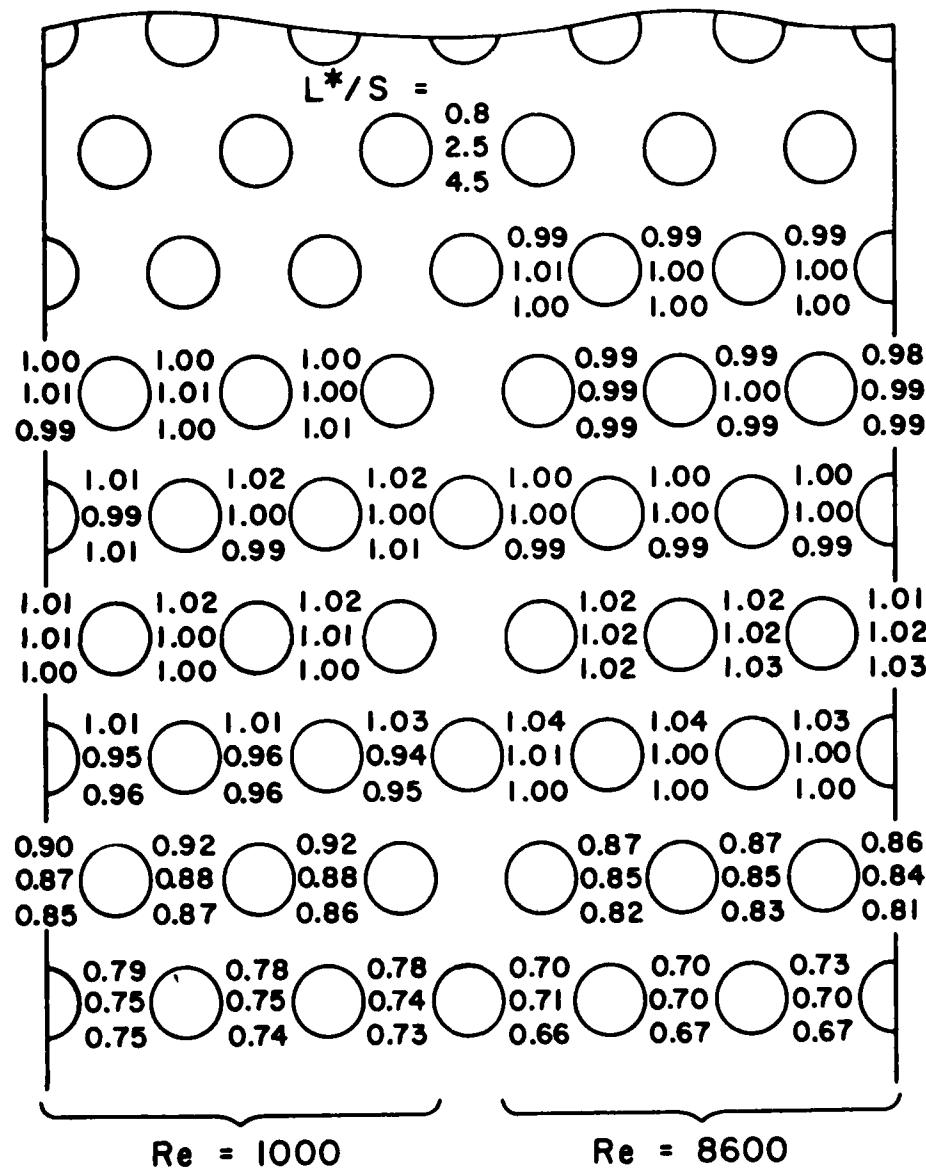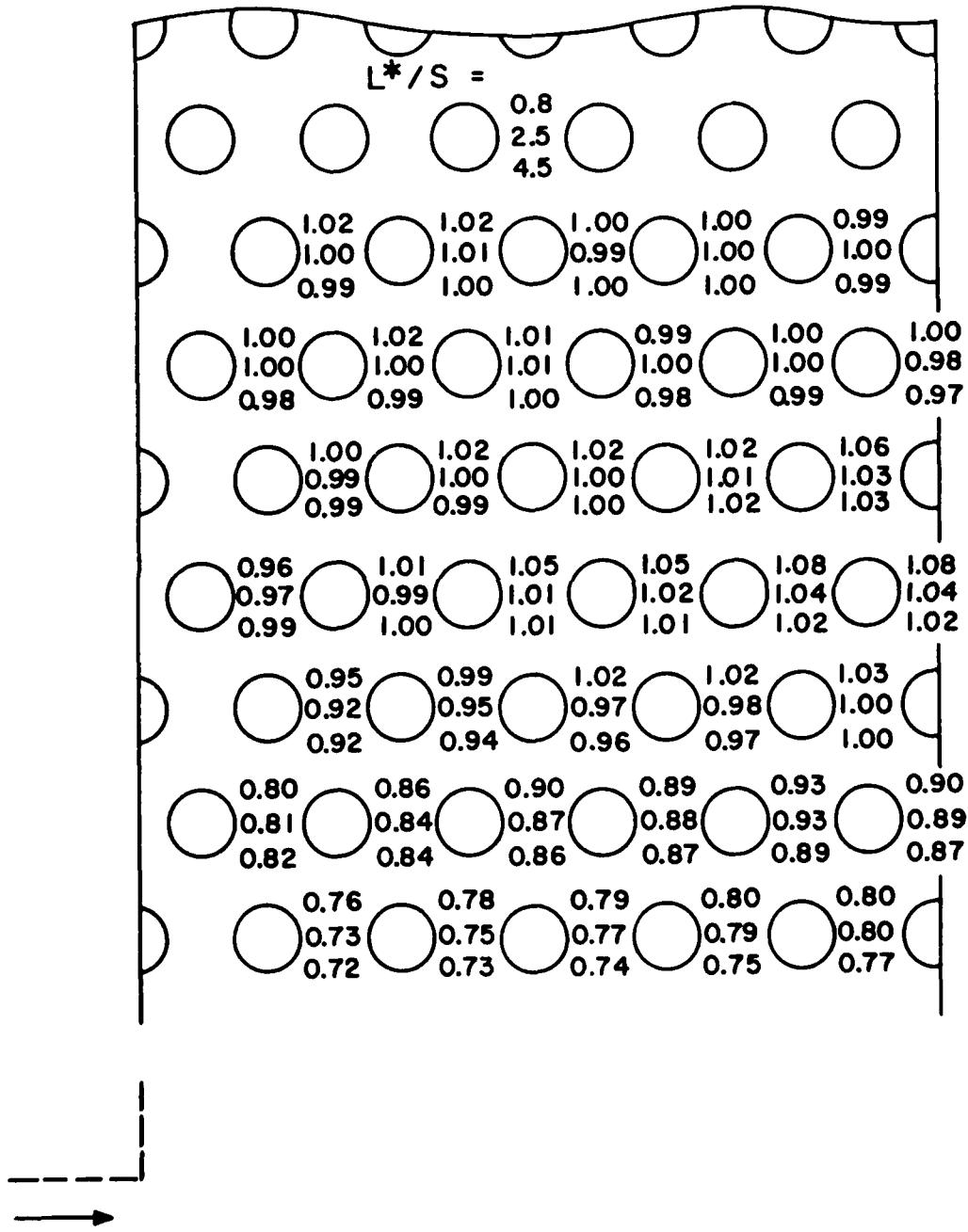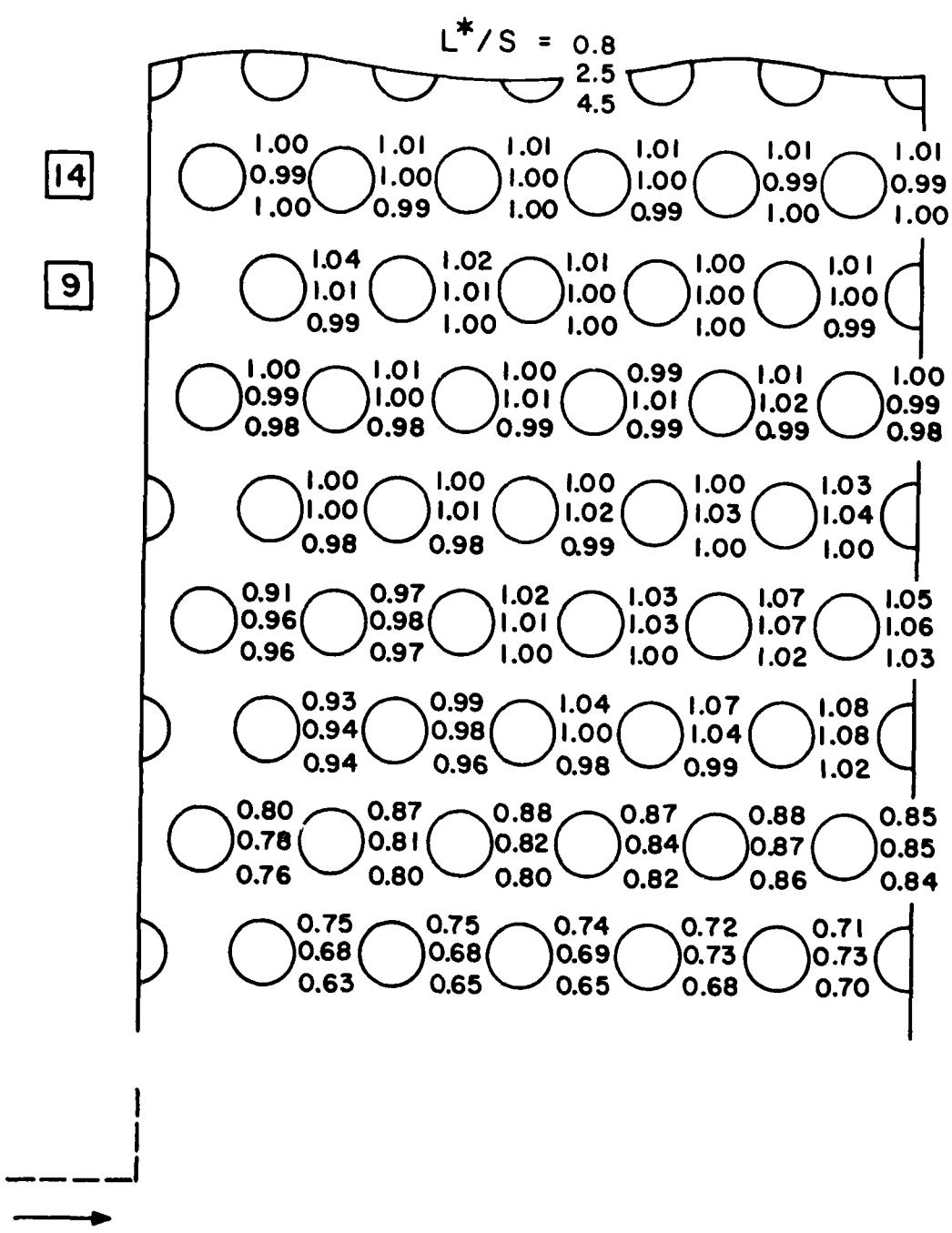
Fig.6
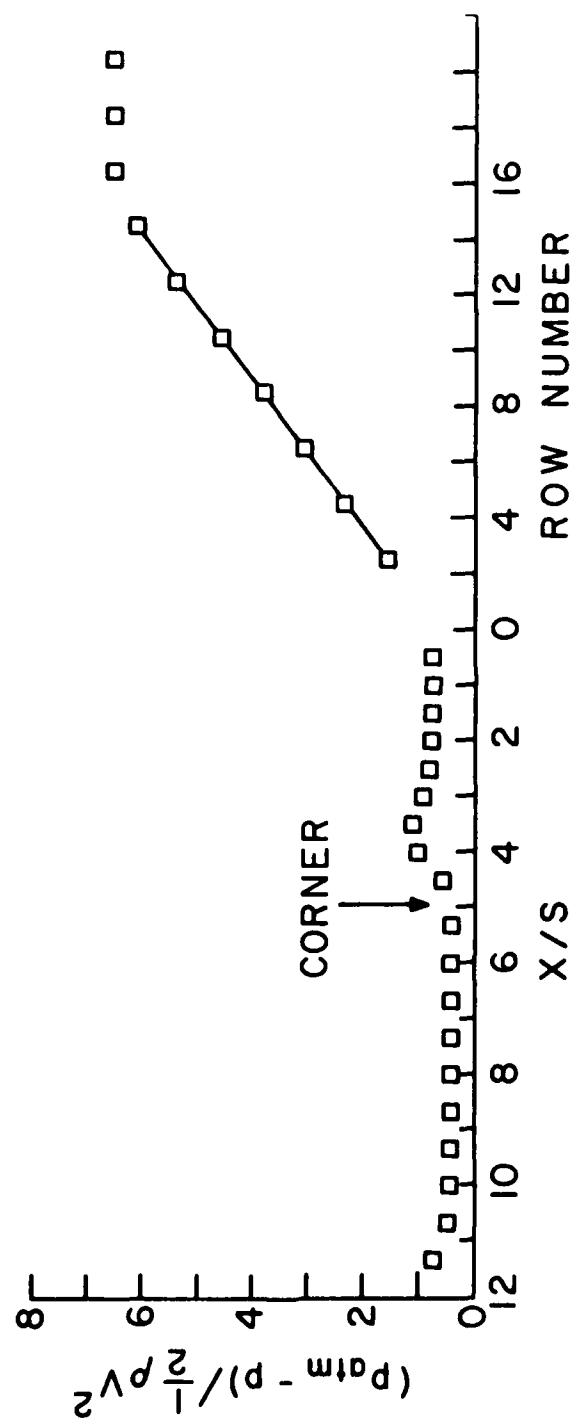
Fig. 7

FLOW
DIRECTION

(a)

STAGNATION
ISLAND

WAKE

(b)

Fig. 8

# SWIRL-AFFECTED TURBULENT FLUID FLOW AND HEAT TRANSFER

## IN A CIRCULAR TUBE

## ABSTRACT

Experiments were performed to study the fluid flow and heat transfer character-
istics for turbulent airflow in a tube in which there is a decaying axisymmetric swirl.
Measurements were made of the local swirl angle at the tube wall and of the local
Nusselt number and friction factor, all as a function of position along the length of
the tube. Supplementary flow visualizatl⋅⋅ɴ ⋅ xperiments were performed to establish the
axisymmetry of the swirl and to explore the pattern of fluid flow at the inlet of the
tube. The swirl anɴ;le was found to decay exponentially along the tube, with the decay
being more rapid at lower Reynolds numbers. The swirl gave rise to substantial heat
transfer enhancement in the initial portion of the tube. The enhancement prevailed
over a greater length of the tube at higher Reynolds numbers than at lower Reynolds
numbers. Compared with the enhancements encountered in the conventional thermal en-
trance region in a non-swirling pipe flow, those associated with swirl are substanti-
ally greater and longer lived.

## NOMENCLATURE

| | |
|---|---|
| D | diameter of test section |
| f | local apparent friction factor, equation (3) |
| $f_{fd}$ | fully developed friction factor (non-swirling flow) |
| h | local heat transfer coefficient, $q/(T_w - T_b)$ |
| k | thermal conductivity |
| L | active length of plenum chamber |
| $\dot{m}$ | mass flowrate of air |

Nu  local Nusselt number, $hD/k$

$Nu_{fd}$ fully developed Nusselt number (non-swirling flow)

p  pressure at tube wall

q  local convective heat transfer rate per unit area

Re  Reynolds number, $4\dot{m}/\mu\pi D$

$T_w$  local wall temperature

$T_b$  local bulk temperature

V  mean axial velocity

X  axial coordinate ($X = 0$ at tube inlet)

μ  viscosity

ρ  density

φ  wall swirl angle

## INTRODUCTION

This paper describes a multi-faceted experimental investigation of the heat transfer and fluid flow characteristics of a turbulent pipe flow in which there is an axially decaying swirl. The work encompassed three distinct but interrelated sets of experiments, each carried out with a separate apparatus. In the first set of experiments, measurements were made to characterize the axial distribution of the swirl strength. The second and third sets of experiments were respectively focused on the effects of the swirl on the local friction factors and heat transfer coefficients along the length of the tube.

The one common feature of the three apparatuses was the swirl generator, the function of which was to provide an axisymmetric swirling flow at the inlet of the test section tube. As described later, the generator induced the swirl by means of 224 holes drilled through the wall of a circular cylinder (i.e., the swirl chamber) so as to be tangential to the inner surface of the wall. Control of the swirl strength at the test section inlet was achieved by varying the distance at which the swirl chamber was situated upstream of the inlet. Flow visualization, documented by photographs, affirmed that the generator delivered nearly perfectly axisymmetric swirl to the inlet of the test section tube.

Air was the working fluid in all of the experiments, and the Reynolds number ranged from 9000 to 43,500. At each Reynolds number, experiments were performed for either two or three swirl strengths at the tube inlet.

The results will be presented in four parts. In the first part, photographs and diagrams documenting the key results of the flow visualization work will be displayed. The swirl decay with axial distance along the tube is presented in the next section. The third and fourth parts respectively display the axial distributions of the local friction factor and the local heat transfer coefficient.

A novel approach was used to characterize the local swirl strength. The basis of the characterization was the observation of the track of a small droplet of a

tracer fluid introduced locally at the tube wall. The direction of droplet movement along the wall from the point of its introduction is indicative of the relative magnitudes of the axial and tangential wall shear stresses. This direction can be characterized by the angle of the droplet track with respect to the axial direction, so that the angle is a measure of the ratio of the wall shears. The departure of the angle from zero will be used to characterize the strength of the swirl adjacent to the tube wall. The use of a parameter which serves as a measure of the wall-adjacent swirl appears to be particularly apt when the effects of swirl on the wall heat transfer are of major concern, as in the present investigation.

The literature on swirling pipe flows can be subdivided into papers which deal with maintained swirl (e.g., by an inserted twisted tape) or with decaying swirl--the latter being of primary relevance to the present work. A complete survey of the literature on decaying swirl is included in the thesis [1] from which this paper is drawn. Here, owing to space limitations, a somewhat abbreviated survey will be presented.

Two particularly relevant findings from the literature relate to the characterization of the initial swirl (i.e., at the tube inlet) and to the complexity of the flow. In the main, it has been customary to characterize the initial swirl by describing the device which produced the swirl, for instance, a twisted tape upstream of the test section, or the number and orientation of swirl-producing slots and baffles. Less commonly, measurements of the axial and tangential velocity profiles have been made and the cross sectional integrals of these quantities (i.e., the fluxes of tangential and axial momentum) ratioed to yield the so-called swirl number. In one investigation, the maximum tangential velocity was used to characterize the swirl. Although the aforementioned swirl number includes more detail than the other characterizations used in the literature, it, too, is not definitive because of its integral nature.

With regard to the complexity of the flow, three features are noteworthy. The first is the possibility of backflow adjacent to the tube axis in the presence of

strong swirl. Also, it has been found that the profile of the axial velocity is markedly affected by the swirl, with the maximum velocity moving from a near-wall location toward the axis as the swirl decays. The maximum tangential velocity also shows a similar movement.

The effect of swirl on pipe-flow heat transfer was investigated in [2 - 6], while, among these, only [2] included friction factor measurements. Upstream-positioned twisted tapes served both to provide and to characterize the swirl in [2] and [3]. In [4], four square slots were used to inject the gas tangentially into the tube. The angular velocity measurements reported there were made in an apparatus whose geometry differed from the heat transfer apparatus. In [5], four flat vanes were used to induce and to characterize the swirl, and only length-averaged Nusselt numbers are reported. Swirl was induced in [6] by a single slot and, in addition, the axis of the swirl-generating tube was not colinear with the axis of the heated test section tube. The resultant swirl was found to be unsymmetric.

Whereas the literature contains interesting and useful information, it also provides the impetus for further work as undertaken here.

## EXPERIMENTAL APPARATUS

In this section, the three separate apparatuses respectively used in the swirl, pressure drop, and heat transfer experiments will be described along with the swirl generator, which is common to all three. In view of the extensive amount of apparatus involved and with due regard to journal space limitations, the description will deal with the main features of the various apparatuses, with details available in [1].

Swirl generator. The swirl generator will be described with reference to diagrams (a) and (b) of Fig. 1. As seen in diagram (a), the generator consisted of two parts--the swirl chamber and the plenum chamber, which respectively served to produce the swirl and to control the strength of the swirl at the inlet of the test section. The swirl chamber was a plexiglass cylinder, capped at one end to form a cavity with an internal length of 9.8 cm, inside diameter of 7 cm, and wall thickness of 0.635 cm.

Along the portion of the cylinder shown speckled in Fig. 1(a), 224 holes, each 0.159 cm in diameter, were drilled through the chamber wall. The deployment of the holes in a typical axial cross section A-A is depicted in Fig. 1(b). As seen there, the holes were tangent to the inner surface of the cylinder wall. In each cross section, there were eight such holes separated by a uniform circumferential spacing of $45^{\circ}$. At each circumferential station, a total of 28 holes were deployed axially along the cylinder, with a center-to-center distance of 0.191 cm. The front end of the swirl chamber was framed with a 14 cm O.D. annular plexiglass disk.

The swirl chamber and its framing disk formed a closure for one end of a larger plexiglass cylinder (internal diameter and length = 14 cm and 30.5 cm, respectively), i.e., the plenum chamber. The front face of the swirl chamber could be positioned anywhere within the plenum. This enabled adjustment of the distance L between the swirl chamber exit and the inlet of the test section tube, which was situated at the downstream end of the plenum.

The simple aperture shown in the downstream wall of the plenum (Fig. 1(a)), suitable for receiving a thin-walled metallic tube of internal diameter D, is one of the three plenum--test section interfaces employed during the experiments. The pictured interface was for the pressure measurement tube. For the swirl measurement tube, a somewhat larger aperture was provided in the plenum wall. In the case of the heat transfer experiments, a portion of the wall was replaced by a thermal isolation barrier designed to minimize extraneous heat losses.

The swirl generator was operated in the suction mode, with air being drawn from the laboratory room through the tangential holes in the wall of the swirl chamber. The swirling flow passed into the plenum chamber where, depending on the active plenum length L, it was attenuated before entering the attached test section tube. A blower positioned at the downstream end of the test section provided the suction which induced the airflow. The flowrate was measured with a calibrated rotameter situated between the test section exit and the blower.

Swirl measurement tube. As was noted in the Introduction, the local swirl angle

was determined by measuring the direction of the track of a small droplet of tracer
fluid introduced at the tube wall. These measurements were performed in a segmented
tube, a typical portion of which is pictured in Fig. 1(c). As seen there, the tube
consisted of a succession of identical modules (21, in total), each of axial length
equal to 4D. The modules were of plexiglass. They were fabricated by cutting appropri-
ate lengths from solid rod stock and precision boring the internal diameter to a
finished dimension D = 2.362 cm. Protrusions and recesses were machined at the
respective ends of each module to achieve the interlocking fit pictured in Fig 1(c).

For the assembled tube, special precautions were employed to achieve straightness.
As a further defense against leaks (in addition to the interlocking fits and close
machining tolerances), pressure-sensitive tape was placed over all joints on the out-
side of the tube.

A small radial hole, 0.046 cm in diameter, was drilled through the wall of each
module to facilitate the introduction of the tracer fluid. In the assembled tube, the
holes were positioned at the low point of the circular cross section (the tube was
horizontal).

Prior to a data run, with the tube disassembled, the inside surface of each module
was covered with white, self-adhering, plasticized contact paper. The contact paper
was then pierced at the points where it covered the aforementioned tracer-fluid in-
jection holes. With the tube assembled and a steady airflow at a preselected Reynolds
number in the tube, the tracer fluid was introduced into the respective modules. This
was accomplished with a fine-bore injection needle, from which a droplet of the tracer
fluid was ejected very slowly into the radial hole. Since the system was operated in
the suction mode, the droplet was drawn through the hole and was deposited on the
contact paper adjacent to the opening, at which point it moved along the wall under
the action of the fluid shear. At the termination of the run, the tube was disassembled,
the contact paper removed from the respective modules, and the direction of the droplet
path relative to the axial direction was measured.

The tracer fluid was a mixture of lampblack powder and oil.

Pressure measurement tube. Axial pressure distributions were measured utilizing a stainless steel tube with a bore diameter of 2.362 cm and an overall length of 84 diameters. The tube was equipped with 14 pressure taps (0.089 cm tap hole) deployed along its length at axial stations which will be evident from the friction factor results to be presented later. The pressure signals were sensed by a Baratron solid-state, capacitance-type pressure meter which could be operated in three different ranges, 1, 10, and 100 Torr, with respective smallest scale divisions of $10^{-4}$, $10^{-3}$, and $10^{-2}$ Torr.

Heat transfer apparatus. The heat transfer experiments were performed with a stainless steel tube having an internal diameter of 2.362 cm, a wall thickness of 0.089 cm, and an overall length of 76 diameters. Heating was accomplished by Ohmic dissipation in the tube wall. Thermocouples were spot welded to the outside surface of the tube at 28 axial stations, with a more dense packing in the thermal entrance region (the axial positioning will be evident from the Nusselt number distributions). The thermocouple emfs were sensed and recorded by a Fluke 2240B programmable data-logger.

A number of measures were taken to minimize extraneous heat losses. For one, a portion of the plenum wall at the test section--plenum interface was replaced by a very thin (0.043 cm thick) annular disk of fiberglass. The low conductance of this disk and its minimal contact with the heated tube virtually eliminated heat losses to the plenum. A second measure was to employ guard heating/cooling to eliminate conduction along the bus bars which delivered electric current to the tube. In addition, the tube was suspended by nylon line rather than by rigid supports. Finally, the entirety of the heat transfer apparatus was housed in an insulation enclosure filled with silica aerogel (thermal conductivity $\simeq$ 80 percent of air).

## FLOW VISUALIZATION

The flow visualization was carried out using the oil-lampblack technique [7]. The purposes of the flow visualization were to establish the symmetry of the swirl, explore the flow separation and reattachment at the tube inlet, and illuminate and clarify the measurement of the wall swirl angle.

To facilitate certain of the visualization studies, it was found convenient to use an auxiliary disk situated at the downstream end of the plenum chamber as portrayed by the dashed lines in Fig. 1(a). The bore diameter of the disk was 2.362 cm, exactly equal to that of the test section tube, and its length was 2.54 cm. Thus, in effect, the disk provided a 2.54 cm upstream extension of the test section tube.

The disk (made of plexiglass) was easily inserted into and withdrawn from the plenum. Thus, with the disk outside the plenum, contact paper could be readily affixed to its upstream face or to its bore, and the oil-lampblack mixture applied to the contact paper. Then, with the disk in place at the downstream end of the plenum and the airflow activated, a visualization pattern was formed. Upon completion of the test, the disk was withdrawn from the plenum and the contact paper removed from the disk and laid flat for measurement and photography.

The first experiments to be discussed are those related to the symmetry of the swirl entering the test section tube. For these experiments, prior to the airflow period, dot-like droplets of the oil-lampblack mixture were placed on the contact-paper-covered upstream face of the disk at equal angular intervals around a circle concentric with the tube inlet. In the presence of the airflow, the droplets moved inward toward the tube inlet, and the tracks of their motion are shown in the photographs (a) and (b) of Fig. 2. Both photographs correspond to the same test section Reynolds number of 43,500 but to different active plenum lengths L, respectively L/D = 10.75 for photo (a) and L/D = 0 for photo (b).

In the absence of swirl, the droplet tracks would be radial lines. The spiral paths in evidence in Fig. 2 are, therefore, reflections of a clockwise swirl.

Qualitative inspection of the photographs indicates that the swirl is axisymmetric. This observation can be verified quantitatively by drawing rays from the center of the circle to the initial and final points of each droplet track, and then measuring the angle between the rays. For the trajectories of photograph (a), the aforementioned angle was $40.3^{\circ}$, while that for photograph (b) was $53.0^{\circ}$. The increase of the angle is indicative of stronger swirl, which is consistent with the fact that when the effective plenum length is zero, there is no opportunity for the swirl to decay in the plenum.

Next, attention will be turned to the flow pattern at the inlet of the test section tube. For these experiments, contact paper was affixed to the bore of the disk and the oil-lampblack mixture brushed on the contact paper to form a uniform film. A typical flow pattern imprinted on the contact paper is pictured in diagram (c) of Fig. 2. This pattern corresponds to a test section Reynolds number of 26,500 and to an effective plenum length $L/D = 10.75$.

Near the bottom of the diagram is a dark band which corresponds to the zone in which the flow reattaches to the tube wall after having separated at the sharp-edged inlet. This zone is centered at an axial distance of about 0.2D from the inlet cross section. The array of finely etched parallel streak lines downstream of the reattachment zone mirror the direction of the wall-adjacent flow in that region. These lines make an angle of $48^{\circ}$ with the axial direction, indicating a strong swirl component (in a swirl-free flow, the streak lines would be parallel to the axis). The somewhat irregular collection of lines upstream of the reattachment zone corresponds to the backflow leg of the recirculating flow which fills the separated region.

The final aspect of the flow visualization presentation is an illustration of the tracer droplet tracks from which the wall swirl-angle measurements were made. Figure 2(d) is a photograph which shows the actual droplet tracks at $X/d = 0$, 32, and 64 corresponding to a test section Reynolds number of 43,500 and to an effective plenum length $L/D = 12$. Had the flow been purely axial, the track would have

appeared as a vertical line. Thus, Fig. 2(d) shows the decay of the swirl along the tube, starting with a wall swirl angle of $52.5^O$ at the inlet and decreasing to an angle of $17^O$ at X/D = 64.

## SWIRL ANGLE RESULTS

Measurements of the wall swirl angle were made at as many as nine axial stations along the length of the test section. The experiments were performed for test section Reynolds numbers Re = 9000, 16,500, 26,500, and 43,500. At each Reynolds number, two initial swirl strengths were employed, respectively corresponding to the shortest and longest active plenum lengths L/D = 0 and L/D = 12.

At the higher Reynolds numbers and larger initial swirls, owing to the high shear forces exerted by the airflow, the droplet tracks were straight and crisp, enabling very accurate determination of the wall swirl angle. However, for lower Reynolds numbers and less vigorous swirls, the track was not as sharp. For these conditions and at downstream measurement stations, the residual swirl was not strong enough to move the droplet upward along the tube wall without gravity-related ambiguities. Swirl angle results are not presented at any axial station where such ambiguities were thought to be significant.

Axial distributions of the wall swirl angle are plotted in Fig. 3 for Reynolds numbers of 16,500, 26,500, and 43,500 (for the reason just cited, the Re = 9000 results are confined to a few axial stations and will be presented in a later figure). The results for all three Reynolds numbers share the same ordinate scale, but the abscissa origins are displaced to avoid overlap of the data. For each Reynolds number, data are presented for the L/D = 0 and 12 plenum lengths. Curves have been faired through the data to provide continuity, and a dashed line has been used to indicate a realistic extrapolation at downstream stations for the Re = 16,500, L/D = 12 case.

Figure 3 shows that the wall swirl angle decreases monotonically toward zero with increasing downstream distance, signalling the decay of the tangential component of

the wall shear. Furthermore, the lower the Reynolds number, the more rapid is the de-
cay. This finding is consistent with the stronger viscous forces that are operative
in lower Reynolds number flows. At the highest Reynolds number of the experiments
(i.e., Re = 43,500), an appreciable swirl remains even after a length of run of 80
diameters.

The swirl strength at the tube inlet corresponding to the zero-L/D plenum is
high, as witnessed by the wall swirl angle of approximately $60^o$ which implies a tan-
gential wall shear that is greater than the axial wall shear. The inlet-section swirl
corresponding to the L/D = 12 plenum is somewhat lower because of the dissipation which
occurs in the plenum. The dissipation is greater at lower Reynolds numbers, and this
is reflected in the variation of the initial swirl angle from $52^o$ to $44^o$ as Re varies
from 43,500 to 16,500.

Another noteworthy feature of the figure is the minimal scatter of the data.
This is to be contrasted to the scatter present in the published data for other
measures of swirl (e.g., Fig. 5 of [6]).

Another perspective on the swirl angle results is provided by Fig. 4. This is
a two-part figure in which the axial distribution of the swirl angle corresponding
to the L/D = 0 plenum are plotted in the upper part, while those for the L/D = 12
plenum are plotted in the lower part. The data in each part are parameterized by the
Reynolds number, and it is to emphasize the Reynolds number effect that the figure
has been prepared. The figure shows that with the same (or nearly the same) swirl
at the tube inlet, the decay of the swirl along the tube is much more rapid as the
Reynolds number decreases. A similar conclusion about the role of the Reynolds number
follows from the experiments of [8] and [9], where different measures of the swirl
strength were used.

The analytical work of [10] and [8], respectively for laminar and turbulent flow,
suggested that the asymptotic behavior of the decay of swirl is exponential in the
flow direction. This prompted the semi-logarithmic presentation of swirl angle data

in Fig. 5, which is, again, a two-part figure. The axial distributions for a fixed Reynolds number and parametric L/D are plotted in the upper part of the figure, while the results for a fixed L/D and parametric Re are plotted in the lower part.

The two parts of the figure demonstrate that the wall swirl angle follows an exponential law of decay and that, furthermore, the exponential behavior holds all along the tube (the slight data dropoff for Re = 16,500 and L/D = 0 is attributable to extraneous gravity effects on the tracer droplet motion). A least-squares fit of all of the semi-logarithmic data yielded

$$\text{Swirl Angle (Degrees)} = C\exp[-\beta(X/D)] \tag{1}$$

where

$$\beta = 483(\text{Re})^{-0.97} \tag{2}$$

Equation (2) indicates that the decay length constant $\beta$ varies more or less inversely with the Reynolds number. This quantitative finding about the role of the Reynolds number affirms the visual observations of Figs. 3 and 4.

## FRICTION FACTOR RESULTS

Prior to the swirl flow experiments, axial pressure distributions were measured in non-swirling flows. These distributions were of the conventional form, culminating in a linear regime downstream of the hydrodynamic entrance region. Fully developed friction factors were evaluated for the same range of Reynolds numbers as were used in the swirl flow experiments. These friction factors were compared with those given by the well-established Blasius formula, with deviations in the 1.7 - 4 percent range. This excellent agreement served to verify the instrumentation and the measurement technique.

For the swirling flows, the measured pressure distributions were used to evaluate local apparent friction factors. At each measurement station, the local pressure gradient (-dp/dX) was calculated by fitting a least-squares straight line through the pressures at that point and at the upstream and downstream neighboring points. Then, the friction factor was obtained by local application of its equation of

definition

$$f = (-dp/dX)D/\tfrac{1}{2}\rho V^2 \tag{3}$$

where $\rho V^2 = (\dot{m}/\tfrac{1}{4}\pi D^2)^2/\rho$, and $\rho$ is the local density at the point of interest.

To provide the fullest perspective for the local swirl-flow friction factors, they are presented in ratio form relative to the fully developed friction factor $f_{fd}$ for the Reynolds number of interest. The values of $f_{fd}$ used in the ratio are those determined in the present non-swirl experiments.

The results for the $f/f_{fd}$ ratio are presented in Figs. 6 and 7, where they are plotted as a function of the dimensionless axial position coordinate X/D. Figure 6 consists of two parts which respectively pertain to the upper and lower levels of the initial swirl employed in the experiments (i.e., L/D = 0 and 12). In each part of the figure, $f/f_{fd}$ distributions are plotted for Re = 9000, 16,500, 26,500 and 43,500. An overall inspection of Fig. 6 indicates a dramatic difference in the level of the friction factor at small X/D due to differences in the level of the initial swirl. It is also evident that $f/f_{fd}$ drops off more rapidly at high levels of initial swirl, so that at more downstream stations the $f/f_{fd}$ ratio should be less sensitive to the initial swirl. This issue will be explored in a more quantitative manner shortly.

The main message of Fig. 6 relates to the role of the Reynolds number. In this regard, reference may be made to the results for Re = 16,500, 26,500 and 43,500 for L/D = 0. As can be seen from either Fig. 4 or Fig. 5, the initial swirl for these cases is virtually the same. Figure 6 shows that the initial values of $f/f_{fd}$ are also nearly the same. However, with increasing downstream distance, the three distributions separate, with a more rapid decline at lower Reynolds numbers. This behavior can be attributed to the more rapid axial decay of the swirl with decreasing Reynolds number that is in evidence in Figs. 4 and 5.

In Fig. 7, the $f/f_{fd}$ distributions for Re = 9000 and L/D = 0, 6, and 12 are brought together in the left-hand part of the figure, and a similar grouping for Re = 43,500 is made in the right-hand portion of the figure. The main point of the

figure is the marked differences in the rapidity of the dropoff of $f/f_{fd}$ as a function of the initial swirl. The strongest initial swirl is that associated with L/D = 0, and the strength progressively decreases as L/D increases. Figure 7 clearly shows that the stronger the initial swirl, the more rapidly does $f/f_{fd}$ drop off. Thus, large differences in the initial values of $f/f_{fd}$ which correspond to different initial swirl strengths die away with increasing downstream distance.

The generally high values of $f/f_{fd}$ that prevail in the upstream portion of the tube are noteworthy. These high values may be attributed to two primary causes. One is the dissipation of the tangential momentum of the swirl. The other is the severe swirl-related distortions of the axial velocity profiles. In particular, the maximum axial velocity may occur near the tube wall, and this gives rise to high wall shear. Also, backflow may occur in the central core of the flow, further contributing to the dissipation of momentum.

## HEAT TRANSFER RESULTS

Local heat transfer coefficients were evaluated from the basic definition

$$h = q/(T_w - T_b) \tag{4}$$

The local convective heat flux q was determined by correcting the electric power input for axial conduction in the tube wall and for losses through the insulation which surrounds the test section. The value of $T_b$ at any axial station X was found from an energy balance on the fluid, using a control volume which extended from X = 0 to X = X and integrating the aforementioned local q values to obtain the heat input to the control volume. Values of the local wall temperature $T_w$ were available from the experimental data.

A dimensionless representation was made in terms of the local Nusselt number

$$Nu = hD/k \tag{5}$$

with k at the local bulk temperature. Variable properties were not an issue since the wall-to-bulk temperature differences were kept small (i.e., < $10^\circ$C).

Prior to the swirl-flow experiments, heat transfer data were collected for the

no-swirl case for Reynolds numbers between 9000 and 43,500. The fully developed

Nusselt numbers from these experiments were compared with those from the Petukhov-

Popov correlation (equations (8 - 23) and (8 - 24) of [11]). The average deviation

of the data from the correlation was 5.1 percent, which is within the six percent

confidence limit of the correlation. This good agreement lends confidence to the heat

transfer apparatus and instrumentation.

The local Nusselt numbers for the swirl-flow experiments will be presented in

ratio form relative to the fully developed value $Nu_{fd}$ for the same Reynolds number.

Owing to its broad acceptance, the Petukhov-Popov correlation will be used for the fully

developed Nusselt numbers.

The Nusselt number results, plotted in the form $Nu/Nu_{fd}$ vs. X/D, are reported in

Figs. 8 and 9 in a presentation format that parallels that of Figs. 6 and 7 for the

friction factor. In Fig. 8, the results for the upper level of the initial swirl,

corresponding to L/D = 0, are brought together in the left portion of the figure,

while the results for the lower initial swirl level (L/D = 12) are brought together

at the upper right. For each level of the initial swirl, axial distributions are

plotted for Re = 9000, 16,500, 26,500, and 43,500.

From the ordinate of Fig. 8, it is seen that $Nu/Nu_{fd}$ is substantially greater

than one in the initial portion of the tube. Furthermore, it will be demonstrated

shortly that these values of $Nu/Nu_{fd}$ are much greater than those which prevail in

the thermal entrance region of a pipe with a non-swirling airflow. Thus, the swirl

is highly enhancing. By comparing the results for L/D = 0 and 12, it is also evi-

dent that the Nusselt numbers in the initial portion of the tube are quite responsive

to the level of the initial swirl, being larger at stronger swirls. The dropoff of

$Nu/Nu_{fd}$ with X/D also depends on the initial swirl, and this effect will be docu-

mented shortly.

The response of the $Nu/Nu_{fd}$ distributions to changes in Reynolds number at a

fixed initial swirl can be identified by comparing the results in Fig. 8 for

Re = 16,500, 26,500, and 43,500 for L/D = 0. These cases have almost identical

initial swirl (see Figs. 4 and 5). It is seen that the lower the Reynolds number, the more rapidly does $Nu/Nu_{fd}$ drop off. Thus, swirl is more enhancing with respect to heat transfer at higher Reynolds numbers than at lower Reynolds numbers.

The aforementioned response of $Nu/Nu_{fd}$ to the Reynolds number is identical to that already encountered for the friction factor results. The more rapid dropoff of both $Nu/Nu_{fd}$ and $f/f_{fd}$ at lower Re is caused by the more rapid decay of the swirl.

In Fig. 9, the $Nu/Nu_{fd}$ distributions are grouped according to Reynolds number (for Re = 9000 and 43,500). In each group, results are given for the three swirl levels as characterized by the plenum L/D ( = 0, 6, and 12). A special feature of the presentation is the inclusion of the $Nu/Nu_{fd}$ distribution for the no-swirl case for Re = 9000. No-swirl $Nu/Nu_{fd}$ distributions were measured for all the investigated Reynolds numbers, including Re = 43,500. However, due to overlap with other plotted data, the Re = 43,500 no-swirl distribution could not be included in Fig. 9. It is, however, quite similar to that shown for Re = 9000.

Inspection of Fig. 9 shows that conventional thermal entrance region effects as occur in non-swirling flows are second order compared with those caused by swirl. For one thing, $Nu/Nu_{fd}$ decreases much more rapidly in a conventional entrance region than in a swirling flow. In addition, the magnitudes of $Nu/Nu_{fd}$ are substantially smaller for the former.

Figure 9 highlights the effects of the initial swirl on the magnitude of $Nu/Nu_{fd}$ and on the rapidity of its dropoff with X/D. It is seen that the initial magnitude of $Nu/Nu_{fd}$ is ordered with the initial swirl strength. Furthermore, the greater the initial swirl strength, the more rapidly does $Nu/Nu_{fd}$ drop off. Thus, the large initial gaps between the $Nu/Nu_{fd}$ distributions for the different initial swirls tend to diminish with increasing downstream distance.

It is relevant to seek a correlation between the $Nu/Nu_{fd}$ ratio at a given X/D and the wall swirl angle which prevails at that X/D. Such a correlation is presented in Table 1, where $Nu/Nu_{fd}$ is listed as a function of the swirl angle (now denoted by $\Phi$) for Re = 26,500 and 43,500. For each Reynolds number, results are presented for both the L/D = 0 and 12 initial swirl levels.

The table shows that for a given wall swirl angle $\Phi$, the $Nu/Nu_{fd}$ ratio is quite insensitive to the initial swirl level, especially for small and intermediate values of $\Phi$. Also, at a given $\Phi$, $Nu/Nu_{fd}$ depends only weakly on Re in the investigated range. The available swirl angle results for Re = 9000 and 16,500 are not sufficiently complete to enable a listing as extensive as that of Table 1 to be made; however, a limited tabulation for Re = 16,500 indicated a slightly greater sensitivity to the initial swirl level.

A tabulation of $f/f_{fd}$ vs. $\Phi$, similar to that for $Nu/Nu_{fd}$, is presented in Table 2. At a given Re, the table shows that $f/f_{fd}$ is nearly independent of the initial swirl level when $f/f_{fd} < \sim 4$. In the range of larger $f/f_{fd}$, the effect of the initial swirl is more pronounced. Furthermore, $f/f_{fd}$ is more sensitive to Re (at a given $\Phi$) than is $Nu/Nu_{fd}$.

## CONCLUDING REMARKS

This investigation of turbulent pipe flow with decaying swirl has encompassed three primary sets of experiments, respectively for the measurement of the local swirl angle at the tube wall and the local friction factor and Nusselt number. These quantities were determined as a function of axial position along the length of the test section tube. Supplementary flow visualization experiments were also performed to establish the symmetry of the swirl and to examine the flow pattern at the tube inlet.

A special feature of the experiments was the use of a swirl generator which pro-vided a perfectly axisymmetric swirl at the tube inlet. The swirl at any axial sta-tion was characterized by the ratio of the tangential and axial shear stresses at the tube wall. This ratio was expressed in terms of the angle between the resultant wall shear stress and the axial direction. The angle was found to decay exponentially along the length of the tube. The rate of decay was more rapid at lower Reynolds numbers.

The swirl gave rise to substantial heat transfer enhancement in the initial portion of the test section tube, the extent of which was ordered according to the initial swirl strength. For a given initial swirl, the ratio $Nu/Nu_{fd}$, which com-pares the local and fully developed Nusselt numbers, drops off more rapidly as the Reynolds number decreases. Thus, the swirl-related enhancement is longer lived at higher Reynolds numbers than at lower Reynolds numbers. At a given Reynolds number, the $Nu/Nu_{fd}$ ratio drops off somewhat more rapidly for higher initial swirls.

Compared with the $Nu/Nu_{fd}$ ratios encountered in the thermal entrance region of a conventional non-swirling pipe flow, those for the present swirl flows are sub-stantially higher, and these enhanced values persist to greater downstream distances.

The characteristics of the friction factor distributions closely parallel those of the Nusselt number distributions.

The basic data for the Nusselt number and the friction factor that have been presented here can be used as inputs to computations of the enhancement characteristics of swirl-affected pipe flows. Such enhancement evaluations may be performed for a wide variety of constraints (e.g., fixed pumping power, fixed heat duty, fixed mass flowrate, fixed transfer surface area, etc.). The actual execution of the enhancement evaluations is beyond the scope of the paper.

The present heat transfer and friction factor results could not be compared with those of the literature because it was not possible to find a common ground for the characterization of the swirl.

## ACKNOWLEDGEMENT

## REFERENCES

1.  Chaboki, A., "Heat Transfer, Pressure Drop, and Flow Visualization for Axially Decaying Swirl in a Turbulent Pipe Flow," Thesis, Department of Mechanical Engineering, University of Minnesota, Minneapolis, Minnesota, 1983.

2.  Blackwelder, R. and Kreith, F., "An Experimental Investigation of Heat Transfer and Pressure Drop in a Decaying Swirl Flow," in Augmentation of Convective Heat and Mass Transfer, ASME, 1970, pp. 102-108.

3.  Narezhnyy, E. G. and Sudarev, A. V., "Local Heat Transfer in Air Flowing in Tubes with a Turbulence Promoter at the Inlet," Heat Transfer--Soviet Research, Vol. 3, No. 2, 1971, pp. 62-66.

4.  Blum, H. A. and Oliver, L. R., "Heat Transfer in a Decaying Vortex System," ASME Paper No. 66-WA/HT-62, 1967.

5.  Zaherzadeh, N. H. and Jagadish, B. S., "Heat Transfer in Decaying Swirl Flows," International Journal of Heat and Mass Transfer, Vol. 18, 1975, pp. 941-944.

6.  Hay, N. and West, P. D., "Heat Transfer in Free Swirling Flow in a Pipe," ASME Journal of Heat Transfer, Vol. 97, 1975, pp. 411-416.

7.  Merzkirch, W., Flow Visualization, Academic Press, New York, 1974, pp. 53-56.

8.  Kreith , F. and Sonju, O. K., "The Decay of Turbulent Swirl in a Pipe," Journal of Fluid Mechanics, Vol. 22, 1965, pp. 257-271.

9.  Wolf, L., Jr., Lavan, Z., and Fejer, A. A., "Measurements of the Decay of Swirl in Turbulent Flow," AIAA Journal, Vol. 7, 1969, pp. 974-975.

10.  Talbot, L., "Laminar Swirling Pipe Flow," Journal of Applied Mechanics, Vol. 21, 1954, pp. 1 - 7.

11.  Karlekar, B. V. and Desmond, R. M., Heat Transfer, 2nd edn., West Publishing, St. Paul, 1982.

## Table 1

### Relation Between $Nu/Nu_{fd}$ and the Wall Swirl Angle $\phi$ (degrees)

| $\phi$ | L/D = | Re = 26,500 | | Re = 43,500 | |
|---|---|---|---|---|---|
| | | 0 | 12 | 0 | 12 |
| 15 | | 1.65 | 1.64 | | |
| 20 | | 1.86 | 1.83 | 1.74 | 1.76 |
| 25 | | 2.12 | 2.05 | 1.90 | 1.90 |
| 30 | | 2.35 | 2.27 | 2.10 | 2.09 |
| 35 | | 2.66 | 2.53 | 2.38 | 2.35 |
| 40 | | 2.96 | 2.83 | 2.73 | 2.60 |
| 45 | | 3.37 | 3.23 | 3.12 | 2.87 |

## Table 2

### Relation Between $f/f_{fd}$ and the Wall Swirl Angle $\phi$ (degrees)

| $\phi$ | L/D = | Re = 26,500 | | Re = 43,500 | |
|---|---|---|---|---|---|
| | | 0 | 12 | 0 | 12 |
| 15 | | 2.02 | 2.00 | | |
| 20 | | 2.55 | 2.54 | 2.05 | 1.92 |
| 25 | | 3.35 | 3.25 | 2.45 | 2.26 |
| 30 | | 4.60 | 4.05 | 3.05 | 2.95 |
| 35 | | 6.15 | 5.00 | 4.20 | 4.15 |
| 40 | | 8.25 | 6.30 | 6.10 | 5.65 |

## FIGURE CAPTIONS

Fig. 1    Diagrams depicting various features of the experimental apparatus

Fig. 2    Flow visualization results

Fig. 3    Wall swirl angle distributions grouped according to Reynolds number

Fig. 4    Wall swirl angle distributions grouped according to plenum length

Fig. 5    Demonstration of the exponential axial decay of the wall swirl angle

Fig. 6    Friction factor distributions grouped according to plenum length

Fig. 7    Friction factor distributions grouped according to Reynolds number

Fig. 8    Nusselt number distributions grouped according to plenum length

Fig. 9    Nusselt number distributions grouped according to Reynolds number

PLENUM CHAMBER

SECTION A-A
(b)

AUXILIARY
DISK

L

D

(a)

SWIRL CHAMBER

4D

D

(c)

Fig. 1

(a)

(b)

(c)

AXIAL
DIRECTION

INLET

(d)
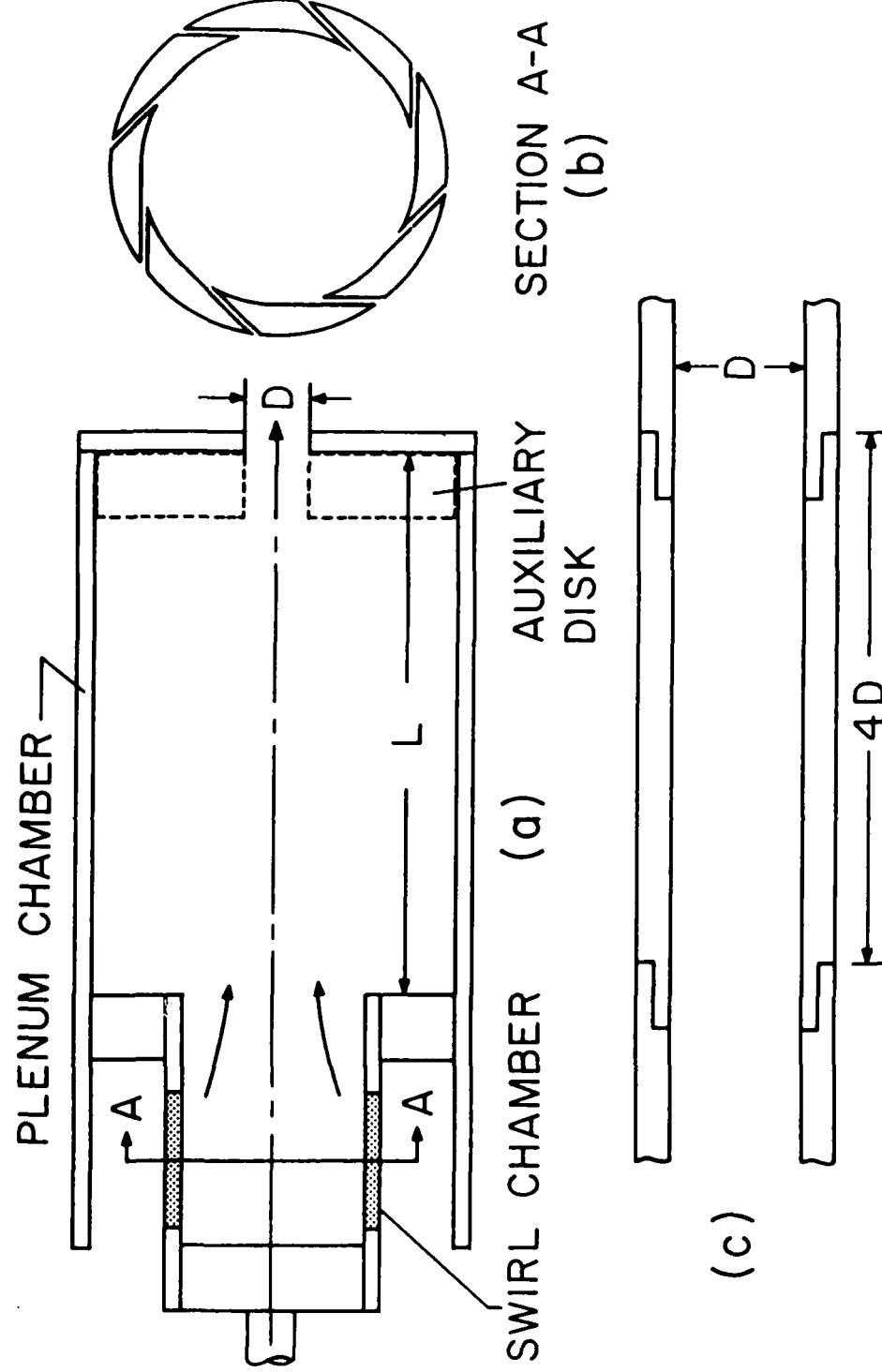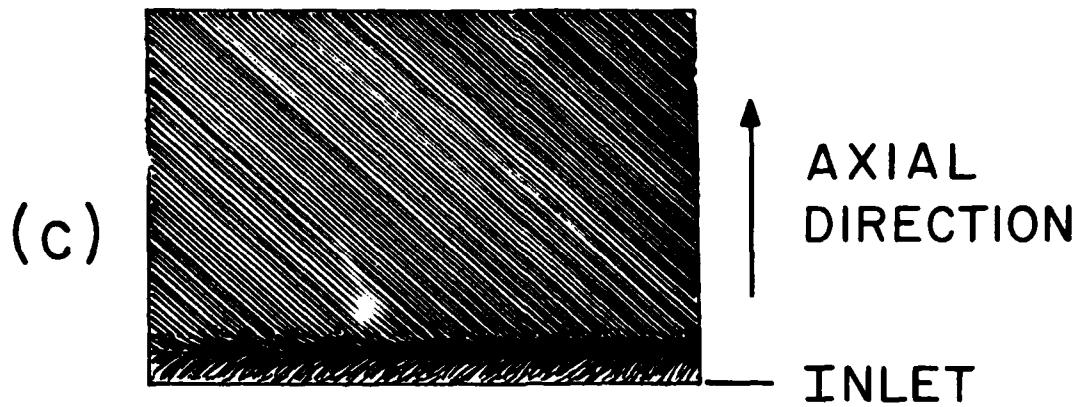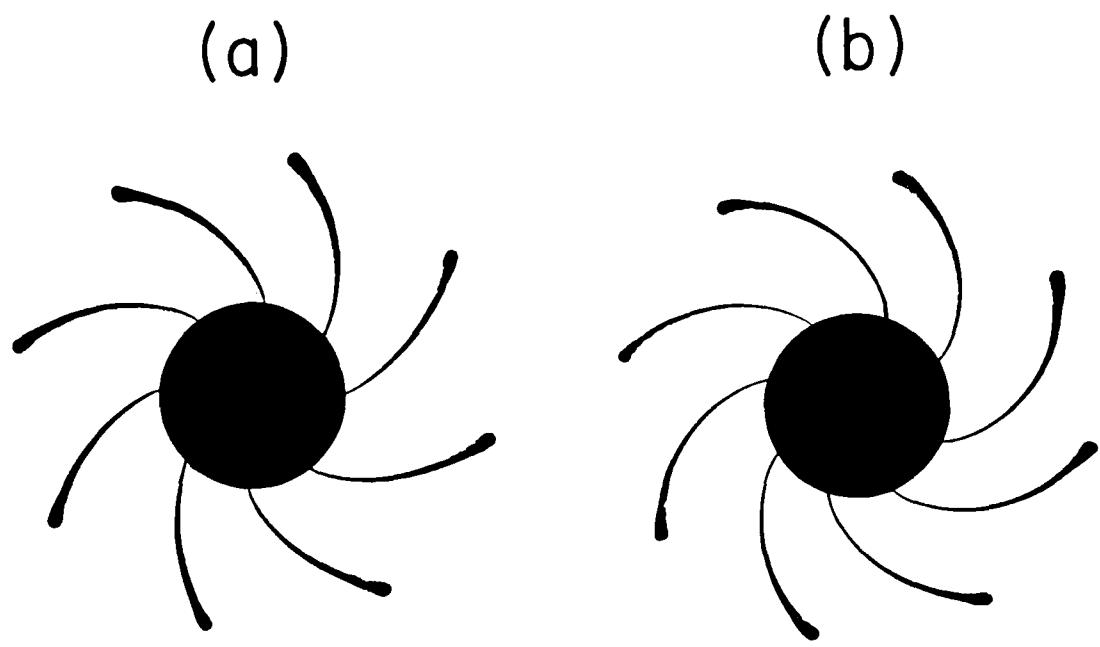
Fig. 2
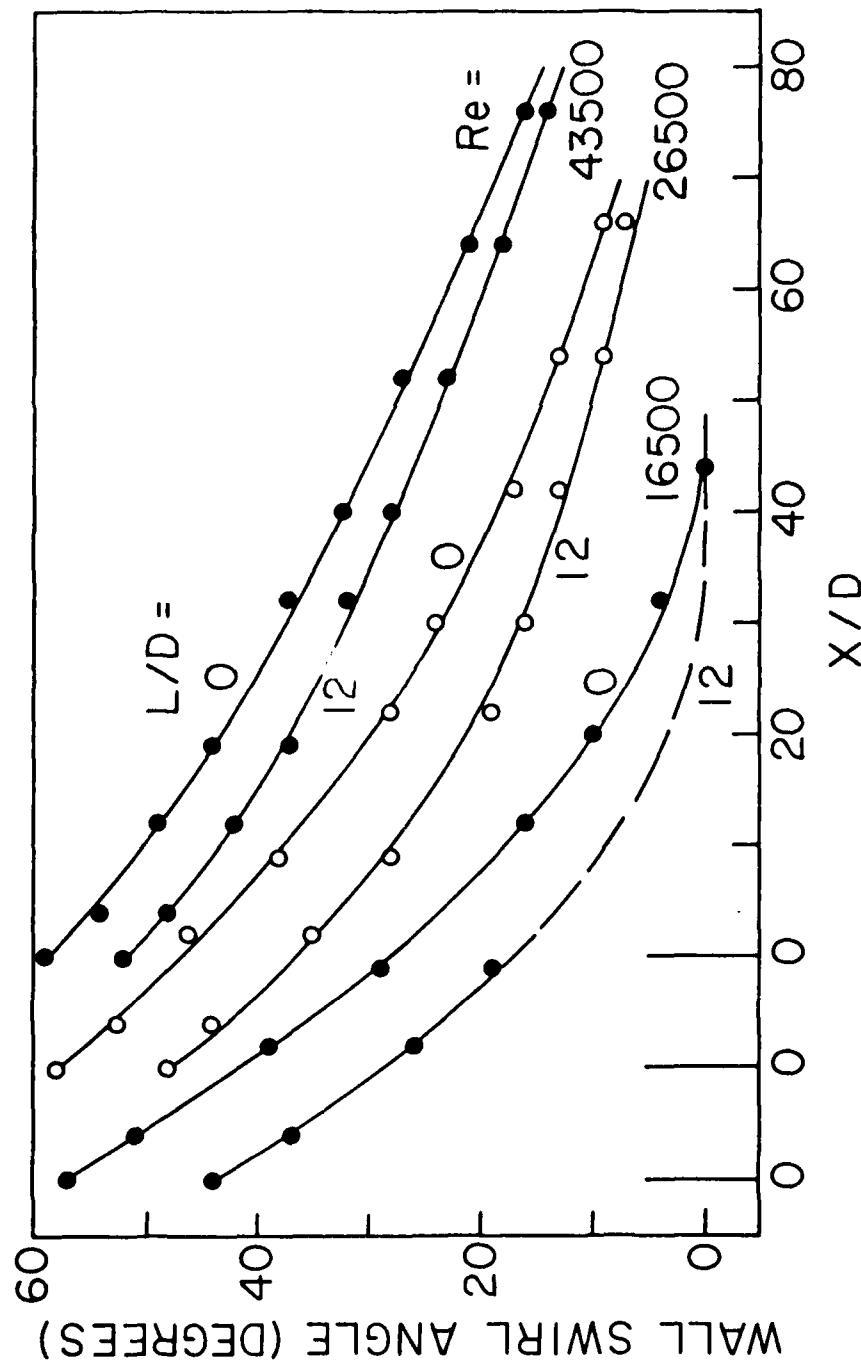
Fig. 3
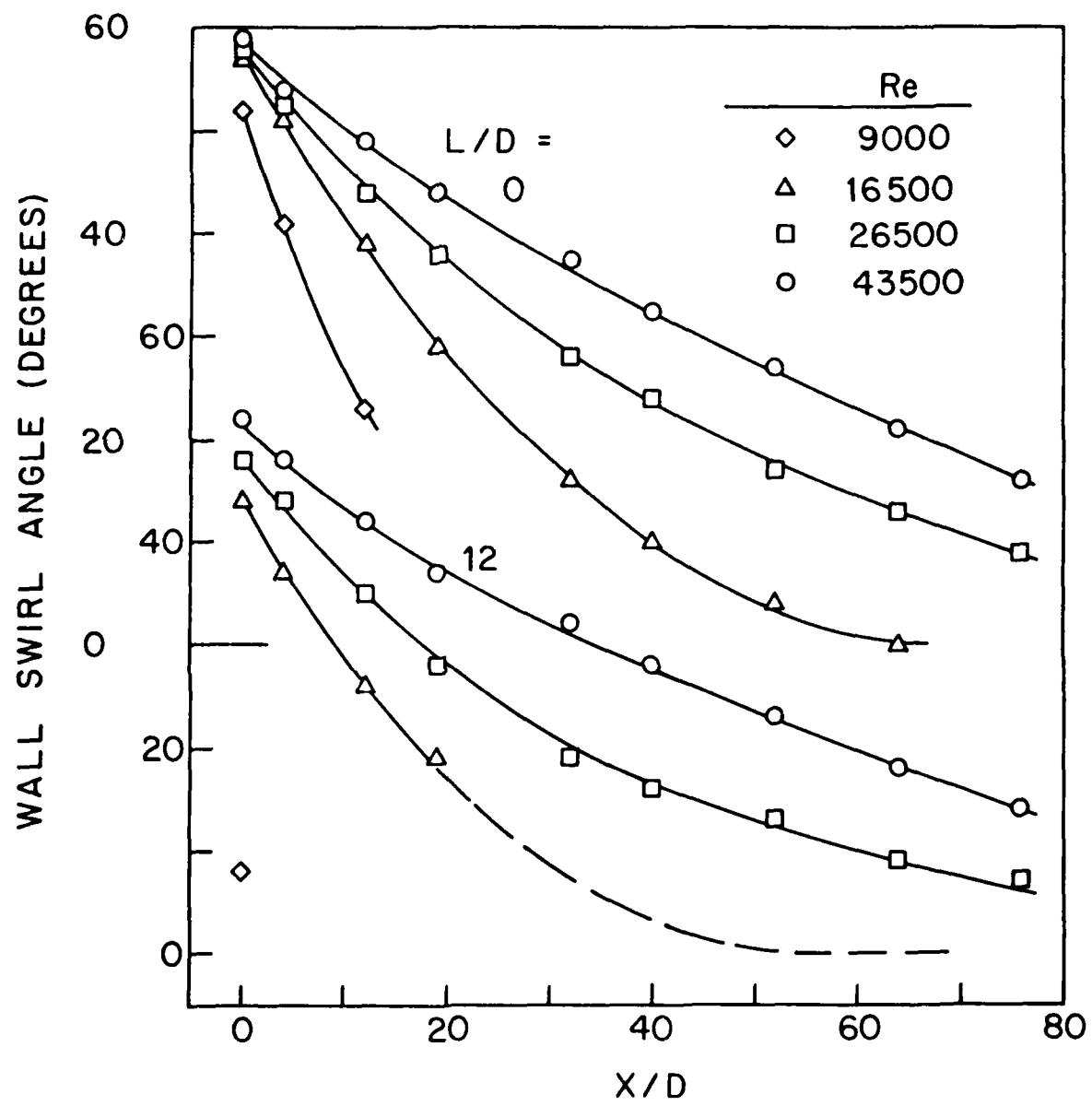
Fig. 4
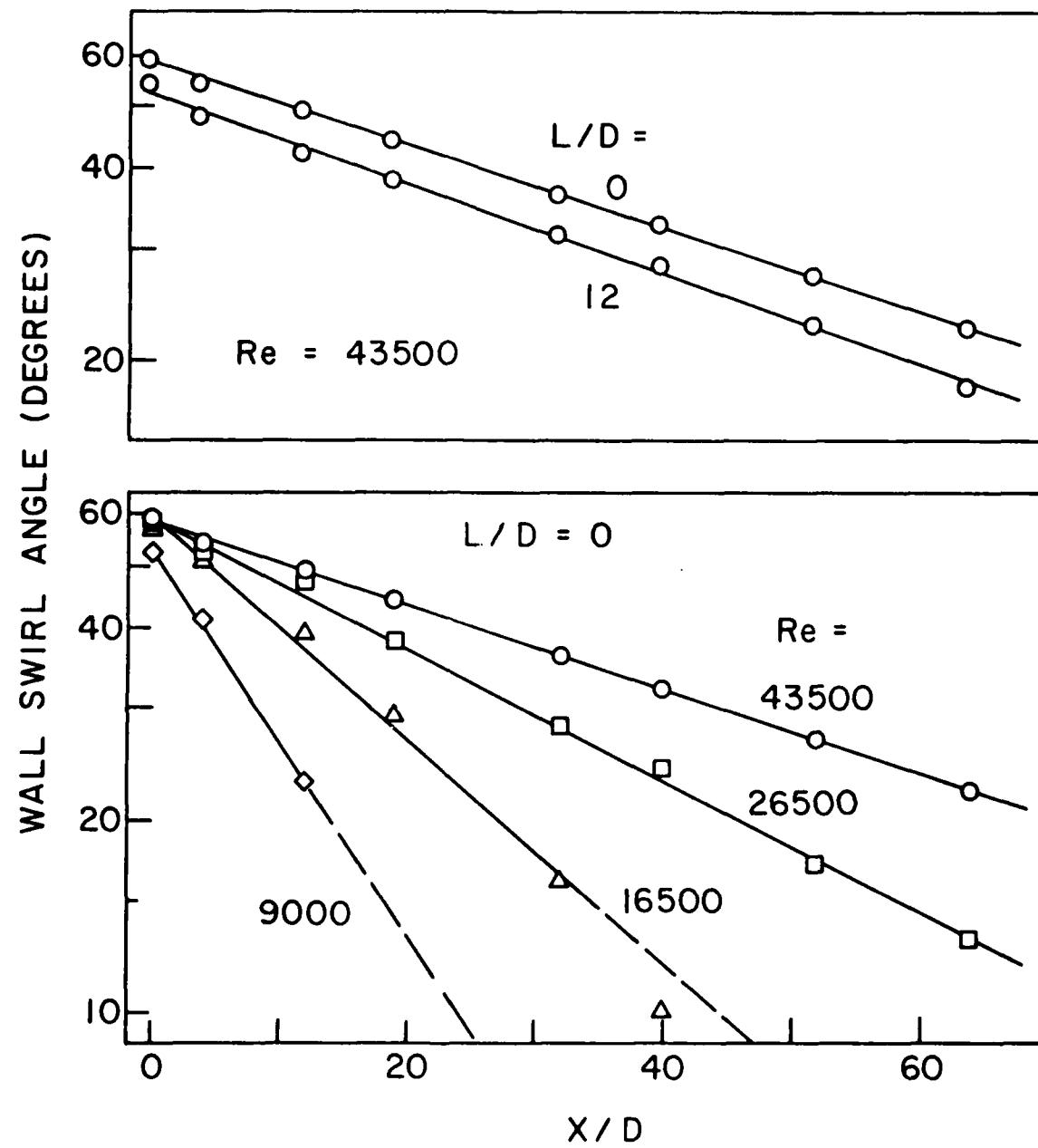
Fig. 5
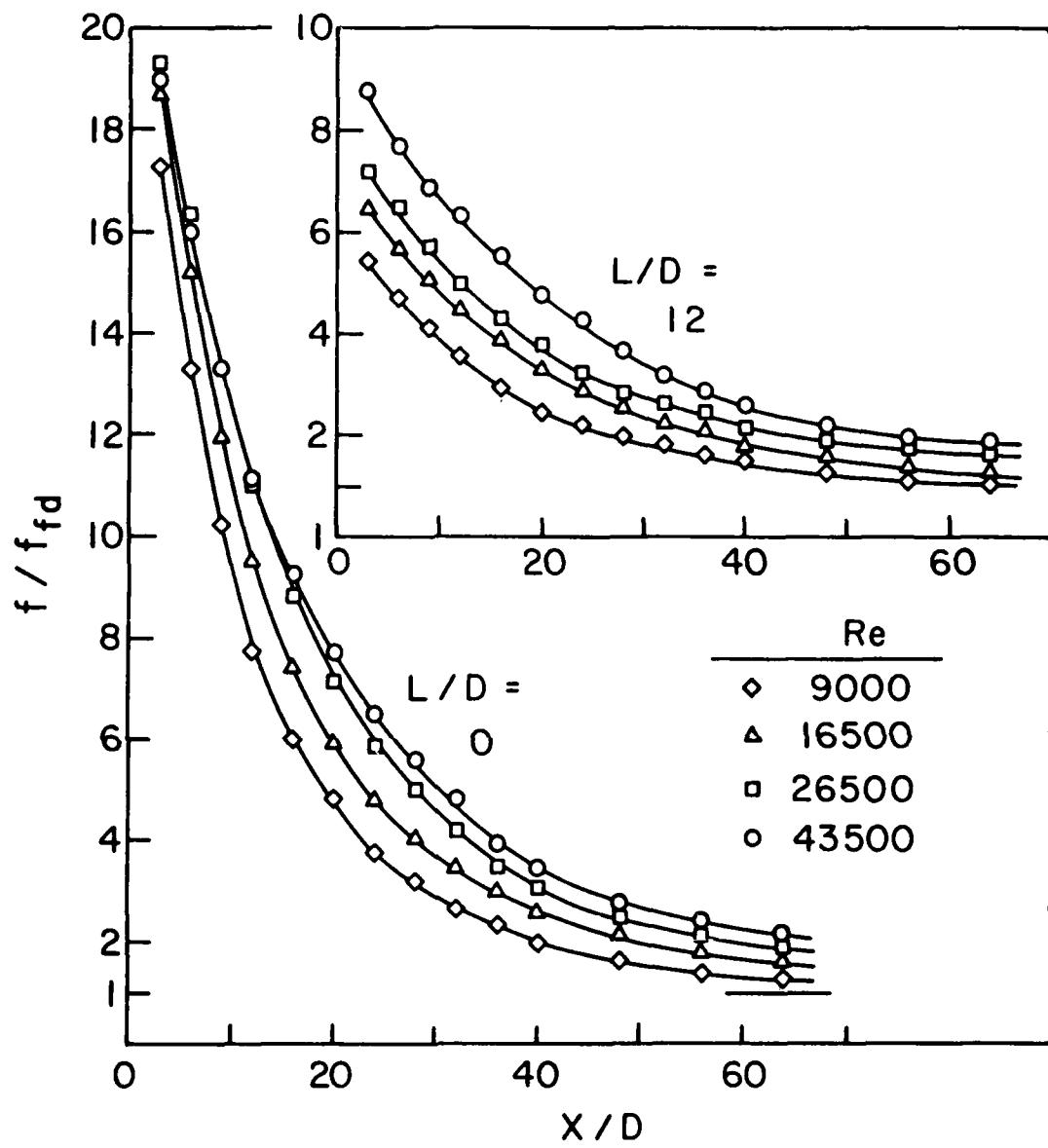
Fig. 6
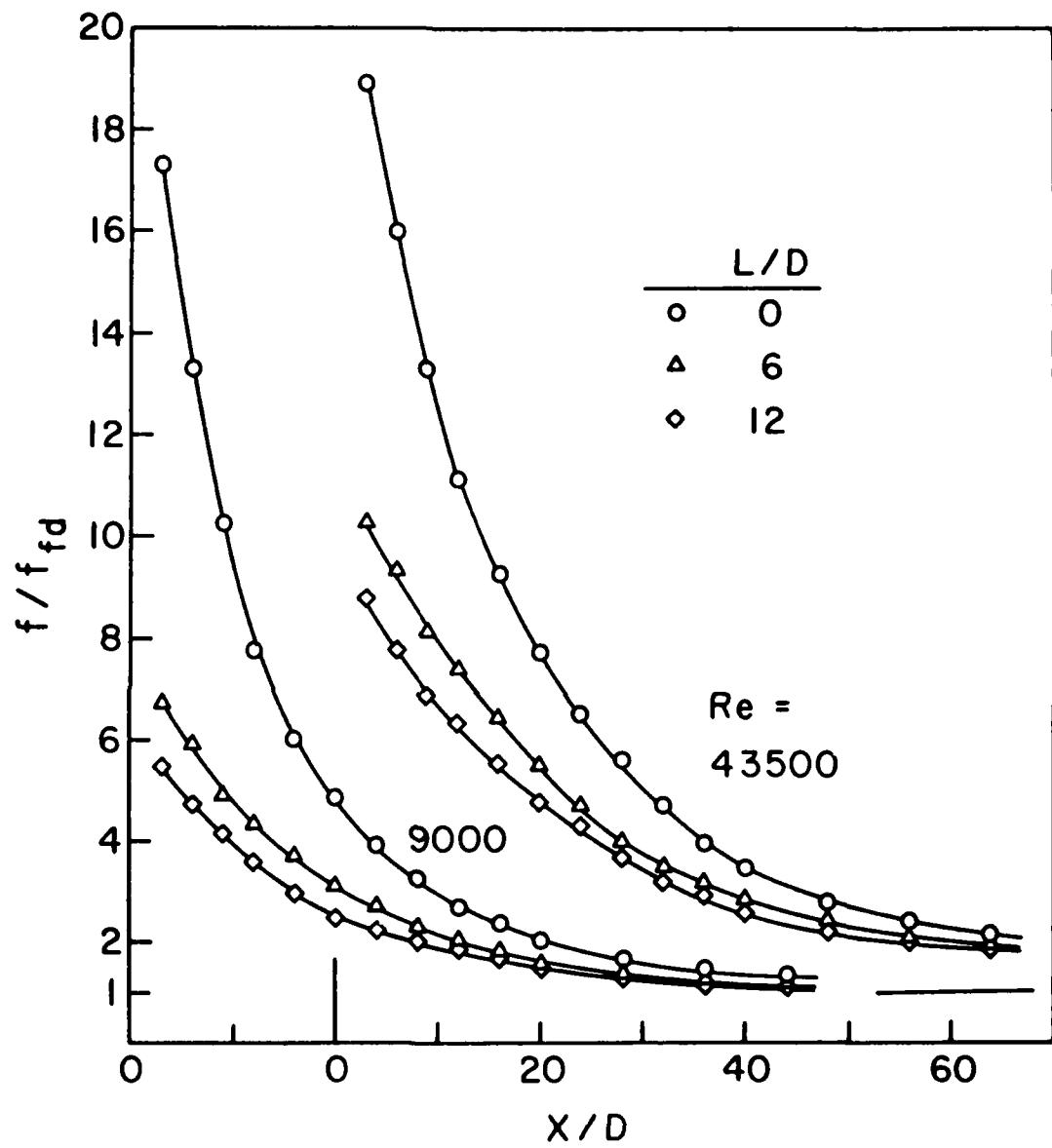
Fig. 7
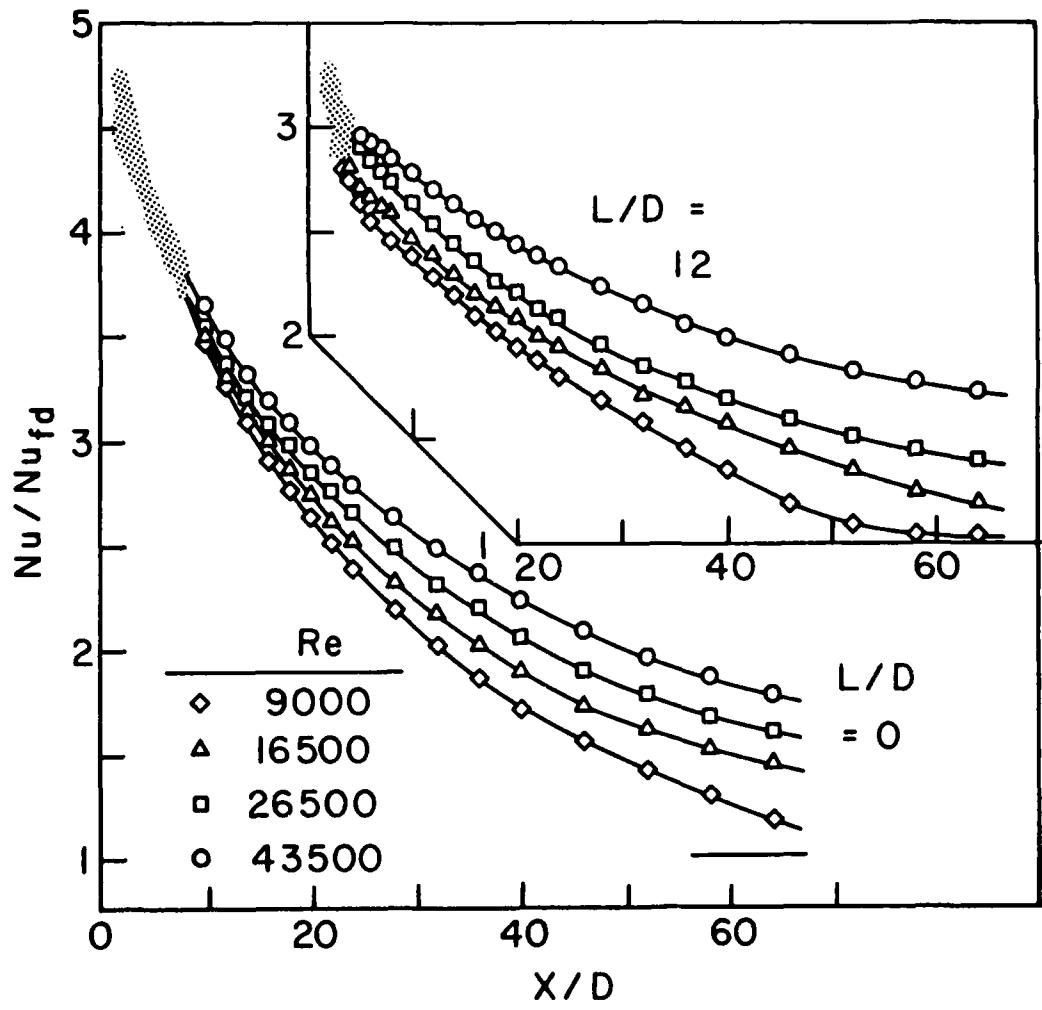
Fig. 8
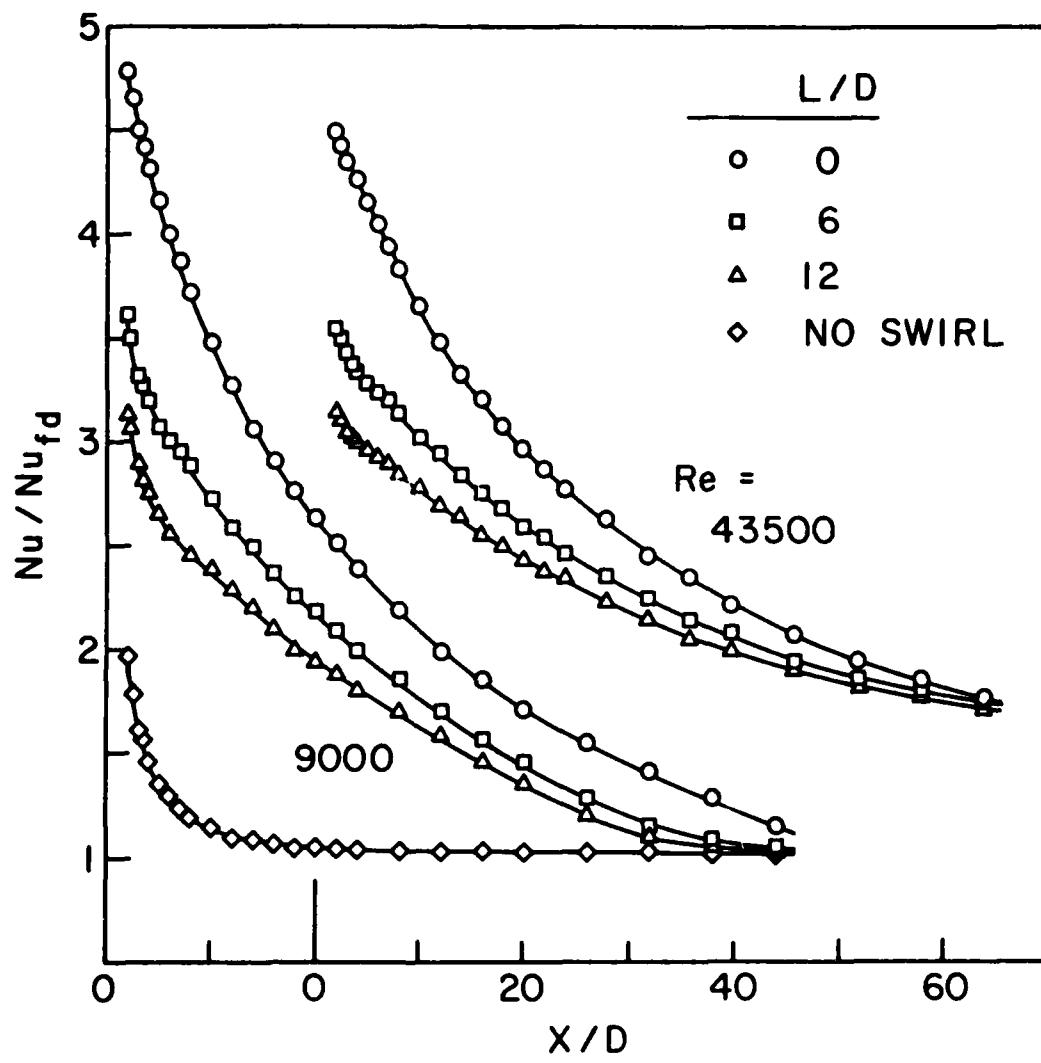
Fig. 9

# SYMMETRIC VS. ASYMMETRIC PERIODIC DISTURBANCES

# AT THE WALLS OF A HEATED FLOW PASSAGE

## ABSTRACT

Measurements were made of local and fully developed turbulent heat transfer coefficients for a flat rectangular duct having streamwise-periodic, two-dimensional disturbances symmetrically positioned at both principal walls. Friction factors were also determined. The local transfer coefficient distributions revealed the rapid attainment of the periodic fully developed regime. The fully developed transfer coefficients exceeded (typically by forty percent) those for an otherwise identical duct having periodic disturbances at only one of the principal walls (asymmetric case). The symmetric disturbances also yielded significantly increased transfer coefficients (up to a factor of three) compared with a corresponding disturbance-free duct. Large disturbance-related increases in the friction factor were also sustained. An analysis based on fixed duct dimensions and fixed pumping power was made to assess the relative performance of the symmetrically and asymmetrically disturbed ducts and the disturbance-free duct. For a wide range of conditions, the symmetrically disturbed duct yielded the highest fully developed transfer coefficients. Compact correlations in terms of roughness parameters were developed for both the fully developed heat transfer coefficients and friction factors.

# NOMENCLATURE

$A_{cyc}$    mass transfer area, pW

AR    aspect ratio, W/H

$D_h$    hydraulic diameter

$\mathcal{D}$    diffusion coefficient

e    disturbance height ( = rod diameter)

$e^+$    roughness Reynolds number, equation (12)

f    fully developed friction factor

H    duct height

$H_e^+$    heat (mass) transfer function, equation (13)

$h_{fd}$    cycle-average fully developed heat transfer coefficient

$h_{fd}^*$    fully developed heat transfer coefficient for disturbance-free duct

K(X)    local mass transfer coefficient

$\overline{K}_{cyc}$    cycle-average fully developed mass transfer coefficient

$K_{fd}$    alternate designation for $\overline{K}_{cyc}$

$K_{fd}^*$    fully developed mass transfer coefficient for disturbance-free duct

$\dot{M}_{cyc}$    per-cycle fully developed mass transfer rate

$\dot{m}(X)$    local rate of mass transfer per unit area

P    pressure

PP    pumping power

p    center-to-center pitch of disturbance rods

$R^+$    modified roughness function, equation (11)

$R_e^+$    roughness function, equation (10)

Re    Reynolds number

$Re^*$    Reynolds number for disturbance-free duct

Sc    Schmidt number

Sh(X)    local Sherwood number

$\overline{Sh}_{cyc}$    cycle-average fully developed Sherwood number

St     Stanton number

V     mean velocity

W     duct width

$\dot{w}$     mass flowrate through duct

X     axial coordinate

Greek symbols

$\mu$     viscosity

$\nu$     kinematic viscosity

$\rho$     air density

$\rho_{nb}$     bulk density of naphthalene vapor

$\rho_{nw}$     density of naphthalene vapor at wall

$\Delta\rho_{cyc}$     per-cycle difference between $\rho_{nw}$ and $\rho_{nb}$

Superscript

*     disturbance-free duct

INTRODUCTION

The research described here is the second and concluding part of an in-depth, two-part experimental study of streamwise-periodically-disturbed turbulent heat transfer and pressure drop in a flat rectangular duct. The work was motivated by the search for enhancement techniques for heat transfer in the flow passages of heat exchange devices.

In the first part of the study [1], two-dimensional disturbance elements were periodically deployed adjacent to one of the principal walls of the duct. Each disturbance element was a small-diameter circular rod which was oriented transverse to the flow direction and which spanned the full width of the duct. The other principal wall of the duct was smooth (i.e., free of disturbance elements). Two geometrical parameters were varied during the course of the experiments, including: (1) the ratio of the streamwise pitch of the disturbance elements to the element height (i.e., diameter) and (2) the ratio of the disturbance element height to the duct height. For each configuration, the duct Reynolds number was varied between 10,000 and 45,000. In addition, two thermal boundary conditions were investigated: (1) the same uniform temperature at both principal walls and (2) uniform temperature at the wall adjacent to the disturbance elements; no heat transfer at the smooth principal wall.

Local heat transfer coefficients were measured at 160 axial stations, and this information was employed to determine cycle-averaged, fully developed heat transfer coefficients. The fully developed coefficients at the disturbance-adjacent wall were enhanced by as much as 140 percent compared with those for the corresponding smooth-walled duct. For the average coefficient encompassing both principal walls (both at uniform wall temperature), enhancements as large as 90 percent were encountered. The measured fully developed friction factors were several times larger than those for the smooth duct. Both the fully developed heat transfer coefficients and friction factors were successfully

correlated using roughness parameters.

The research reported here was undertaken to fulfill two objectives. The first was to extend the previous work [1] to the case in which there are disturbance rods positioned adjacent to both of the principal walls of the duct. For this case, the same geometrical and flow parameters will be employed and varied as in [1] for the one-sided disturbed duct. For these experiments, both of the principal walls are maintained at the same uniform temperature. The experiments yield local heat transfer coefficients, cycle-average fully developed heat transfer coefficients, and fully developed friction factors. Correlations of the fully developed results will be developed in terms of roughness parameters.

The second objective of the work is to quantify the performance of both the one-sided and two-sided disturbed ducts with respect to a corresponding smooth-walled duct. In order to take account of both the heat transfer and pressure drop characteristics of the various ducts, the comparison will be made for the condition of equal pumping power. The outcome of the comparison will be a rank ordering of the one-sided disturbed duct, the two-sided disturbed duct, and the smooth-walled duct based on which yields the highest heat transfer coefficient for a given pumping power.

The smooth-walled heat transfer and pressure drop data needed for the aforementioned performance appraisal were measured in [1] and were found to be in excellent agreement with available literature information. The literature survey set forth in [1] for duct flows with wall-adjacent periodic disturbances is also applicable for the present investigation and needs no elaboration.

## THE EXPERIMENTS

A schematic side view of the flat rectangular duct used in the experiments is presented in Fig. 1. The diagram shows the two principal walls of the duct and the circular-rod disturbance elements deployed adjacent to each of the walls. The two sets of rods are positioned at common axial stations, with the axial

separation distance between the centers of successive rods denoted by p (pitch). Since p is uniform along the duct, the rods provide streamwise-periodic, two-dimensional disturbances.

In addition to the pitch p, the other two lengths which characterize the flow passage geometry are indicated in the figure--the height H of the duct and the height e of the disturbance elements (equal to the rod diameter). In non-dimensional terms, the passage geometry may be characterized by two dimension ratios involving the quantities p, H, and e. The ratios to be employed here are p/e and e/H, and Table 1 lists the investigated numerical values of these quanti-ties. As seen there, for each of two disturbance height/duct height ratios, three values of the pitch-height ratio of the disturbance elements were employed. These parameter values were obtained by using ducts of two different heights (0.636 and 1.275 cm) and disturbance elements with three different pitches (0.952, 1.905, and 3.811 cm), while maintaining the disturbance height fixed (e = 1.051 mm). All told, then, six different configurations were investigated.

Another dimension ratio of potential relevance is the aspect ratio AR = W/H (W = width of duct) of the duct cross section. However, the values of AR employed in the experiments, 6.4 and 12.8, are believed to be sufficiently large to elimi-nate it as a significant parameter. By incorporating the aspect ratio into the conventional definition of the duct hydraulic diameter $D_h$, it readily follows that $e/D_h = \frac{1}{2}(e/H)(1 + 1/AR)$, yielding an alternative measure of the relative height of the disturbance elements.

The disturbance rods spanned the entire width W of the duct. To hold the rods in place, holes had been drilled along the upper and lower edges of the duct side walls, and the rod ends were seated in these holes. The rods were cut from lengths of 1.051-mm diameter drill-rod stock, selected for straightness and uniformity of diameter.

Figure 1 also shows the inlet configuration of the duct. As seen there,

the inlet is sharp edged. In addition, the upstream end of the duct is set into

a large baffle plate. This arrangement simulates the situation in which the

duct inlet is built into the downstream wall of a large plenum chamber. At the

downstream end of the duct (not shown), there is a rectangular-to-circular transi-

tion section which, in turn, is connected to an air handling system consisting

of a flowmeter, a control valve, and a blower.

The system is operated in the suction mode, with air from the temperature-

controlled laboratory room being drawn into the duct inlet. The blower is located

in an adjacent room, and the blower discharge is vented outside the building.

The naphthalene sublimation technique was used in the execution of the ex-

periments because it affords several advantages compared with direct heat transfer

measurements. By employing the well-established analogy between heat and mass

transfer, the mass transfer coefficients and Sherwood numbers determined here can

be transformed to heat transfer coefficients and Nusselt numbers.

The surface of each principal wall was of naphthalene, freshly cast for each

data run. The surface finish of the naphthalene was comparable to that of the

highly polished stainless steel plate against which the casting was made. The

side walls of the duct were metallic (aluminum) and, therefore, did not partici-

pate in the mass transfer process.

At the principal walls, the mass transfer boundary condition was that the

density of the naphthalene vapor is uniform. By the analogy, this corresponds

to uniform wall temperature in the corresponding heat transfer problem. The

mass-transfer inactive side walls correspond to adiabatic surfaces.

The naphthalene vapor density in equilibrium with a solid naphthalene surface

depends on the surface temperature. Since the vapor density at the principal

walls of the duct is needed in the data reduction, the surface temperature was

measured by calibrated thermocouples that were embedded in the solid during the

casting process. Two thermocouples were installed in each wall. Deviations

among the thermocouple readings were never greater than 0.05 - 0.1$^o$C.

The local mass transfer coefficients were deduced from measurements of the surface contours of the principal walls. Such measurements were performed both before and after each data run. By differencing the before and after measurements, the amount of mass sublimed at each measurement station was determined. At each principal wall, the surface contour was measured in a 160-point axial traverse along each of three parallel lines, one of which was situated midway between the duct side walls while the others were respectively situated to either side of the midline, halfway between it and the side wall. The measurement system (depth sensor and electronics) had a resolving power of 10$^{-5}$ inches. Further details of the surface contour measurements are given in [1].

Pressure drop experiments were performed using an auxiliary apparatus in which the naphthalene-surfaced principal walls were replaced by metallic walls. The axial deployment of the pressure taps was tailored to take account of the streamwise periodic nature of the flow. In particular, in the periodic fully developed regime, the pressure drop per cycle (i.e., in an axial length p) is a constant. Consequently, pressure taps with an axial spacing p (or an integer multiple of p) will yield a linear pressure distribution in the fully developed regime. This pressure tap pattern was adopted in the experiments. Pressure drops were measured with a capacitance-type, solid-state pressure meter capable of resolving 10$^{-3}$ or 10$^{-4}$ Torr, depending on the pressure level.

## DATA REDUCTION

Two types of mass transfer coefficients (and corresponding Sherwood numbers) were evaluated from the experimental data. One of these is the local transfer coefficient at any axial station X. The other is the cycle-average transfer coefficient for the periodic fully developed regime.

For the evaluation of the local coefficient, the first step is to average out any slight differences in the sublimation rates at a given $X$ among the

three parallel lines along which the contour measurements were made at each principal wall. Furthermore, the two principal walls yielded virtually the same local mass transfer rates, and any small differences were averaged out. Then, let $\dot{m}(X)$ denote the local rate of mass transfer per unit area at X. Also, let $\rho_{nw}$ denote the napththalene vapor density at the principal walls and $\rho_{nb}(X)$ the bulk naphthalene vapor density at X. With these, the local mass transfer coefficient K(X) is

$$K(X) = \dot{m}(X)/[\rho_{nw} - \rho_{nb}(X)] \tag{1}$$

Among the quantities appearing in equation (1), $\dot{m}(X)$ is determined directly from the differences between the surface contours measured before and after the data run (equation (2) of [1]). The density $\rho_{nw}$ is evaluated from the vapor pressure/temperature relation for naphthalene in conjunction with the perfect gas law (note that $\rho_{nw}$ is independent of X). For $\rho_{nb}(X)$, the naphthalene subliming from the walls between $X = 0$ and $X \approx X$ is balanced by the increase in the naphthalene vapor content of the air between those stations (equation (5) of [1]; note also that $\rho_{nb} = 0$ at $X = 0$).

Attention will next be turned to the cycle-average fully developed mass transfer coefficient. As a first step, the per-cycle, fully developed mass transfer rate $\dot{M}_{cyc}$ is evaluated from

$$\dot{M}_{cyc} = \int_{X}^{x+p} \dot{m}(X)WdX \tag{2}$$

where X and $(X + p)$ are situated in the fully developed regime. Since $\dot{m}(X)$ is already averaged for the two principal walls, the individual walls need not be considered separately. The mass transfer surface area corresponding to $\dot{M}_{cyc}$ is $A_{cyc} = pW$.

The per-cycle mass transfer is driven by the mean per-cycle difference between $\rho_{nw}$ and $\rho_{nb}$. This difference, to be denoted by $\Delta\rho_{cyc}$, involves $\rho_{nb}(X)$ $(X + p)$, as well as $\rho_{nw}$. These quantities were individually evaluated

as described in the foregoing. For $\Delta\rho_{cyc}$, calculations were made for three different models: (1) log mean, (2) arithmetic mean, and (3) integrated mean of $[\rho_{nw} - \rho_{nb}(X)]$. The mass transfer coefficients based on these calculation models were identical within plotting accuracy.

In terms of the quantities defined in the preceding paragraphs

$$\overline{K}_{cyc} = \dot{M}_{cyc}/A_{cyc}\Delta\rho_{cyc} \tag{3}$$

The dimensionless counterparts of $K(X)$ and $\overline{K}_{cyc}$ are the Sherwood numbers

$$Sh(X) = K(X)D_h/\mathcal{D}, \quad \overline{Sh}_{cyc} = \overline{K}_{cyc}D_h/\mathcal{D} \tag{4}$$

in which $D_h$ is the conventional hydraulic diameter $[2HW/(H + W)]$, and $\mathcal{D}$ is the naphthalene–air diffusion coefficient. The latter is eliminated by using the Schmidt number Sc, which gives

$$1/\mathcal{D} = (1/\nu)Sc \tag{5}$$

and Sc = 2.5 for the naphthalene–air system.

The pressure drop and friction factor will now be considered. As noted earlier, the pressure taps were positioned to measure the per-cycle pressure drop in the fully developed regime, which is the same from cycle to cycle. From the resulting linear pressure distribution, the gradient dP/dX was determined and used in the evaluation of the fully developed friction factor

$$f = (-dP/dX)D_h/\tfrac{1}{2}\rho V^2 \tag{6}$$

where $\rho V^2 = (\dot{w}/HW)^2/\rho$, in which $\dot{w}$ is the mass flowrate and $\rho$ is the density in the fully developed regime.

The Reynolds number was employed as a dimensionless representation of the mass flow

$$Re = \rho VD_h/\mu = 2\dot{w}/\mu(H + W) \tag{7}$$

Re was evaluated from the rightmost term of equation (7).

## DISTRIBUTIONS OF THE LOCAL MASS TRANSFER COEFFICIENT

Each data run yielded the axial distribution of the local Sherwood number Sh(X). A sampling of this information will now be presented. This presentation will complement the Sh(X) distributions at the disturbance-adjacent wall for a one-sided disturbed duct as displayed in Figs. 2 - 6 of [1].

As was noted earlier, the mass transfer results for the two principal walls were virtually identical, and whatever small differences did exist were averaged out. The Sh(X) distributions now to be presented are, therefore, representative of both walls.

Figure 2 displays the response of the local Sherwood number distribution to changes in Reynolds number. In the figure, Sh(X) is plotted as a function of $X/D_h$ for Re = 10,700, 21,400, and 35,000. These results correspond to fixed values of the geometric parameters e/H and p/e, respectively equal to 0.164 and 18.3. Along the abscissa of each graph in Fig. 2 are black circles which indicate the axial positions of the disturbance rods.

Before considering the effect of Reynolds number, it is appropriate to comment on the general character of the Sh(X) distributions. The portion of the distribution upstream of the first rod reflects the separation of the flow at the sharp-edged inlet of the duct. In particular, the first peak corresponds to the reattachment of the separated flow. The remainder of the Sh(X) distribution is shaped and controlled by the presence of the periodic disturbances. It is seen that Sh(X) takes on a periodic pattern almost immediately, and the virtual absence of an entrance region is noteworthy.

The flow separates each time it encounters a disturbance rod. Reattachment occurs in the inter-rod space, and each reattachment corresponds to a peak in the Sh(X) distribution. Subsequent to reattachment, the flow begins to redevelop, causing Sh(X) to drop off. The dropoff is arrested as the flow encounters the next disturbance rod, and Sh(X) increases as the separated flow approaches

reattachment.

At axial stations in the neighborhood of the disturbance rods, there are occasional data points which do not fall on the mainline Sh(X) distribution. These points, which, for the most part, are high, are not scatter. Rather, they reflect the presence of intense, compact vortices situated immediately upstream and downstream of the disturbance rod.

With regard to the Reynolds number, its main effect is to change the level of the Sh(X) distribution. However, the shape of the distribution is virtually unaffected. In particular, the location at which the maximum occurs (i.e., the point of flow reattachment in the inter-rod space) is unchanged in the investigated Reynolds number range. There is, however, a tendency for the maximum to become somewhat more peaked with increasing Reynolds number. This peaking tendency is associated with a more rapid dropoff of Sh(X) downstream of the maximum.

The next issue to be considered is the effect of the pitch p of the disturbance rods on the Sh(X) distribution, and Fig. 3 has been prepared for this purpose. Results are given for p/e = 9.15, 18.3, and 36.6 for fixed values of Re = 12,700 and e/H = 0.082. In considering this figure, it is helpful to take note of the black circles along the abscissa of each graph which serve to depict the positions of the disturbance rods.

Inspection of Fig. 3 shows that the main effect of a change in pitch is to alter the extent of the flow redevelopment which follows reattachment. With increasing pitch (i.e., larger inter-rod space), the amount of redevelopment increases. This is especially evident in the results for p/e = 36.6, where the flattening of the Sh(X) distribution in the aft portion of the inter-rod space testifies to the considerable amount of redevelopment that has occurred. Thus, the velocity distribution in the flow approaching the next disturbance rod (which is directly related to the degree of redevelopment of the flow) changes as the pitch changes. Despite this, the distance downstream of the rod at which

reattachment occurs is virtually unaffected by changes in pitch.

The final aspect of the Sh(X) distributions to be considered is the effect of the relative heights of the disturbance rods and the duct. Figure 4 shows results for e/H = 0.082 and 0.164 for Re $\simeq$ 20,000 and p/e = 18.3. Note that the $X/D_h$ scales for the two graphs are different because of the different $D_h$ values for the two cases. The shapes of the two Sh(X) distributions are the same. Indeed, if not for the different abscissa scales, they would be very nearly coincident, aside from the non-mainline points, which tend to be irregular. Also, the distribution for e/H = 0.082 appears to bottom-out at slightly lower values than does the e/H = 0.164 distribution.

## FULLY DEVELOPED MASS TRANSFER AND FRICTION RESULTS

As noted earlier, the per-cycle mass transfer coefficient and Sherwood number are constant in the periodic fully developed regime. In addition, the constancy of the per-cycle pressure drop enables a fully developed friction factor to be defined and evaluated. The fully developed regime is of particular importance in periodically disturbed flows because the entrance length is very short (Figs. 2 - 4).

<u>Sherwood numbers</u>. The per-cycle fully developed Sherwood numbers are plotted in Fig. 5 as a function of the Reynolds number. The figure conveys results for all six of the investigated configurations. In order to avoid overlap, the results for e/H = 0.164 are plotted as $2\overline{Sh}_{cyc}$, while those for e/H = 0.082 are plotted directly as $\overline{Sh}_{cyc}$. Within each e/H grouping, the p/e parameter is assigned values of 9.15, 18.3, and 36.6.

The straight lines which pass through the data are least-squares fits of the form

$$\overline{Sh}_{cyc} = CRe^n \tag{8}$$

where the constants C and n are listed in Table 1. The exponents n (slopes of the lines in Fig. 5) are clustered in the range 0.59 - 0.65. The n values are

very slightly higher for e/H = 0.082 (cases 1 - 3) than for e/H = 0.164 (cases 4 - 6), but there is no systematic variation with p/e. There is virtually no scatter of the data points relative to the least-squares lines.

The figure shows that for fixed values of the other parameters, more closely spaced disturbance elements (smaller p/e) give rise to higher Sherwood numbers. It may also be observed that the duct with the lesser height (e/H = 0.164) is more responsive to changes in p/e than is the duct with the greater height (e/H = 0.082).

After taking account of the two-fold scaling, it can be verified that the p/e = 36.6 curves for the two e/H values are virtually coincident and that the p/e = 18.3 curves deviate from each other by only a few percent. For p/e = 9.15, the deviations between the two curves is in the ten percent range. Therefore, for fixed values of Re and p/e, the Sherwood number is not very sensitive to e/H. However, it does not necessarily follow that the mass transfer coefficient is similarly insensitive to e/H. This is because an H-related difference in e/H may give rise to different values of $D_h$, which have to be used when the mass transfer coefficient is extracted from the Sherwood number.

The per-cycle fully developed Sherwood numbers just presented for the two-sided disturbed duct will now be compared with those for the one-sided disturbed duct that was investigated in [1]. The comparison is displayed in Figs. 6 and 7, which respectively correspond to fixed values of e/H equal to 0.082 and 0.164. The lines appearing in these figures are least-squares fits of the experimental data (the actual data are displayed in Fig. 5 and in Figs. 8 and 9 of [1]).

In each figure, the results are grouped according to p/e. In each grouping, there are three lines. One of these is for the two-sided disturbed duct (two rodded walls), while the others are for the one-sided disturbed duct (one rodded/ one smooth). Note that for the latter duct, both the rodded and smooth walls participate in the mass transfer process. For this duct, Sherwood number results

are shown separately for the rodded wall and for the average of the smooth and rodded walls.

From an overall inspection of Figs. 6 and 7, it is seen that the per-cycle fully developed Sherwood numbers for a two-sided disturbed duct always exceed those for a one-sided disturbed duct. For concreteness, the smooth wall/rodded wall average for the one-sided case will be compared with the two-sided case. Such a comparison shows that relative to the one-sided disturbances, the two-sided disturbances give rise to Sherwood number enhancements in the 25 - 60 percent range, with 40 percent representing a typical enhancement.

In general, there is a tendency toward larger double-disturbance-related enhancements at lower Reynolds numbers, except at the smallest pitch ($p/e$ = 9.15) where the enhancement is virtually independent of Reynolds number. Also, among the various disturbance pitches, the smallest enhancement occurs for the largest pitch. Globally speaking, the enhancements are not strongly dependent on $e/H$.

Figures 5-7 have focused on the Sherwood numbers for ducts with periodic disturbances. To provide perspective for these results, the fully developed Sherwood numbers for corresponding disturbance-free ducts have been measured [1]. For $Re$ = 10, 20, 30, and 40 x $10^3$, the Sh values are 56.8, 96.4, 134, and 169. When these values are compared with those of Figs. 5 - 7, it is seen that the presence of the disturbance rods yields up to a three-fold increase in the Sherwood number at $Re$ = 10,000 and up to a 2.4-fold increase at $Re$ = 40,000. These impressive enhancements are accompanied by large increases in pressure drop, as will be demonstrated shortly. The trade-off between the higher Sherwood numbers and higher friction factors will be assessed later in the paper.

Friction factors. The fully developed friction factors are plotted in Fig. 8 as a function of the Reynolds number. The presentation includes both the one-sided disturbed duct and the two-sided disturbed duct. Data points are shown only for the latter since the data for the former are displayed in Fig. 7 of [1].

The straight lines appearing in the figure are least-squares correlations of the form

$$f = C_1 Re^{-m} \tag{9}$$

The constants $C_1$ and m for the two-sided disturbed duct are listed in Table 2, while those for the one-sided disturbed duct are given in [1] in the text following equation (16).

For the corresponding ducts without disturbances, the measured friction factors [1] are 0.0343, 0.0283, 0.0256, and 0.0239, respectively for Re = 10, 20, 30, and 40 x $10^3$.

From Fig. 8, it is seen that, as expected, the presence of disturbance rods at both principal walls takes a greater toll in pressure drop than do rods at one principal wall. The increase is, however, much greater for ducts of smaller height, as is seen by comparing the results for e/H = 0.164 with those for e/H = 0.082. This finding is physically plausible and is related to the appreciable blockage of the flow cross section which occurs when disturbance elements are situated at both principal walls in a duct of relatively low height. In the present experiments, for the e/H = 0.164 configuration, the cross-sectional blockage was 32.8 percent at the axial stations at which the rods were situated. The greater pressure drop for the lower-height, two-sided disturbed duct will figure prominently in the performance evaluations to be presented later.

Another interesting point, evident both in Fig. 8 and in Table 2 for the two-sided disturbed duct, is that the f,Re curves for e/H = 0.164 are flatter than those for e/H = 0.082. It is well established that the flatter the f,Re distribution, the more significant are inertial losses relative to friction losses. Since greater cross-sectional blockage accentuates inertial losses, the flatter f,Re distributions for the e/H = 0.164 case are physically reasonable. As expected, the friction factor is larger for more closely spaced disturbances (i.e., for smaller p/e).

By comparing the f values of Fig. 8 with those indicated earlier for

disturbance-free ducts, it is seen that the disturbance elements give rise to very large increases in pressure drop. Owing to the large parameter-dependent spread of the data, the extent of the increase is also highly parameter-dependent, but factors of 5 - 10 fall within the observed range.

Correlations based on roughness parameters. A very compact presentation of the fully developed mass transfer and pressure drop results can be achieved in terms of the so-called roughness parameters. These parameters have already been used in [1] to correlate the results for one-sided disturbed ducts, and they will be employed here (with selective modifications) for two-sided disturbed ducts.

The first step is to write the roughness function $R_e^+$ as set forth in [1]

$$R_e^+ = (8/f)^{\frac{1}{2}} + 2.5\ell n(2e/D_h) + 4.23 \tag{10}$$

Next, a modified roughness function $R^+$ appropriate to the present two-sided disturbed ducts is introduced

$$R^+ = [(e/D_h)/(p/e)]^{0.4}R_e^+ \tag{11}$$

The Reynolds number is incorporated in another roughness parameter, $e^+$

$$e^+ = (f/8)^{\frac{1}{2}}(e/D_h)Re \tag{12}$$

The friction factor, Reynolds number data for all of the two-sided disturbed cases were recast into the $R^+, e^+$ parameters and plotted in Fig. 9. The correlation of the data is seen to be very good, especially when account is taken of the large spread of the same data when presented in terms of f and Re (see Fig. 8). Least-squares, straight-line correlations are shown in Fig. 9, along with the correlating equations. The breakpoint between the lines is at $e^+ = 300$.

For the correlation of the Sherwood number results, a function $H_e^+$ is defined as

$$H_e^+ = [(f/8St) - 1]/(f/8)^{\frac{1}{2}} + R_e^+ \tag{13}$$

where

$$St = \overline{Sh}_{cyc}/ReSc \tag{14}$$

The $\overline{Sh}_{cyc}$,Re data were rephrased in terms of $H_e^+$ and $e^+$ and plotted in Fig. 10.

The data are well correlated by these parameters, and a least-squares correlating equation is presented in the figure.

The highly satisfactory correlations in evidence in Figs. 9 and 10 encourage their use for interpolation between the present parameter values and for moderate extrapolation.

## PERFORMANCE ASSESSMENTS

The fact that both the mass (heat) transfer coefficients and friction factors are increased by the presence of the periodic disturbance elements requires that further analysis be performed to assess the net effect of the disturbances. Such an assessment is usually made by comparing an enhanced configuration with a related baseline configuration. The comparison is carried out under a set of constraints which depend on the specifics of each application.

Here, the assessment methodology is illustrated by considering a flat rectangular duct of fixed cross-sectional and length dimensions. Three versions of the duct are to be compared: (1) no disturbance elements, (2) disturbance elements deployed along one principal wall, and (3) disturbance elements deployed along both principal walls. Among these, the disturbance-free duct will be regarded as the baseline case and is designated by an asterisk. The objective of the assessment is to determine which configuration has the highest fully developed mass (heat) transfer coefficient under the constraint that the pumping power be equal for all three configurations.

The pumping power PP is given by

$$PP = (\dot{w}/\rho)\Delta P \tag{15}$$

and the equal pumping power constraint can be expressed as

$$PP = (PP)^* \tag{16}$$

where the left-hand side refers to either of the enhanced (i.e., periodically disturbed) configurations while the right side corresponds to the baseline case. For fixed duct dimensions and equal thermophysical properties, equation (16)

becomes

$$fRe^3 = (fRe^3)^*$$  (17)

Since the friction factor has been experimentally determined as a function of the Reynolds number for both the baseline and the enhanced configurations, equation (17) is a relation between Re and Re$^*$.

The numerical results obtained from the solution of equation (17) are presented in Fig. 11, where Re for the periodically disturbed configurations is plotted as a function of Re$^*$ for the disturbance-free configuration. In each of the two graphs which make up Fig. 11, results are presented for six disturbed-duct cases. The e/H = 0.082 graph pertains to cases 1 - 3 of Table 1, with the suffix A denoting the two-sided disturbed duct and the suffix B denoting the one-sided disturbed duct. A similar set of results is conveyed in the e/H = 0.164 graph.

In general, for all cases depicted in Fig. 11, Re < Re$^*$. This finding is physically plausible since the higher pressure drops of the periodically disturbed ducts must be balanced by lower mass throughflows in order to satisfy the equal pumping power constraint. By the same reasoning, it follows that the higher pressure drops of the two-sided disturbed ducts (i.e., the A ducts) will yield lower Reynolds numbers than those for the one-sided disturbed ducts (B ducts). Also, since the pressure drop increases with decreasing pitch, it follows that the smaller the pitch, the lower the Reynolds number, so that the lines for cases 1, 2, and 3 are arranged in ascending order (lowest pitch to highest pitch). Another relevant observation to be made in Fig. 11 is that the Re values for the e/H = 0.164 cases are lower than those for the e/H = 0.082 cases.

With the Re$^*$, Re information of Fig. 11, the corresponding Sherwood numbers can be evaluated and the ratio $(K/K^*)_{fd}$ determined, where the subscript fd denotes fully developed. Note that $K_{fd}$ corresponds to Re and $K^*_{fd}$ corresponds to Re$^*$ (Re and Re$^*$ are related according to Fig. 11). Furthermore, from the analogy between heat and mass transfer, $Nu/Pr^s = Sh/Sc^s$, so that

$$(K/K^*)_{fd} = (h/h^*)_{fd} \tag{18}$$

The $(K/K^*)_{fd}$ results are plotted as a function of $Re^*$ in Fig. 12. As in Fig. 11, there are two graphs, respectively for e/H = 0.082 and 0.164, with six disturbance-duct cases in each graph.

In assessing Fig. 12, the key issue is whether $(K/K^*)_{fd}$ is greater or less than one, with net enhancement corresponding to $(K/K^*)_{fd} > 1$. From the figure, it is seen that all of the e/H = 0.082 cases yield net enhancement. Over most of the Reynolds number range, the enhancement is greater for the two-sided disturbed ducts (A ducts) than for the one-sided disturbed ducts (B ducts), but at the higher end of the range the enhancements are about the same for the two types of ducts. For both ducts, the greatest enhancements occur at the lower Reynolds numbers and drop off as the Reynolds number increases, with a much more rapid dropoff for the two-sided disturbed duct. The maximum value of $(K/K^*)_{fd}$ for the e/H = 0.082 cases is just under 1.5, while the minimum value is about 1.1.

The $(K/K^*)_{fd}$ values for the e/H = 0.164 ducts are lower than those for the e/H = 0.082 ducts. Indeed, at the upper end of the Reynolds number range, $(K/K^*)_{fd} < 1$, indicating net degradation. The largest value of $(K/K^*)_{fd}$ for the e/H = 0.164 ducts is about 1.3.

The superior performance of the ducts with smaller e/H was already foretold by the Reynolds number results of Fig. 11, where it was noted that the equal-pumping-power Reynolds numbers for e/H = 0.164 were lower than those for 0.082.

The outcome of the performance assessment shows that there is merit to the use of periodic disturbances, provided that the geometrical parameters are selected with care.

## CONCLUDING REMARKS

The present experiments have yielded both local and fully developed mass (heat) transfer coefficients for a flat rectangular duct having streamwise-periodic, two-dimensional disturbances at both of the principal walls. Fully developed friction factors were also determined. Three parameters were varied during the course of the investigation, including p/e (pitch-to-height ratio of the disturbance elements), e/H (ratio of disturbance height to duct height), and the Reynolds number Re. The results obtained here serve to complement and complete prior experimental results for a duct having disturbances at only one of the principal walls.

The local Sherwood number distributions revealed the rapid attainment of the periodic fully developed regime, and thereby underscored the importance of the fully developed mass (heat) transfer and friction results, whereby they became the main focus of the work.

The fully developed Sherwood numbers for a two-sided disturbed duct exceeded those for a one-sided disturbed duct, typically by about forty percent. Relative to a disturbance-free duct, the presence of periodic disturbances at both principal walls yielded up to a three-fold increase in the Sherwood number at Re = 10,000 and up to a 2.4-fold increase at Re = 40,000.

The presence of disturbances at both walls also increased the fully developed friction factor relative to that for the one-sided disturbed duct. The increase was substantially greater for a duct of smaller height.

An analysis was carried out to assess the relative performances of the disturbance-free duct, the one-sided disturbed duct, and the two-sided disturbed duct. The analysis was performed for fixed duct dimensions and fixed pumping power and sought the largest values of the fully developed mass (heat) transfer coefficient. Relative to the disturbance-free duct, which served as a baseline case, the presence of periodic disturbances was found to be enhancing over a wide range of

(but not all) conditions. For the most part, greater enhancement was attained with two-sided disturbances than with one-sided disturbances.

Compact correlations, suitable for interpolation and for moderate extrapolation, were developed for both the fully developed Sherwood number and friction factor. The correlation was achieved in terms of the so-called roughness parameters.

## ACKNOWLEDGEMENT

## REFERENCE

1. E. M. Sparrow and W. Q. Tao, Enhanced heat transfer in a flat rectangular duct with streamwise-periodic disturbances at one principal wall, J. Heat Transfer 105, 851-861 (1983).

END

FILMED

DTIC
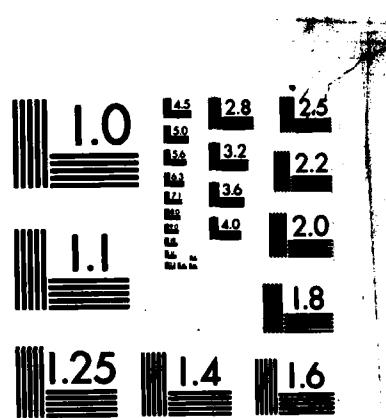
MICROCOPY RESOLUTION TEST CHART
NATIONAL BUREAU OF STANDARDS-1963-A

## Table 1

### Flow Passage Characteristics

| Case | e/H | AR | p/e |
|------|-----|-----|------|
| 1 | 0.082 | 6.4 | 9.15 |
| 2 | | | 18.3 |
| 3 | | | 36.6 |
| 4 | 0.164 | 12.8 | 9.15 |
| 5 | | | 18.3 |
| 6 | | | 36.6 |

## Table 2

### Constants in Equations (8) and (9)

| Case | C | n | $C_1$ | m |
|------|-----|-----|-------|-----|
| 1 | 0.4056 | 0.6428 | 2.034 | 0.2003 |
| 2 | 0.5168 | 0.6126 | 1.588 | 0.2106 |
| 3 | 0.3092 | 0.6468 | 0.981 | 0.2113 |
| 4 | 0.5511 | 0.6229 | 1.682 | 0.0979 |
| 5 | 0.6275 | 0.5953 | 1.174 | 0.1062 |
| 6 | 0.4143 | 0.6178 | 0.982 | 0.1385 |

FIGURE CAPTIONS

Fig. 1   Schematic side view of the duct test section with the disturbance
elements in place

Fig. 2   Response of the local Sherwood number distribution to changes in
Reynolds number (e/H = 0.164, p/e = 18.3)

Fig. 3   Response of the local Sherwood number distribution to changes in
pitch (Re = 12,700, e/H = 0.082)

Fig. 4   Response of the local Sherwood number distribution to changes in
the relative heights of the disturbance rods and the duct
(Re ≃ 20,000, p/e = 18.3)

Fig. 5   Per-cycle fully developed Sherwood numbers

Fig. 6   Comparison of per-cycle fully developed Sherwood numbers for one-sided
and two-sided disturbed ducts, e/H = 0.082

Fig. 7   Comparison of per-cycle fully developed Sherwood numbers for one-sided
and two-sided disturbed ducts, e/H = 0.164

Fig. 8   Fully developed friction factors

Fig. 9   Friction factor correlation in terms of roughness parameters

Fig. 10  Sherwood number correlation in terms of roughness parameters

Fig. 11  Relationship between Re for periodically disturbed ducts and Re* for
a disturbance-free duct (equal pumping power constraint). The A
curves are for two-sided disturbed ducts and the B curves are for
one-sided disturbed ducts.

Fig. 12  Comparison of fully developed transfer coefficients for periodically
disturbed ducts and a disturbance-free duct (equal pumping power
constraint). The A curves are for two-sided disturbed ducts and the
B curves are for one-sided disturbed ducts.
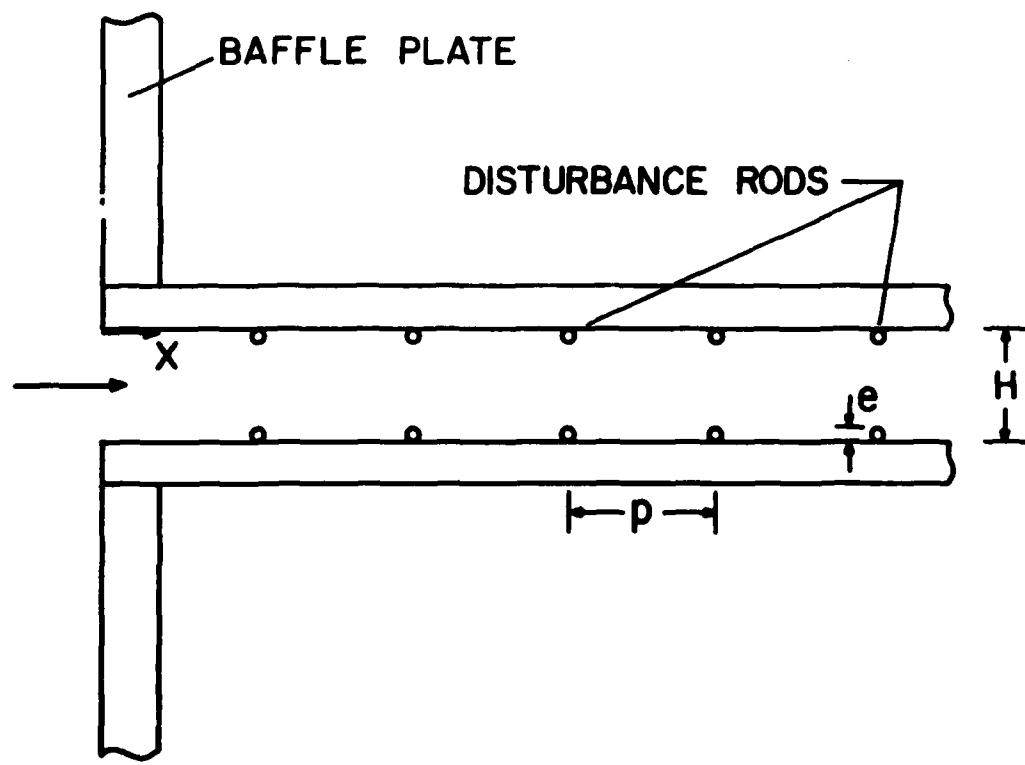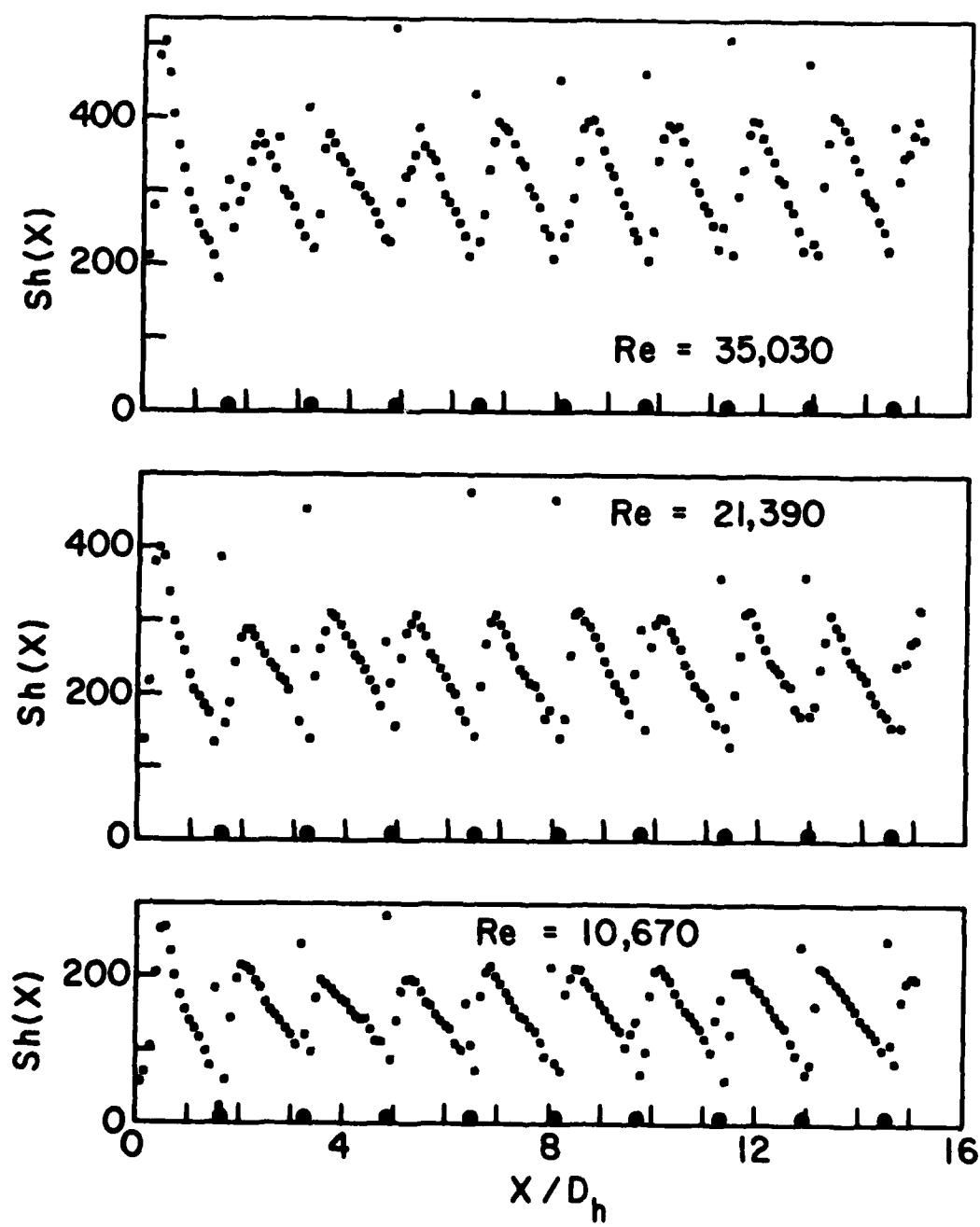
Fig. 1

Fig. 2
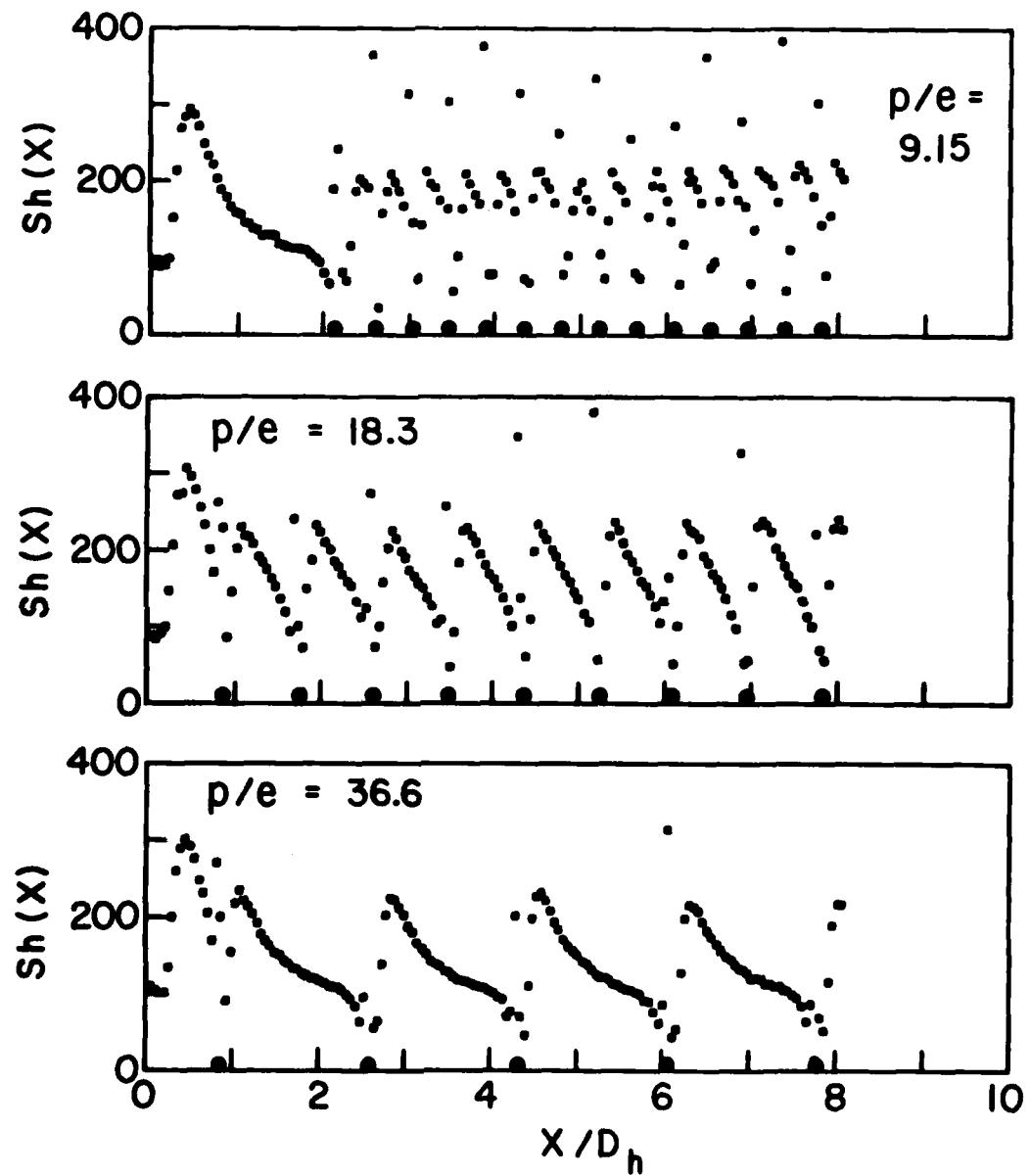
Fig. 3
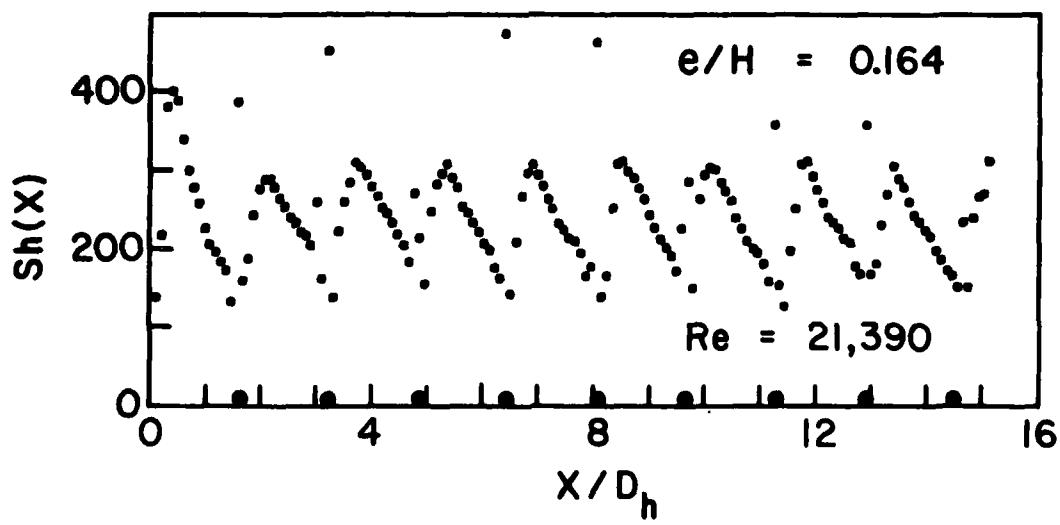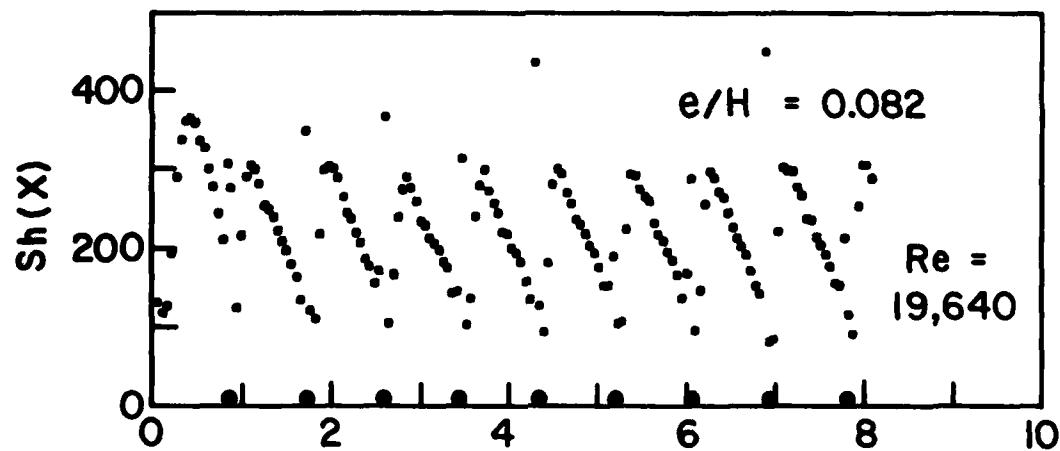
Fig. 4
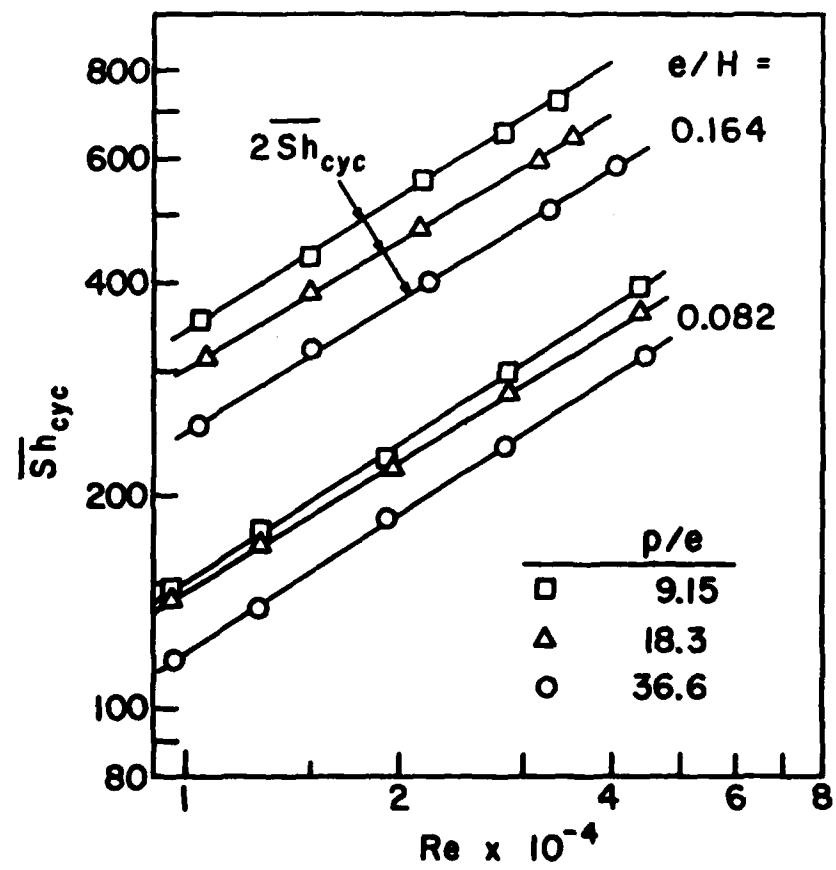
Fig. 5
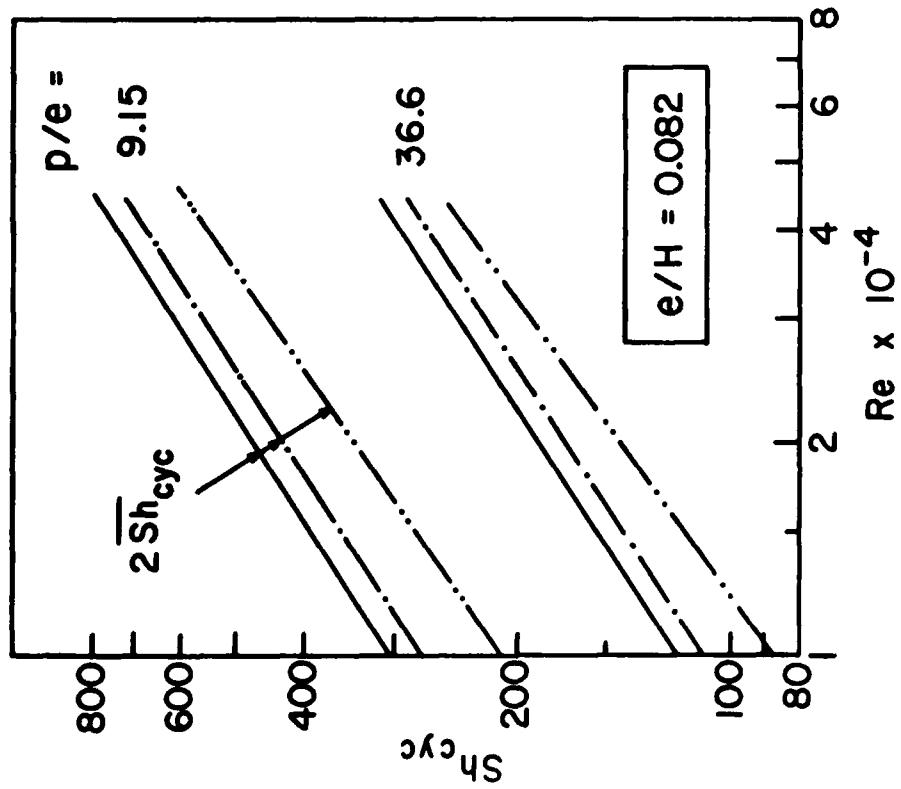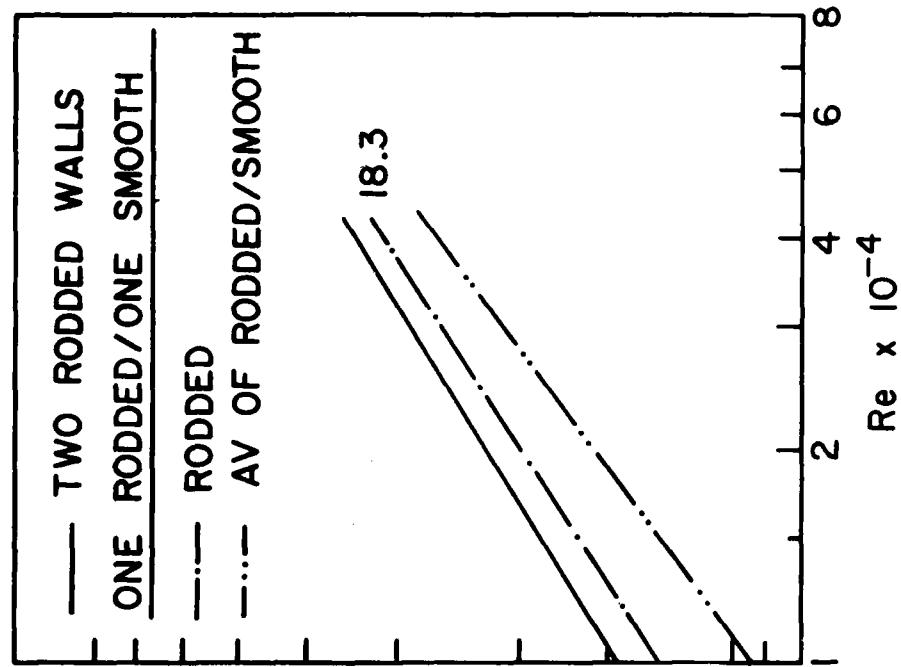
Fig.6
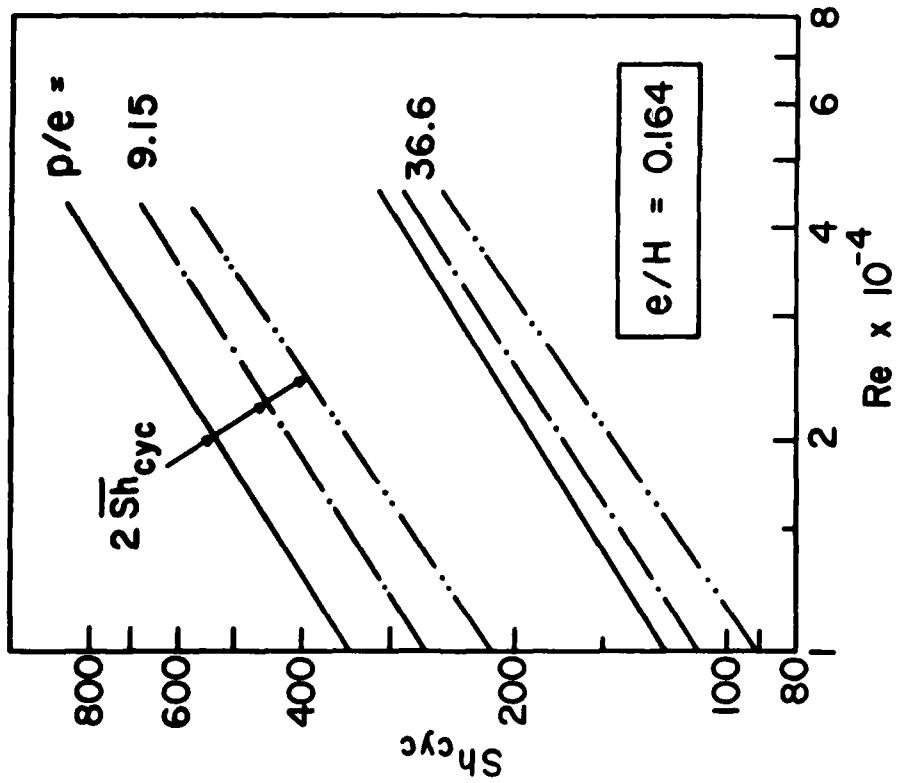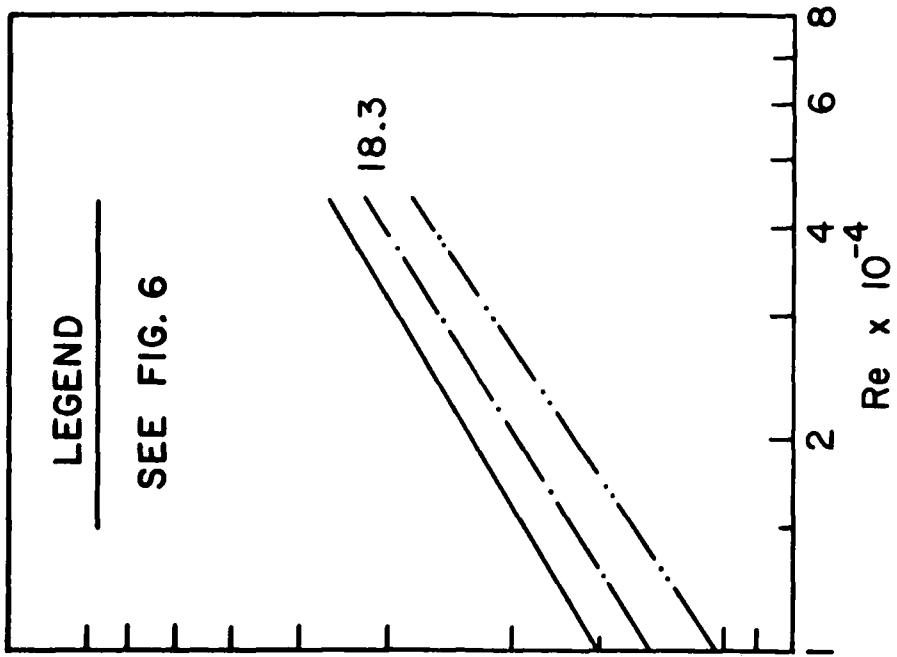
Fig. 7
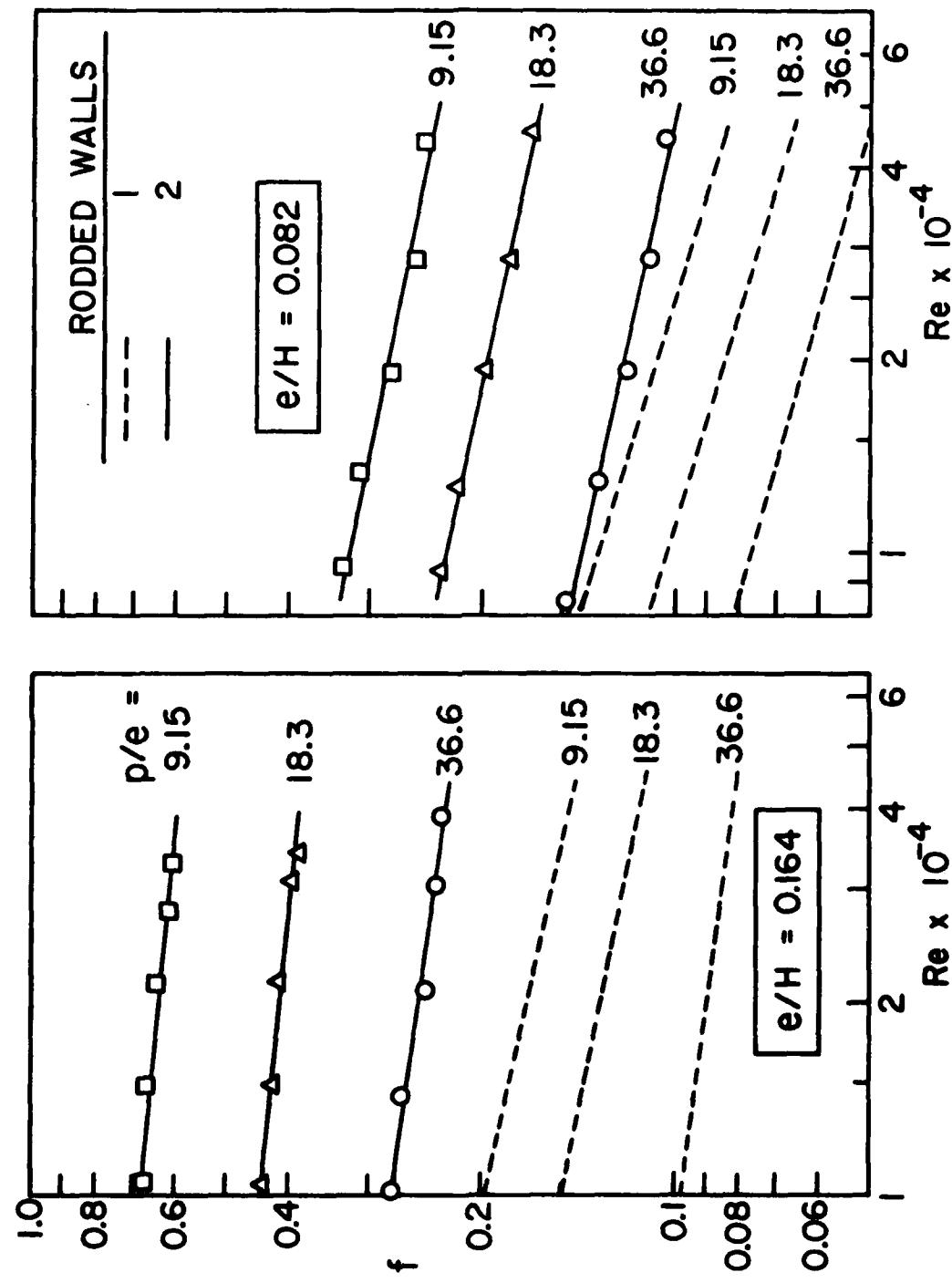
Fig. 8
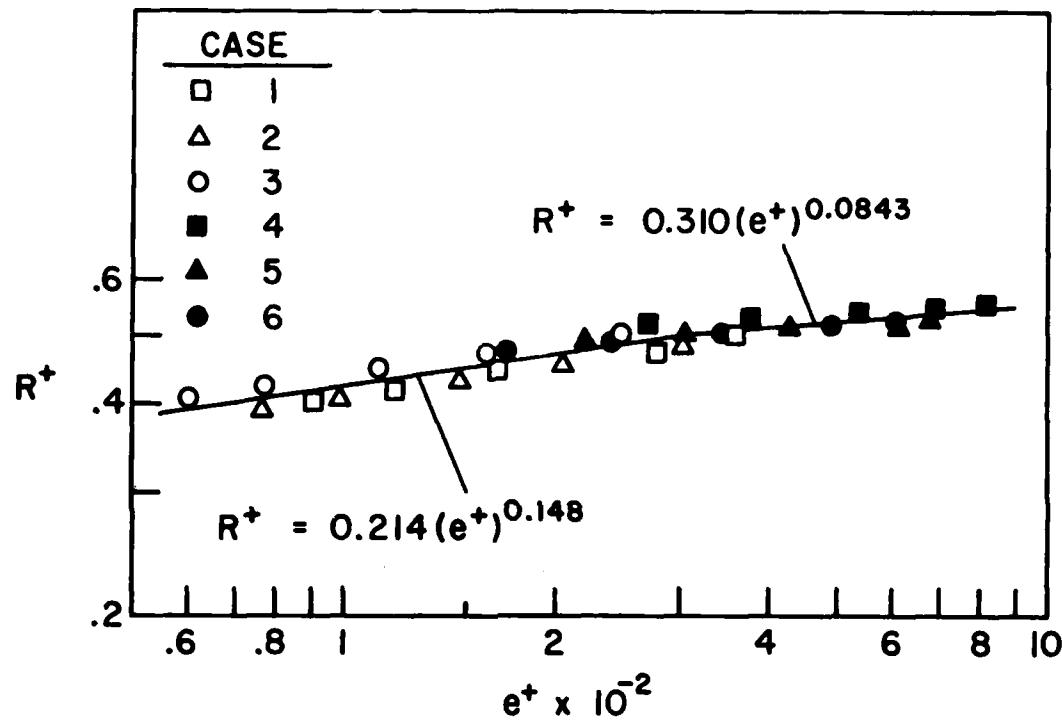
Fig. 9
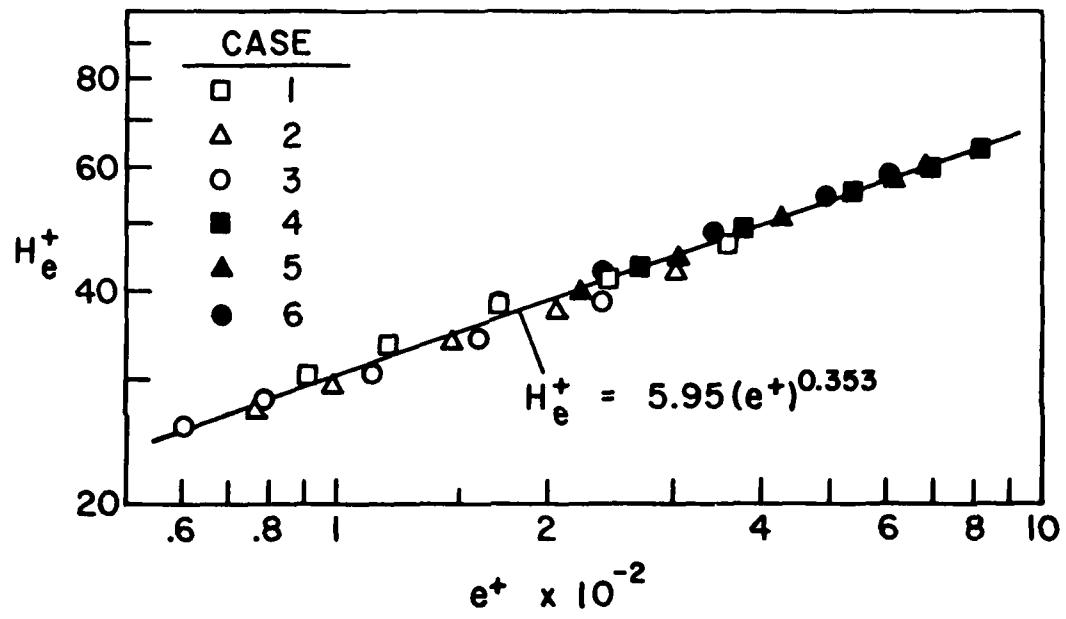
Fig. 10
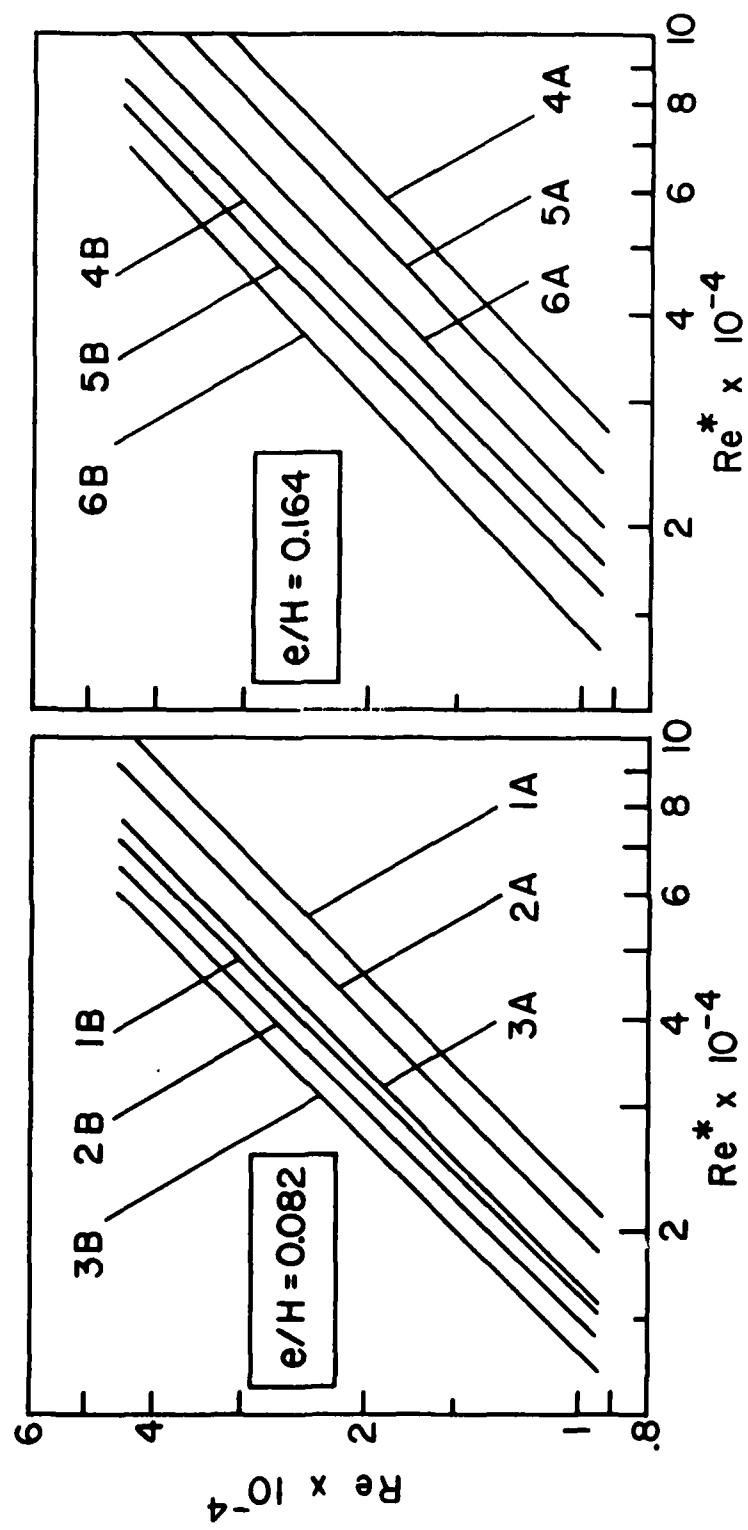
Fig. II
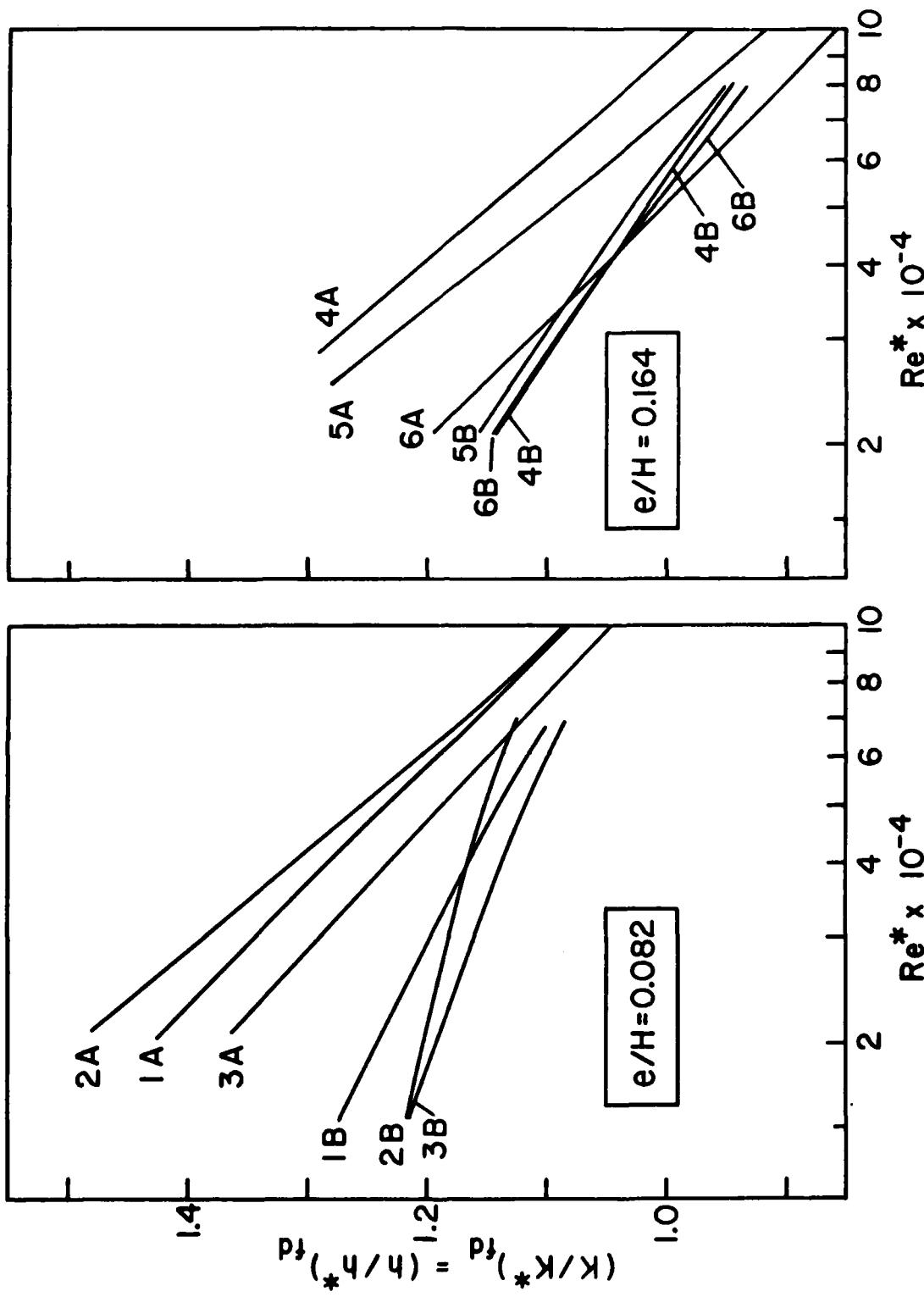
Fig. 12

# DISTRIBUTION LIST

## HEAT TRANSFER

One copy except
as noted

Mr. M. Keith Ellingsworth                              5
Power Program
Office of Naval Research
800 N. Quincy Street
Arlington, VA 22203

Defense Documentation Center                          12
Building 5, Cameron Station
Alexandria, VA 22314

Technical Information Division                          6
Naval Research Laboratory
4555 Overlook Avenue SW
Washington, DC 20375

Professor Paul Marto
Department of Mechanical Engineering
US Naval Post Graduate School
Monterey, CA 93940

Professor Bruce Rankin
Naval Systems Engineering
US Naval Academy
Annapolis, MD 21402

Office of Naval Research Eastern/
    Central Regional Office
Bldg 114, Section D
666 Summer Street
Boston, Massachusetts 02210

Office of Naval Research Branch Office
536 South Clark Street
Chicago, Ill. 60605

Office of Naval Research
Western Regional Office
1030 East Green Street
Pasadena, CA 91106

Mr. Charles Miller, Code 05R13
Crystal Plaza #6
Naval Sea Systems Command
Washinton, DC 20362

Professor Charles B. Watkins
Chairman, Mechanical Engineering Department
Howard University
Washington, DC 20059

Professor Adrian Bejan
Department of Mechanical Engineering
University of Colorado
Boulder, Colorado 80309

Professor Donald M. McEligot
Department of Aerospace and Mechanical Engineering
Engineering Experiment Station
University of Arizona 85721

Professor Paul A. Libby
Department of Applied Mechanics and Engineering Sciences
University of California San Diego
Post Office Box 109
La Jolla, CA 92037

Professor C. Forbes Dewey Jr.
Fluid Mechanics Laboratory
Massachusetts Institute of Technology
Cambridge, Massachusetts 02139

Professor William G. Characklis
Dept. of Civil Engineering and Engineering Mechanics
Montana State University
Bozeman, Montana 59717

Professor Ralph Webb
Department of Mechanical Engineering
Pennsylvania State University
208 Mechanical Engineering Bldg.
University Park, PA 16802

Professor Warren Rohsenow
Mechanical Engineering Department
Massachusetts Institute of Technology
77 Massachusetts Avenue
Cambridge, Massachusetts 02139

Professor A. Louis London
Mechanical Engineering Department
Bldg. 500, Room 501B
Stanford University
Stanford, CA 94305

Professor James G. Knudsen
Associate Dean, School of Engineering
Oregon State University
219 Covell Hall
Corvallis, Oregon 97331

Professor Arthur E. Bergles
Mechanical Engineering Department
Iowa State University
Ames, Iowa 50011

Professor Kenneth J. Bell
School of Chemical Engineering
Oklahoma State University
Stillwater, Oklahoma 74074

Dr. James Lorenz
Component Technology Division
Argonne National Laboratory
9700 South Cass Avenue
Argonne, Illinois 60439

Dr. David M. Eissenberg
Oak Ridge National Laboratory
P.O. Box Y, Bldg. 9204-1, MS-0
Oak Ridge, Tennessee 37830

Dr. Jerry Taborak
Technical Director
Heat Transfer Research Institute
1000 South Fremont Avenue
Alhambra, CA 91802

Dr. Simion Kuo
Chief, Energy Systems
Energy Research Laboratory
United Technology Research Center
East Hartford, Connecticut 06108

Mr. Jack Yampolsky
General Atomic Company
P.O. Box 81608
San Diego, CA 92138

Mr. Ted Carnavos
Noranda Metal Industries, Inc.
Prospect Drive
Newtown, Connecticut 06470

Dr. Ramesh K. Shah
Harrison Radiator Division
General Motors Corporation
Lockport, New York 14094

Dr. Ravi K. Sakhuja
Manager, Advanced Programs
Thermo Electron Corporation
101 First Avenue
Waltham, Massachusetts 02154

Mr. Doug Marron
Engine R&D Branch, Code 5231
NC #4
Naval Sea Systems Command
Washington, D.C.   20362
(Tel 202-692-6874)

Mr. Richard S. Carlton
Director, Engines Division, Code 523
NC #4
Naval Sea Systems Command
Washington, D.C.   20362
(Tel. 202-692-6868)

Mr. Richard F. Wyvill
Engine Design Branch, Code 5232
NC #4
Naval Sea Systems Command
Washington, D.C.   20362
(Tel 202-692-6931)

Mr. Walter Ritz
Code 033C
Naval Ships Systems Engineering Station
Philadelphia, Pennsylvania   19112
(Tel. 215-755-3841)

Dr. Simion Kuo
United Tech. Res. Center
Silver Lane
East Hartford, Conn.   06108
(Tel. 203-727-7258)

Mr. T.M. Herder
Bldg. 464-G2
General Electric Co.
1100 Western Ave.
Lynn, Massachusettes   01910
(Tel. 617-594-3360)

Mr. Ed Strain
AiResearch of Arizona
Dept. 76, Mail Stop 301-2
P.O. Box 5217
Phoenix, Arizona   85010
(Tel 602-267-2797)

Mr. Norm McIntire
Solar Turbines International
2200 Pacific Hwy.
San Diego, CA   92101
(Tel. 714-238-6527)

Mr. Robert W. Perkins
Turbotec Products, Inc.
533 Downey Drive
New Britain, Connecticut 06051

Dr. Keith E. Starner
York Division, Borg-Warner Corp.
P.O. Box 1592
York, PA 17405

Mr. Peter Wishart
C-E Power Systems
Combustion Engineering, Inc.
Windsor, Connecticut 06095

Mr. Henry W. Braum
Manager, Condenser Engineering Department
Delaval
Front Street
Florence, New Jersey 08518

Dr. Thomas Rabas
Steam Turbine-Generator Technical Operations Division
Westinghouse Electric Corporation
Lester Branch
P.O. Box 9175 N2
Philadelphia, PA 19113

END

FILMED

6-84

DTIC